



PASSIVE MIMO RADAR DETECTION

DISSERTATION

Daniel E. Hack, Civilian
AFIT-ENG-DS-13-S-07

DEPARTMENT OF THE AIR FORCE
AIR UNIVERSITY

AIR FORCE INSTITUTE OF TECHNOLOGY

Wright-Patterson Air Force Base, Ohio

APPROVED FOR PUBLIC RELEASE; DISTRIBUTION UNLIMITED

The views expressed in this document are those of the author and do not reflect the official policy or position of the United States Air Force, the United States Department of Defense or the United States Government.

AFIT-ENG-DS-13-S-07

PASSIVE MIMO RADAR DETECTION

DISSERTATION

Presented to the Faculty

Graduate School of Engineering and Management

Air Force Institute of Technology

Air University

Air Education and Training Command

in Partial Fulfillment of the Requirements for the

Degree of Doctor of Philosophy

Daniel E. Hack, B.S.E.E., M.S.

Civilian

September 2013

APPROVED FOR PUBLIC RELEASE; DISTRIBUTION UNLIMITED

PASSIVE MIMO RADAR DETECTION

Daniel E. Hack, B.S.E.E., M.S.
Civilian

Approved:

//signed//

September 2013

Dr. Michael A. Saville
Dissertation Advisor

Date

//signed//

September 2013

Dr. Richard K. Martin
Committee Member

Date

//signed//

September 2013

Dr. Matthew C. Fickus
Committee Member

Date

Accepted:

//signed//

September 2013

Dr. Heidi R. Ries
Interim Dean, Graduate School of Engineering
and Management

Date

Abstract

Passive multiple-input multiple-output (MIMO) radar is a sensor network comprised of multiple distributed receivers that detects and localizes targets using the emissions from multiple non-cooperative radio frequency transmitters. This dissertation advances the theory of centralized passive MIMO radar (PMR) detection by proposing two novel generalized likelihood ratio test (GLRT) detectors. The first addresses detection in PMR networks without direct-path signals. The second addresses detection in PMR networks with direct-path signals. The probability distributions of both test statistics are investigated using recent results from random matrix theory. Equivalence is established between PMR networks without direct-path signals and passive source localization (PSL) networks. Comparison of both detectors with a centralized GLRT for active MIMO radar (AMR) detection reveals that PMR may be interpreted as the link between AMR and PSL sensor networks. In particular, under high direct-path-to-noise ratio (DNR) conditions, PMR sensitivity and ambiguity approaches that of AMR. Under low-DNR conditions, PMR sensitivity and ambiguity approaches that of PSL. At intermediate DNRs, PMR sensitivity and ambiguity smoothly varies between that of AMR and PSL. In this way, PMR unifies PSL and AMR within a common theoretical framework. This result provides insight into the fundamental natures of active and passive distributed sensing.

AFIT-ENG-DS-13-S-07

To my wife.

Acknowledgements

First, I thank my advisor, Dr. Michael Saville, for guiding me through the research process and seeing my degree program through to completion. I also thank the members of my dissertation committee, Dr. Richard Martin and Dr. Matthew Fickus, and the Dean's representative, Dr. Alfred Thal, for critically evaluating the merit of this work. Completion of this program would not have been possible without the financial assistance provided by Dynetics, the Dayton Area Graduate Studies Institute, and Matrix Research. I also thank Dr. Braham Himed and Dr. Alan Kerrick of the Air Force Research Laboratory for sponsoring this research and providing the opportunity to present this work to the broader research community. I am grateful to my professional colleagues at Matrix Research, Dr. Carl Rossler and Mr. Richard Umbach, whose work I often interrupted to discuss my own. Finally, I am greatly indebted to Dr. Lee Patton—boss, mentor, and friend—whose keen insight and critical eye were invaluable in defining and refining this research program.

Daniel E. Hack

Table of Contents

	Page
Abstract	iv
Acknowledgements	vi
List of Figures	x
List of Abbreviations	xiii
List of Symbols	xv
 I. Introduction	 1
1.1 Passive Radar	1
1.1.1 Network Topology	4
1.1.2 Signal Environment	5
1.2 Related RF Sensor Networks	6
1.2.1 Active MIMO Radar	7
1.2.2 Passive Source Localization	8
1.3 Relevance to United States Air Force	9
1.4 Current Shortcomings	9
1.4.1 PMR Detection with References	10
1.4.2 PMR Detection without References	11
1.5 Research Hypothesis and Methodology	13
1.6 Research Contributions	14
1.6.1 PMR Detection without References	14
1.6.2 PMR Detection with References	15
1.6.3 Unified Detection Framework	16
1.7 Chapter Outline	17
 II. Signal Model	 18
2.1 Scenario	18
2.2 Signal Environment	19
2.2.1 Direct-Path Signal	22
2.2.2 Target-Path Signal	25
2.3 Discretization	26
2.4 Summary	29
 III. Passive MIMO Radar Detection without References	 30
3.1 Signal Model	32
3.2 Surveillance-Surveillance GLRT	34
3.3 Distribution	39

	Page
3.3.1 Alternative Hypothesis	40
3.3.2 Null Hypothesis	41
3.3.3 Dependence on SNR	42
3.4 Interpretation	43
3.5 Simulations	47
3.5.1 Detection Performance	48
3.5.2 Ambiguity Performance	51
3.5.3 Numerical Challenges	58
3.6 Conclusion	59
IV. Passive MIMO Radar Detection with References	60
4.1 Signal Model	61
4.2 Detectors	64
4.2.1 Reference-Surveillance GLRT	65
4.2.2 Surveillance-Surveillance GLRT	69
4.2.3 Matched Filter GLRT	69
4.3 Distributions	70
4.3.1 Matched Filter GLRT Distributions	70
4.3.2 Reference-Surveillance GLRT Distributions	71
4.3.3 Dependence on SNR and DNR	74
4.4 Interpretations	76
4.4.1 Surveillance-Surveillance Processing	76
4.4.2 Reference-Surveillance Processing	78
4.5 Simulations	80
4.5.1 Detection Performance	80
4.5.2 Ambiguity Performance	84
4.6 Discussion	93
4.7 Conclusion	95
V. Unified Detection Framework	96
5.1 Transformations	96
5.2 Signal Models	99
5.2.1 Active MIMO Radar	99
5.2.2 Passive MIMO Radar	100
5.2.3 Passive Source Localization	101
5.3 Detectors	101
5.3.1 Matched Filter GLRT	102
5.3.2 Surveillance-Surveillance GLRT	103
5.3.3 Reference-Surveillance GLRT	104
5.4 Conclusion	106

	Page
VI. Conclusion	107
6.1 Summary of Contributions	107
6.1.1 PMR Detection without References	107
6.1.2 PMR Detection with References	108
6.1.3 Unified Detection Framework	109
6.2 Future Research	110
A. Far-Field Differential Range Approximation	112
B. Reference and Surveillance Channel Formation	113
Bibliography	118

List of Figures

Figure		Page
1	Passive Radar Publications by Year and Type	3
2	Passive Radar Network Topologies	5
3	An Active MIMO Radar Sensor Network.....	7
4	A Passive Source Localization Sensor Network	8
5	Reference and Surveillance Channel Formation	11
6	Passive MIMO Radar without Direct-Path References	12
7	A Unified Framework for Active and Passive Distributed RF Sensing.....	16
8	Geometry for the ij th Transmitter-Receiver Pair	18
9	Passive MIMO Radar without Direct-Path Signals	30
10	The ij th Bistatic Pair in a PMR Network without Direct-Path Signals	33
11	A PSL Sensor Network with Three Receivers	44
12	Interpretation of PMR without References as a PSL Scenario	45
13	Predicted (Pred) and Simulated (Sim) P_d Curves for a PMR Network with a Varying Number of Transmitters and Receivers	49
14	Additional P_d Curves for PMR Networks with a Varying Number of Transmitters and Receivers	50
15	P_d Curves for a PMR Scenario with 2 Transmitters, 3 Receivers, and $L = [1, 3, 10, 30, 100, 300, 1000]$ Samples per Signal	52
16	Integration Gain G_{int} as a Function of L for a PMR Scenario with 2 Transmitters and 3 Receivers	52

Figure		Page
17	Example Transmit Signal Ambiguity Function $\chi^i(\Delta\tau, \Delta f_d)$ (dB)	54
18	$\xi_{ss}(\mathbf{p}, \dot{\mathbf{p}}) _{\dot{\mathbf{p}}=\mathbf{0}}$ (dB) for $\dot{\mathbf{t}} = \mathbf{0}$ and Single-Element Receivers	55
19	TDOA $\Delta\tau_p^{jk} = \Delta\ell_p^{jk}/f_s$ (μs) for $j = 2$ and $k = 3$	55
20	$\xi_{ss}(\mathbf{p}, \dot{\mathbf{p}}) _{\dot{\mathbf{p}}=\mathbf{0}}$ (dB) for $\dot{\mathbf{t}} = \mathbf{0}$ and Six-Element ULA Receivers	56
21	$\xi_{ss}(\mathbf{p}, \dot{\mathbf{p}}) _{\dot{\mathbf{p}}=\mathbf{0}}$ (dB) for $\dot{\mathbf{t}} = \mathbf{0}$ and Single-Element Receivers	57
22	FDOA $(\frac{f_s}{2\pi})\Delta\nu_p^{i,jk}(\mathbf{p}, \dot{\mathbf{p}}) _{\dot{\mathbf{p}}=\dot{\mathbf{t}}}$ (kHz) for $i = 1, j = 2$, and $k = 3$	57
23	$\xi_{ss}(\mathbf{p}, \dot{\mathbf{p}}) _{\dot{\mathbf{p}}=\mathbf{0}}$ (dB) for $\dot{\mathbf{t}} = \mathbf{0}$ and Six-Element ULA Receivers	58
24	A Passive MIMO Radar Sensor Network	60
25	The ij th Bistatic (Transmitter-Receiver) Pair in a PMR Network	62
26	Empirical and Predicted PDFs for ξ_{rs} Under (a) \mathcal{H}_0 and (b) \mathcal{H}_1	75
27	Probability of Detection Curves for $N_t = 2, N_r = 3$, and $L = 1000$	81
28	2D View of RS-GLRT P_d for $N_t = 2, N_r = 3$, and $L = 1000$	82
29	Depiction of RS-GLRT $P_d = 0.9$ iso-contours for $N_t = 2$, $N_r = 3$, and $L = [1, 3, 10, 30, 100, 300, 1000, 3000, 10000]$. The SNR_{avg} values at which the SS-GLRT and MF-GLRT achieve $P_d = 0.9$ are depicted by dash-dotted red lines and dashed blue lines, respectively, for each L	83
30	G_{int} as a Function of L for a PMR Scenario with $N_t = 2$ and $N_r = 3$	84

Figure		Page
31	Low- $\bar{\rho}$ Ambiguity of the (a) RS-GLRT and (b) SS-GLRT for a Stationary Target	86
32	Example TDOA and FDOA Plots for $i = 1$, $j = 2$, and $k = 3$	87
33	Low- $\bar{\rho}$ Ambiguity of the (a) RS-GLRT and (b) SS-GLRT for a Moving Target	88
34	High-DNR Ambiguity of the (a) RS-GLRT and (b) MF-GLRT for a Stationary Target	89
35	Bistatic Range and Bistatic Doppler for $i = 1$ and $j = 2$	89
36	High-DNR Ambiguity of the (a,c) RS-GLRT and (b,d) MF-GLRT for a Moving Target	90
37	Transition Region Ambiguity of the RS-GLRT for a Stationary Target	92
38	Transition Region Ambiguity of the RS-GLRT for a Moving Target	92
39	A Unified Theoretical Framework for Detection in Active and Passive Distributed RF Sensor Networks	97
40	Transformations between AMR, PMR, and PSL Signal Environments	98
41	Decomposition of \mathbb{C}^{N_e} into Subspaces Spanned by the Columns of \mathbf{B}^{ij} ; the Rank-2 Subspace $\langle [\mathbf{a}_d^{ij} \ \mathbf{a}_p^{ij}] \rangle$ is Depicted by the Gray Plane	114

List of Abbreviations

Abbreviation	Page
A2/AD	anti-access/area denial 9
AF	ambiguity function 47
AMR	active MIMO radar 1
AOA	angle-of-arrival 8
CAF	cross-ambiguity function 10
CDF	cumulative distribution function 58
CORA	COvert RAdar 2
CPI	coherent processing interval 19
CRLB	Cramer-Rao Lower Bound 110
CW	continuous wave 6
DAB	digital audio broadcast 2
DFT	discrete Fourier transform 27
DNR	direct-path-to-noise ratio 11
DVB-T	terrestrial digital video broadcast 2
FDOA	frequency difference of arrival 8
FM	frequency modulated 2
GAMMA	Gruppenantenne für militärische Mobilfunk Aufklärung 2
GLRT	generalized likelihood ratio test 13
MF-GLRT	matched filter GLRT 15
MIMO	multiple-input multiple-output 1
MLE	maximum likelihood estimate 36

Abbreviation		Page
PaRaDe	Passive Radar Demonstrator	2
PBR	passive bistatic radar	4
PDF	probability density function	35
PMR	passive MIMO radar	1
PSD	power spectral density	20
PSL	passive source localization	1
RF	radio frequency	1
RS-GLRT	reference-surveillance GLRT	15
SNR	signal-to-noise ratio	14
SS-GLRT	surveillance-surveillance GLRT	14
STAP	space-time adaptive processing	110
TDOA	time difference of arrival	8
UHF	ultra high frequency	2
VHF	very high frequency	2
WSS	wide-sense stationary	20

List of Symbols

Symbol	Page
$ \cdot $	matrix determinant 41
$\ \cdot\ _F$	matrix Frobenius norm 72
$\mathbf{0}_{L^i}$	zero vector of length L^i 29
$\mathbf{a}^{ij}(\mathbf{x})$	spatial steering vector in the direction of \mathbf{x} at the j th receiver with respect to the i th transmit channel 34
\mathbf{a}_d^{ij}	abbreviated spatial steering vector in the direction of \mathbf{d}^i , i.e., $\mathbf{a}_d^{ij} = \mathbf{a}^{ij}(\mathbf{d}^i)$ 64
\mathbf{a}_p^{ij}	abbreviated spatial steering vector in the direction of \mathbf{p} , i.e., $\mathbf{a}_p^{ij} = \mathbf{a}^{ij}(\mathbf{p})$ 65
\mathbf{a}_t^{ij}	abbreviated spatial steering vector in direction of \mathbf{t} , i.e., $\mathbf{a}_t^{ij} = \mathbf{a}^{ij}(\mathbf{t})$ 34
b_1	$b_1 = 1$ under \mathcal{H}_1 and $b_1 = 0$ under \mathcal{H}_0 39
β_{pt}^{ij}	scalar that quantifies loss due to mismatch between actual (\mathbf{t}) and hypothesized (\mathbf{p}) target positions 45
\mathbf{b}_r^{ij}	length- N_e reference channel steering vector (beamformer) with respect to ij th Tx-Rx pair 113
\mathbf{b}_s^{ij}	length- N_e surveillance channel steering vector (beamformer) with respect to ij th Tx-Rx pair 113
B^i	bandwidth of $u^i(t)$ in Hertz 19
B^j	bandwidth of j th receiver in Hertz 20
\mathbf{B}^{ij}	unitary matrix comprised of N_e orthonormal vectors including \mathbf{b}_s^{ij} and \mathbf{b}_r^{ij} 113
c	speed of light 21
δ_n^j	vector from reference element \mathbf{r}_1^j to the n th element of the j th receiver array 19

Symbol	Page
$\Delta\ell_p^{jk}$	TDOA of the hypothesized target position \mathbf{p} between the j th and k th receivers 46
$\Delta\ell_t^{jk}$	TDOA of the actual target position \mathbf{t} between the j th and k th receivers 46
$\Delta\nu_p^{i,jk}$	FDOA of the hypothesized target state $(\mathbf{p}, \dot{\mathbf{p}})$ between the j th and k th receivers with respect to the i th transmit channel 46
$\Delta\nu_t^{i,jk}$	FDOA of the actual target state $(\mathbf{t}, \dot{\mathbf{t}})$ between the j th and k th receivers with respect to the i th transmit channel 46
$\Delta R_n^{ij}(\mathbf{d}^i)$	differential range of the n th element of the j th receiver with respect to the i th transmitter 22
\mathbf{d}^i	position of i th transmitter 18
$\dot{\mathbf{d}}^i$	velocity of i th transmitter 18
$\mathcal{D}(\ell, \nu)$	delay-Doppler operator matrix 28
\mathcal{D}_d^{ij}	abbreviation for direct-path delay-Doppler operator $\mathcal{D}(\ell_d^{ij}, \nu_d^{ij})$ 63
\mathcal{D}_p^{ij}	abbreviation for delay-Doppler operator $\mathcal{D}(\ell_p^{ij}, \nu_p^{ij})$ 35
$\mathcal{D}_{p,1}^i$	delay-Doppler operator associated with the first leg of the ij th hypothesized target-path channel 44
$\mathcal{D}_{p,2}^{ij}$	delay-Doppler operator associated with the second leg of the ij th hypothesized target-path channel 44
\mathcal{D}_t^{ij}	abbreviation for delay-Doppler operator $\mathcal{D}(\ell_t^{ij}, \nu_t^{ij})$ 33
$\mathcal{D}_{t,1}^i$	delay-Doppler operator associated with the first leg of the ij th target-path channel 34
$\mathcal{D}_{t,2}^{ij}$	delay-Doppler operator associated with the second leg of the ij th target-path channel 34

Symbol		Page
$\text{DNR}_{\text{avg}}^i$	average input direct-path-to-noise ratio associated with the i th transmitter after reference channel formation	71
E^i	the cumulative energy of \mathbf{s}^i	68
$E_{(rs)^\perp}^{ij}$	the energy of \mathbf{s}^{ij} that projects into the orthogonal complement of the subspace spanned by \mathbf{a}_d^{ij} and \mathbf{a}_p^{ij}	67
$f_{\chi^2}(x; k, \zeta)$	probability density function of $\chi_{(k),\zeta}^2$	71
f_s^i	ADC sampling rate of i th channel in Hertz	26
F_{rr}^i	abbreviation for Frobenius norm $\ \mathbf{G}_{rr}^i\ _F$	73
F_{rs}^i	abbreviation for Frobenius norm $\ \mathbf{G}_{rs}^i\ _F$	73
F_{ss}^i	abbreviation for Frobenius norm $\ \mathbf{G}_{ss}^i\ _F$	73
Φ_1^i	matrix of delay-Doppler compensated surveillance and reference channels associated with the i th transmit channel	68
Φ_r^i	matrix of delay-Doppler compensated reference channels associated with the i th transmit channel	68
Φ_s^i	matrix of delay-Doppler compensated surveillance channels associated with the i th transmit channel	38
$\gamma(\cdot, \cdot)$	incomplete gamma function	41
γ_d	vector of direct-path channel coefficients with respect to all transmitters and all receivers	65
γ_d^i	vector of direct-path channel coefficients with respect to the i th transmitter and all receivers	65
γ_d^{ij}	direct-path channel coefficient associated with the i th transmitter and j th receiver	24
γ_p	vector of all hypothesized target-path channel coefficients	35

Symbol		Page
γ_p^i	vector of hypothesized target-path channel coefficients associated with the i th transmitter	35
γ_p^{ij}	hypothesized target-path channel coefficient associated with the i th transmitter and j th receiver	35
$\hat{\gamma}_p^{ij}$	MLE of γ_p^{ij}	37
γ_t^{ij}	target-path channel coefficient associated with the i th transmitter and j th receiver	26
$\gamma_{t,1}^i$	channel coefficient associated with the propagation path from the i th transmitter to the target, i.e., the first leg of the ij th target-path channel	33
$\gamma_{t,2}^{ij}$	channel coefficient associated with the second leg of the ij th target-path	33
$\Gamma(\cdot)$	gamma function	40
G_{dp}	direct-path gain, i.e., the sensitivity improvement due to exploitation of direct-path signals	95
$G_{e,n}^j(\mathbf{x})$	element pattern value of n th element of j th receiver array in direction of \mathbf{x}	19
$G_{int}(L)$	integration gain as a function of signal length L	51
\mathbf{G}_1^i	Gram matrix formed from delay-Doppler compensated surveillance and reference signals associated with the i th transmitter	68
\mathbf{G}_{rr}^i	Gram matrix formed from delay-Doppler compensated reference signals associated with the i th transmitter	69
\mathbf{G}_{ss}^i	Gram matrix formed from delay-Doppler compensated surveillance signals associated with i th transmitter	38
\mathcal{H}_0	target-absent (null) hypothesis	35
\mathcal{H}_1	target-present (alternative) hypothesis	35
\mathbf{I}_L	identity matrix of size $L \times L$	28
$I_\nu(z)$	modified Bessel function of the first kind of order ν	71

Symbol	Page
j	the imaginary unit, i.e., $j = \sqrt{-1}$ 19
$\chi^i(\Delta\ell, \Delta\nu)$	ambiguity function of \mathbf{u}^i 47
$\chi_{sr}^{i,jk}$	cross ambiguity function between the i th surveillance channel of the j th receiver and the i th reference channel of the k th receiver 79
$\chi_{ss}^{i,jk}$	cross ambiguity function between the i th surveillance channels of the j th and k th receivers 77
$\chi_{(k),\zeta}^2$	non-central chi-squared random variable with k degrees of freedom and non-centrality ζ 70
$\hat{\mathbf{k}}_n^j(\mathbf{x})$	unit vector from n th element of j th receiver array in direction of \mathbf{x} 19
ℓ_d^{ij}	normalized delay of ij th direct-path channel in samples 27
ℓ_p^{ij}	normalized delay of ij th hypothesized target-path channel in samples 35
ℓ_t^{ij}	normalized delay of ij th target-path channel in samples 27
λ^i	wavelength of i th transmitter 21
$\lambda_1(\cdot)$	the largest eigenvalue of its matrix argument 38
$\lambda_n(\cdot)$	the n th largest eigenvalue of its matrix argument 72
L^i	number of ADC samples of i th channel of j th receiver over the CPI 27
μ_r^{ij}	reference channel coefficient associated with the ij th direct-path channel 67
$\boldsymbol{\mu}_s^i$	vector of surveillance channel coefficients associated with the i th transit channel 40
μ_s^{ij}	surveillance channel coefficient associated with ij th hypothesized target-path channel 39

Symbol		Page
$\tilde{\mu}_s^{ij}$	surveillance channel coefficient associated with the ij th Tx-Rx pair that includes the effect of angular mismatch between hypothesized and actual target positions, i.e., $\tilde{\mu}_s^{ij} = \beta_{pt}^{ij} \mu_s^{ij}$	45
ν_d^{ij}	normalized direct-path Doppler frequency of ij th channel in radians per sample	27
ν_p^{ij}	normalized Doppler shift of ij th hypothesized target-path channel in radians per sample	35
ν_t^{ij}	normalized target-path Doppler frequency of ij th channel in radians per sample	27
\mathbf{n}_n^{ij}	sample vector of the ij th channel complex baseband noise signal associated with the n th array element	29
$n_n^{ij}(t)$	WSS complex baseband Gaussian receiver noise at n th element of j th receiver array in the i th transmit channel	21
$\tilde{n}_n^j(t)$	analytic WSS bandpass Gaussian white receiver noise at n th element of j th receiver array	20
$\tilde{\mathbf{n}}_s^{ij}$	delay-Doppler compensated version of \mathbf{n}_s^{ij}	39
N_0	noise power spectral density amplitude	20
N_e^j	number of elements in j th receiver array	18
N_r	number of receivers	18
N_t	number of transmitters	18
$\tilde{\mathbf{N}}_s^i$	matrix of delay-Doppler compensated surveillance channel noise vectors associated with the i th transmit channel	40
ω_c^i	i th transmitter carrier frequency	19
ω_c^j	center radian frequency of j th receiver	20
ω_d^{ij}	radian Doppler frequency with respect to the i th transmitter and j th receiver	23

Symbol		Page
ω_t^{ij}	bistatic radian Doppler frequency with respect to i th transmitter, target, and j th receiver	25
Ω^i	non-centrality matrix of complex Wishart matrix \mathbf{G}_{ss}^i	40
Ω_1^i	rank-1 non-centrality matrix of complex Wishart matrix \mathbf{G}_1^i	72
Ω_{rr}^i	rank-1 non-centrality matrix of complex Wishart matrix \mathbf{G}_{rr}^i	71
\mathbf{p}	hypothesized target position	34
$\dot{\mathbf{p}}$	hypothesized target velocity	34
$p_{\xi_{ss}}(\xi)$	probability density function of ξ_{ss}	39
$p_{\xi_{ss}}^i(\xi)$	probability density function of ξ_{ss}^i	39
P_{erp}^i	effective radiated power by i th transmitter in direction of \mathbf{x}	21
\mathbf{P}_r^{ij}	orthogonal projection into rank-1 subspace $\langle \mathbf{b}_r^{ij} \rangle$	114
$\mathbf{P}_{r^\perp}^{ij}$	orthogonal projection into orthogonal complement of rank-1 subspace $\langle \mathbf{b}_r^{ij} \rangle$	113
$\mathbf{P}_{r^\perp s}^{ij}$	orthogonal projection into rank-1 subspace $\langle \mathbf{b}_s^{ij} \rangle$	114
$\mathbf{P}_{(rs)^\perp}^{ij}$	orthogonal projection into orthogonal complement of rank-2 subspace $\langle \mathbf{a}_d^{ij}, \mathbf{a}_p^{ij} \rangle$	114
$\bar{\rho}^i$	average power ratio between direct-path and target-path signals for the i th transmitter	72
\mathbf{r}^j	position of j th receiver	18
$\dot{\mathbf{r}}^j$	velocity of j th receiver	18
\mathbf{r}_1^j	location of reference element of j th receiver array	18
\mathbf{r}_n^j	location of n th element of j th receiver array	18
$R_0^{ij}(t)$	range between the i th transmitter and j th receiver	18

Symbol	Page
$R_{0,n}^{ij}(t)$	direct-path range between the i th transmitter and n th element of j th receiver 22
$R_1^i(t)$	range between the i th transmitter and target 18
$R_2^j(t)$	range between the target and j th receiver 18
\mathbf{s}	concatenation of all receiver measurements associated with all transmitters 35
\mathbf{s}^i	concatenation of all receiver measurements associated with i th transmitter 35
$\mathbf{s}_{d,n}^{ij}$	sample vector of the ij th direct-path channel complex baseband signal associated with the n th array element 27
$s_{d,n}^{ij}(t)$	continuous complex baseband representation of the i th transmitter's direct-path signal associated with the n th element of the j th receiver array 22
\mathbf{s}_n^{ij}	sample vector of the ij th channel complex baseband signal associated with the n th array element 27
$s_n^{ij}(t)$	complex baseband signal from the n th element of the j th receiver associated with the i th transmit channel 21
\mathbf{s}_r^{ij}	reference channel formed at the j th receiver with respect to the i th transmitter 67
$\tilde{\mathbf{s}}_r^{ij}$	delay-Doppler compensated version of reference channel \mathbf{s}_r^{ij} 67
\mathbf{s}_s^{ij}	surveillance channel formed at the j th receiver for the i th transmit channel 37
$\tilde{\mathbf{s}}_s^{ij}$	delay-Doppler compensated version of \mathbf{s}_s^{ij} 37
$\mathbf{s}_{t,n}^{ij}$	sample vector of the ij th target-path channel complex baseband signal associated with the n th array element 27
$s_{t,n}^{ij}(t)$	continuous complex baseband representation of the i th transmitter's target-path signal associated with the n th element of the j th receiver array 25
Σ^i	covariance parameter of complex Wishart matrix \mathbf{G}_{ss}^i 40

Symbol		Page
Σ_1^i	covariance parameter of complex Wishart matrix \mathbf{G}_1^i	71
Σ_{rr}^i	covariance parameter of complex Wishart matrix \mathbf{G}_{rr}^i	71
$\text{SNR}_{\text{avg}}^i$	average input signal-to-noise ratio associated with i th transmitter after surveillance channel formation	42
τ_d^{ij}	direct-path delay between i th transmitter and reference element of j th receiver at $t = 0$	23
τ_t^{ij}	target-path delay between i th transmitter, target, and reference element of j th receiver at $t = 0$	25
$\boldsymbol{\theta}^i$	vector of random phases with i.i.d. elements uniformly distributed between 0 and 2π	48
$\vartheta_n^{ij}(\mathbf{d}^i)$	differential carrier phase of the i th direct-path signal received at the n th element of the j th receiver array with respect to the reference element carrier phase	23
$\vartheta_n^{ij}(\mathbf{t})$	differential carrier phase of the i th target-path signal received at the n th element of the j th receiver array with respect to the reference element carrier phase	25
\mathbf{t}	target position	18
$\dot{\mathbf{t}}$	target velocity	18
$\text{tr}(\cdot)$	the trace of its matrix argument	41
T	coherent processing interval (CPI)	19
T_s^i	ADC sampling period of i th channel in seconds	26
$u^i(t)$	i th transmitter's complex baseband signal	19
$\tilde{u}^i(t)$	analytic representation of i th transmit signal	19
\mathbf{u}	concatenation of all unknown transmit signals	35
\mathbf{u}^i	sample vector of the i th transmit complex baseband signal	27
$\hat{\mathbf{u}}^i$	MLE of \mathbf{u}^i	38

Symbol		Page
$\tilde{\mathbf{u}}^i$	the i th “effective” emitted signal when interpreting PMR without direct-path signals as a PSL problem	43
$U(\cdot)$	the unit step function	41
$U^i(\omega)$	spectrum of the i th transmitter’s complex baseband signal	19
$\mathbf{v}_1(\cdot)$	the eigenvector associated with the largest eigenvalue of its matrix argument	38
\mathbf{W}_L	$L \times L$ DFT matrix	27
ξ_{mf}	MF-GLRT test statistic	69
ξ_{rs}	RS-GLRT test statistic	70
ξ_{ss}	SS-GLRT test statistic	38
ξ_{ss}^i	portion of ξ_{ss} associated with the i th transmit channel	39
ζ_1^i	non-zero eigenvalue of $\mathbf{\Omega}_1^i$	72
ζ_p^{ij}	RS-GLRT surveillance channel loss due to mismatch between the actual and hypothesized target angles	76
ζ_{rr}^i	non-zero eigenvalue of $\mathbf{\Omega}_{rr}^i$	71
ζ_{ss}^i	non-zero eigenvalue of $\mathbf{\Omega}^i$	40

PASSIVE MIMO RADAR DETECTION

I. Introduction

This dissertation advances the theory of passive multiple-input multiple-output (MIMO) radar detection. It also unifies passive MIMO radar (PMR), active MIMO radar (AMR), and passive source localization (PSL) sensor networks within a common theoretical framework. This chapter introduces PMR in Sec. 1.1, AMR and PSL in Sec. 1.2, and discusses the relevance of passive radar to the United States Air Force in Sec. 1.3. Current approaches to passive radar detection and their shortcomings are discussed in Sec. 1.4, and the methodology used to address these shortcomings in Sec. 1.5. The contributions of this research are summarized in Sec. 1.6, followed by an outline of the remainder of this dissertation in Sec. 1.7.

1.1 Passive Radar

Passive radar is a type of radar that exploits non-cooperative radio frequency (RF) transmissions to detect, localize, track and/or image objects of interest. *Non-cooperative transmitters*, also known as illuminators of opportunity, operate separate from and independent of the passive radar system. Example non-cooperative transmitters include commercial broadcast transmitters, cellular phone base stations, navigation satellites, and air surveillance radars [88]. The use of non-cooperative transmitters distinguishes passive radar from active radar. Consequently, a passive radar system contains only receivers, and it must select from the illuminators within its operating environment. This enables covert operation, yet also presents challenges that constrain performance in terms of sensitivity, resolution, and ambiguity [31].

Passive radar dates to the earliest days of radar. In 1935, Sir Robert Watson-Watt detected an aircraft using shortwave broadcasts from the Daventry British Broadcasting Corporation Empire transmitter [57]. During World War II, the German system *Klein Heidelberg* exploited transmissions from the British *Chain Home* air surveillance radar to passively detect Allied bombers [32]. In the 1980s and 1990s, researchers in the United States and the United Kingdom revisited using commercial broadcast transmitters for aircraft detection [34, 45, 46]. Several demonstration systems resulted, including Lockheed Martin’s *Silent Sentry*, which exploits multiple frequency modulated (FM) radio transmitters to track aircraft [7]. Interest in passive radar grew rapidly in the wake of these investigations. Fig. 1 depicts the number of passive radar publications that appeared in the English-language technical literature from 1999 to 2011. Many prototype systems were reported during this period. Three prominent examples include: *Passive Radar Demonstrator* (PaRaDe), developed by the *Institute of Electronic Systems* at the *Warsaw University of Technology* [59, 60]; *COvert RADar* (CORA), developed by the German *Fraunhofer Institute for High Frequency Physics and Radar Techniques* (FHR) [55]; and *Gruppenantenne für militärische Mobilfunk Aufklärung*¹ (GAMMA), developed by the German *Fraunhofer Institute for Communication, Information Processing and Ergonomics* (FKIE) [65, 91].

While most reported passive radar systems use only a single illuminator type, a growing number of multiband systems are also under development [8, 28, 56, 73]. The term *multiband* refers to the simultaneous exploitation of different illuminator types across multiple frequency bands. For instance, the *Cassidian Demonstrator* exploits FM radio and digital audio broadcast (DAB) signals in the very high frequency (VHF) band and terrestrial digital video broadcast (DVB-T) signals in the ultra high frequency (UHF) band [73]. Multiband operation increases frequency diversity and

¹German for *Array Antenna for Mobile Military Reconnaissance*

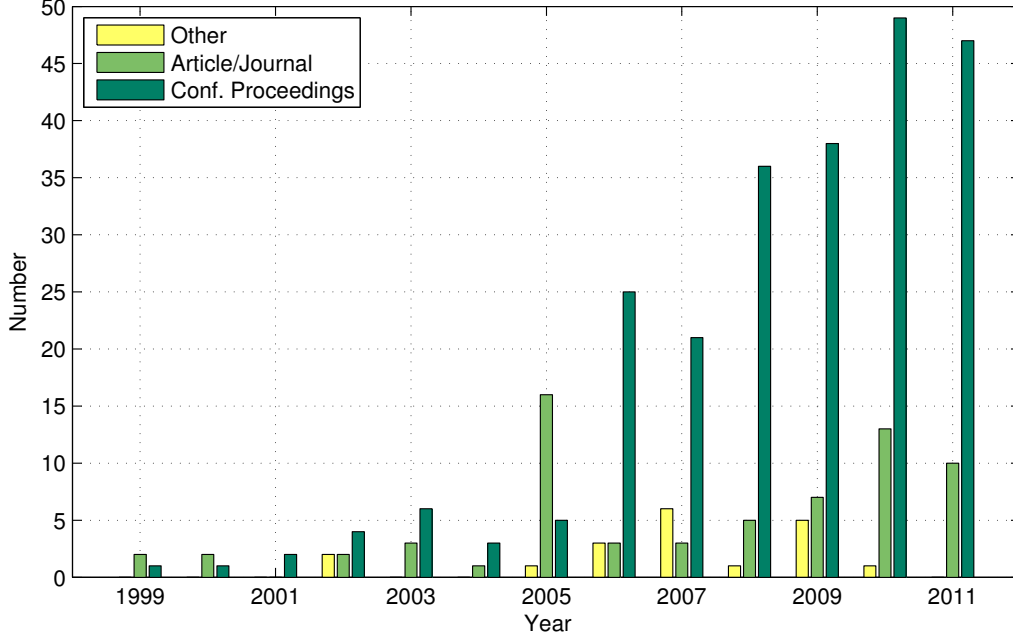


Figure 1. Passive Radar Publications by Year and Type

geometric diversity in comparison to single-band operation, and thereby provides both detection and localization advantages. Both types of diversity increase the number of independent samples of the target’s reflectivity signature, which typically decorrelates with frequency and angle, available to the radar system for processing. The resulting detection improvement is termed *diversity gain* [24]. Geometric diversity also increases the probability the target Doppler is unmasked from clutter interference in at least one bistatic (transmitter-receiver) channel; this is termed *geometry gain* [26]. Finally, the additional measurement degrees-of-freedom provided by geometric diversity enables direct localization of targets in Cartesian space [39, 63].

In addition to multiband operation, airborne operation has also received significant interest in recent years [13, 22, 52]. Airborne operation extends the range of viable passive radar operating modes to include synthetic aperture radar imaging and ground moving target indication, while at the same time complicating the detection problem by introducing Doppler-spread clutter. To assess the prospects of airborne

passive radar, the North Atlantic Treaty Organization established an international task group in 2012 to “comprehensively research the current state of the art of airborne passive radar, identify technological challenges including hardware and signal processing development, identify end user requirements, and address operational usefulness” [1]. While only FM radio appears to have been used in experimental airborne passive radar trials to date [13, 22], DVB-T has also been identified as a candidate illuminator for airborne operation [52].

1.1.1 Network Topology.

Although passive radar systems have only receivers, a passive radar system and the non-cooperative transmitters exploited by that system are sometimes described as a passive radar *network*. The topology of such networks is described as *bistatic*, *multistatic*, or *multiple-input multiple-output*, depending on the number of receiver sites and the number of exploited non-cooperative transmitters. These topologies are illustrated in Fig. 2. *Passive bistatic radar* (PBR) consists of one receiver and one non-cooperative transmitter (Fig. 2a). *Passive multistatic radar* consists of either: (1) one receiver that exploits multiple non-cooperative transmitters (Fig. 2b); or (2) multiple geographically separated receivers that exploit one non-cooperative transmitter (Fig. 2c). Type 1 is more common than type 2 due to the availability of transmitters and the simplicity of using one receiver site. Finally, *passive MIMO radar* (PMR) consists of multiple geographically separated receivers and multiple non-cooperative transmitters (Fig. 2d). In comparison, PMR is the most general passive radar topology, as both bistatic and multistatic systems may be regarded as special cases of PMR. Consequently, PMR is the primary focus of this work.

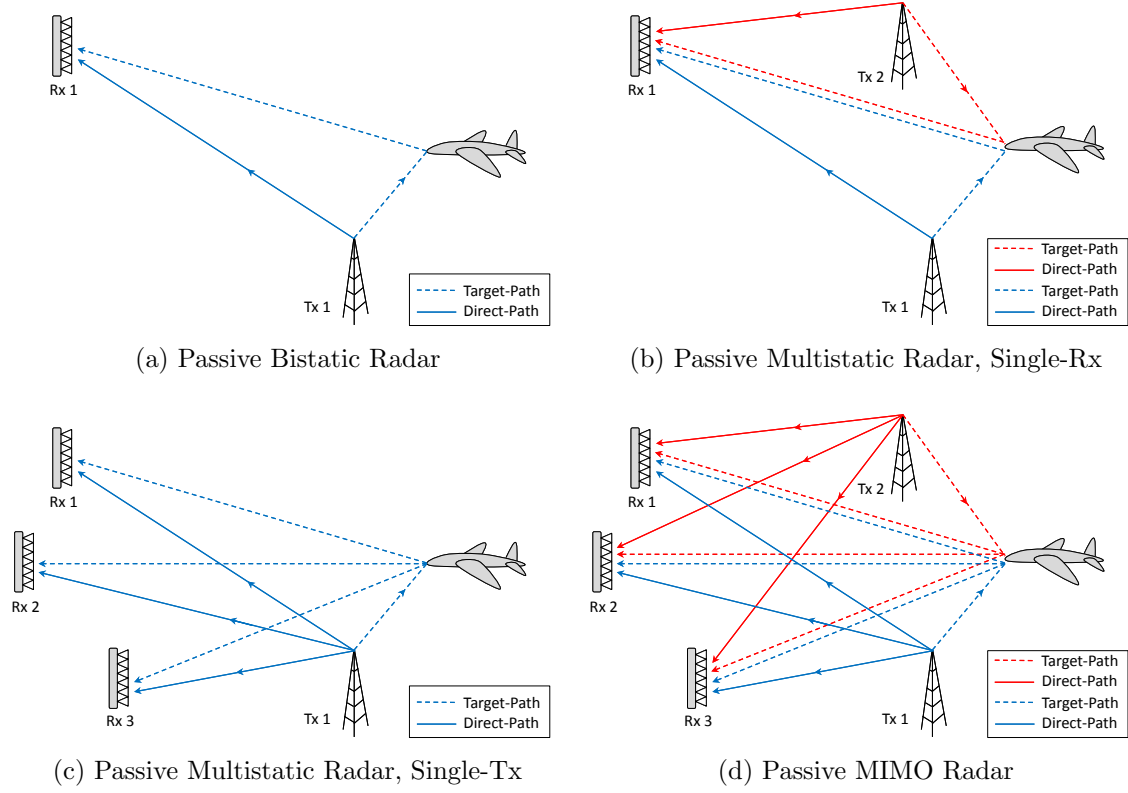


Figure 2. Passive Radar Network Topologies

1.1.2 Signal Environment.

In the PMR signal environment, direct-path (i.e., transmitter-to-receiver) and target-path (i.e., transmitter-to-target-to-receiver) signals from each transmitter are incident at each receiver. This is illustrated in Fig. 2d. The transmitters within a PMR network typically occupy distinct frequency channels. However, some commercial illumination types, including DVB-T and DAB, may operate as single frequency networks, in which multiple geographically separated transmitters emit the same signal on the same frequency channel. Exploitation of single frequency networks complicates the detection and tracking problem because it introduces measurement origin uncertainty, i.e., the passive radar receiver does not know *a priori* which detections go with which transmitters [79]. Sophisticated algorithms are required to resolve this

uncertainty [9, 21]. This work considers only frequency-separable transmissions.

Many commercial transmitters emit continuously or with high duty cycle, e.g., radio, television, and cellular phone emitters. Such transmitters are termed continuous wave (CW)². Consequently, direct-path and target-path signals are often received simultaneously. This causes *direct-path self-jamming*, which can degrade detection sensitivity due to the large power ratio between direct-path and target-path signals typical in passive radar scenarios [33]. Indeed, power ratios exceeding 100 dB have been reported [27]. To counter this obstacle, a passive radar receiver must have large dynamic range and employ one or multiple direct-path interference suppression techniques [33]. Two common interference suppression techniques are: (1) adaptive beamforming [36, 78, 91], in which nulls are placed in the interference direction(s); and (2) adaptive filtering [15, 19, 35, 62, 69], in which the interfering signals are estimated and cancelled via subtraction. In addition, clutter-path (i.e., transmitter-to-clutter-to-receiver) signals are also typically incident at each receiver. Clutter-path interference presents many of the same challenges as direct-path interference and is countered using many of the same techniques.

1.2 Related RF Sensor Networks

Although PMR is the primary focus of this dissertation, AMR and PSL sensor networks are also discussed for comparison. This clarifies the unique properties of PMR, and enable AMR, PMR, and PSL to be understood within a common theoretical framework. AMR and PSL are briefly described in the following sections.

²As opposed to *pulsed*.

1.2.1 Active MIMO Radar.

Active MIMO radar, illustrated in Fig. 3, is defined as a system that detects and localizes targets using multiple distributed transmit-receive (Tx-Rx) nodes and multiple separable signals [41]. Note that this type of MIMO is also described in the literature by the terms statistical MIMO [24], noncoherent MIMO [66], and distributed MIMO [85]³. AMR is distinguished from PMR by the use of cooperative transmitters that transmit known signals. These signals are specially designed to be separable in one of several possible domains (time, frequency, Doppler, or code) [89]. Due to this separability, the scattered returns from each transmitted signal can be isolated at each receiver. The optimal Neyman-Pearson detector for AMR detection performs matched filtering per transmitter-receiver pair, noncoherent integration across pairs, and thresholding [14, 20, 24, 26, 43]. Noncoherent integration is necessitated by the non-isotropic (non-coherent) scattering of complex targets with respect to the transmitter-receiver pairs in MIMO topologies.

³This work does not refer to the type of MIMO radar that uses closely-spaced transmitters.

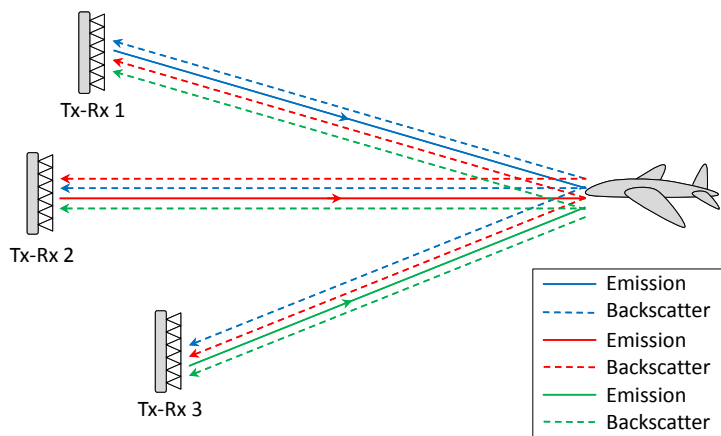


Figure 3. An Active MIMO Radar Sensor Network

1.2.2 Passive Source Localization.

Passive source localization sensor networks, depicted in Fig. 4, detect and localize targets by intercepting and processing target-emitted signals. In comparison to PMR, a PSL system detects target-emitted rather than target-scattered signals, and these signals are often unknown *a priori* to the PSL system, as in PMR. The detection and localization processing in PSL sensor networks is typically based on pairwise processing of the received signals across receivers. Conventional approaches to target localization follow a two-step procedure in which intermediate parameters are (1) measured and then (2) combined to estimate the emitter position and velocity. Such approaches have utilized one or multiple measurement types, including: angle-of-arrival (AOA) [25, 76]; time difference of arrival (TDOA) between receiver pairs [16, 80]; and frequency difference of arrival (FDOA) between receiver pairs, also termed differential Doppler [16, 58]. More recently, centralized approaches that detect and localize emitters by operating directly on all received signals have also been proposed [5, 12, 83, 86, 87].

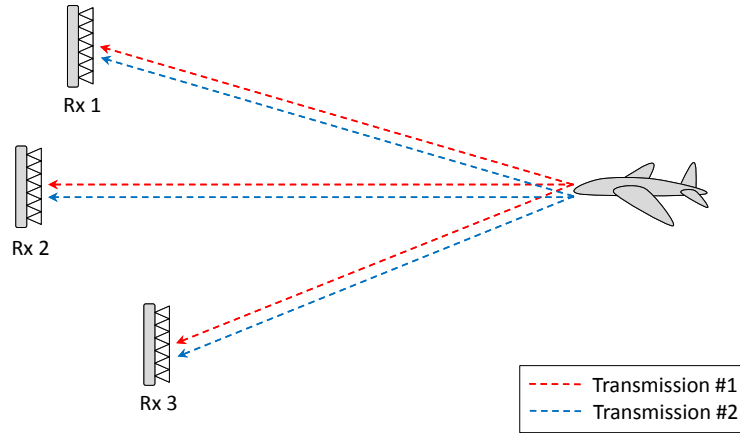


Figure 4. A Passive Source Localization Sensor Network

1.3 Relevance to United States Air Force

The mission of the United States Air Force is “to fly, fight, and win. . .in air, space, and cyberspace” [2]. Airborne passive radar contributes to this mission in several ways. First, near-peer adversaries are developing anti-access/area denial (A2/AD) technologies to limit the projection of US power into strategic places [4]. Passive radar counters these technologies by providing a passive means to attain air situational awareness in contested environments where RF emissions are precluded by survivability considerations. Second, airborne passive radar is less susceptible to electronic attack than active radar in contested electromagnetic environments. The covertness provided by passive radar makes it difficult to jam a passive radar system, and thereby provides an inherent type of electronic protection. Third, a congested RF spectrum aids rather than degrades passive radar by providing the passive radar many candidate illuminators to exploit. This contrasts with active radar, which must operate within spectral gaps to prevent destructive interference. Finally, the use of transmitters of opportunity enables the exploitation of restricted frequency bands not otherwise available for radar use, e.g., various VHF and UHF commercial broadcast bands. In all of these ways, airborne passive radar contributes to the United States Air Force core functions of *air superiority* and *global precision strike* [23].

1.4 Current Shortcomings

Although the potential of passive radar has been demonstrated experimentally, a rigorous theoretical foundation for passive radar detection does not yet exist. This is particularly true for PMR systems, as the majority of the existing research has focused on bistatic and multistatic topologies. In the following, two current approaches to passive radar detection are described, and their shortcomings are discussed. The first, referred to as *detection with references*, is the approach used by all reported

experimental passive radar systems. The second, referred to as *detection without references*, is a recently proposed technique for detection in multiple-receiver passive radar topologies. Due to its prevalence, *detection with references* is also referred to as the *conventional approach*, while *detection without references* is referred to as the *alternative approach*. Both are discussed in turn.

1.4.1 PMR Detection with References.

The conventional approach to detection in passive radar is based on matched filtering. For each bistatic (transmitter-receiver) pair, the passive radar receiver isolates the direct-path and target-path signals into *reference* and *surveillance* channels, respectively. This is accomplished by pointing directional antennas at the transmitter and the anticipated target region, respectively [11, 67], or by digital beamforming in multichannel systems [27, 60, 74, 78, 91], as shown in Fig. 5. Adaptive filtering is applied to the surveillance channels to mitigate direct-path and clutter-path interference [15, 19, 35, 62, 69], and equalization techniques are applied to the reference channels to further isolate the direct-path signals [17, 77, 92]⁴. The cross-ambiguity function (CAF) between the reference and surveillance channels is then computed, and target detection is declared for CAF cells that exceed a threshold value. The bistatic range, bistatic Doppler, and angle-of-arrival measurements from all such detections are then fused to localize and track targets in Cartesian space [21, 50, 61, 63, 73]. Note that this approach is *decentralized* in that detection is performed separately by each bistatic pair, and the resulting detections are fused in subsequent processing.

Although this approach often works in practice, it is *ad hoc* because it simply mimics the matched filtering operation used in active radar. Specifically, calculation of the reference-surveillance CAF approximates the matched filtering operation in ac-

⁴Demodulation-remodulation of the reference channels is also often performed for digital transmissions [6, 18, 54, 68, 75, 92].

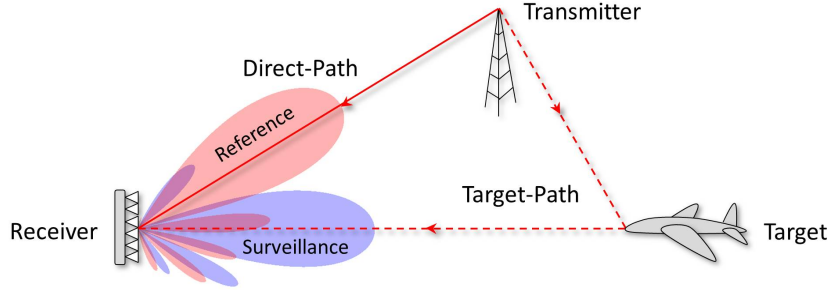


Figure 5. Reference and Surveillance Channel Formation

tive radar, where the reference channel provides an estimate of the *a priori* unknown transmit signal. However, matched filtering is only optimal in the Neyman-Pearson sense when the transmit signal is known exactly, as in active radar. In high direct-path-to-noise ratio (DNR) scenarios, the reference channel provides a high-quality estimate of the transmitted signal, and close to optimal (matched) detection sensitivity is achieved. This is the case in many scenarios of interest. However, if the direct-path signal has low DNR, then the reference channel is mismatched to the originally transmitted signal, and detection sensitivity is degraded in proportion to this mismatch. Although such mismatch is mitigated to some degree by reference channel equalization, it cannot be removed completely⁵. Therefore, the conventional approach is best suited for high-DNR scenarios.

1.4.2 PMR Detection without References.

An alternative detection approach has recently been proposed that does not utilize direct-path signals [84, 10]. In this approach, target-path signals from multiple widely-separated receivers are isolated and cross-correlated after appropriate delay-Doppler compensation. This approach applies only to multiple-receiver multistatic and MIMO topologies, and it resembles techniques used for source detection in PSL

⁵Even after perfect demodulation-remodulation of digital signals, mismatch still results between the transmitted and reconstructed signals due to transmitter-specific effects such as in-phase/quadrature channel mismatch and carrier drift [75].

sensor networks [83, 40]. It is also *centralized* rather than decentralized because it jointly processes all measured target-path signals to detect and localize targets.

Since this approach does not process direct-path signals, it is not degraded in low-DNR scenarios, unlike the conventional approach. Rather, low-DNR scenarios aid this approach by minimizing direct-path interference, which simplifies isolation of the target-path signals. Such scenarios are rare in practice [30], but could result if there is physical blockage of the line-of-sight paths between transmitters and receivers (e.g., the Manastash Ridge Radar [88, p. 121]), or if the illuminators utilize highly directive transmission and/or null the receiver directions. The resulting signal environment is illustrated in Fig. 6. However, by ignoring direct-path signals, this approach ignores a potentially useful source of information about the unknown transmit signals. This is particularly true in high-DNR scenarios, in which the direct-path signal provides a high-quality reference that can be used for (noisy) matched filtering, as in the conventional approach. Thus, this alternative reference-less approach is better suited for low-DNR scenarios than high-DNR scenarios.

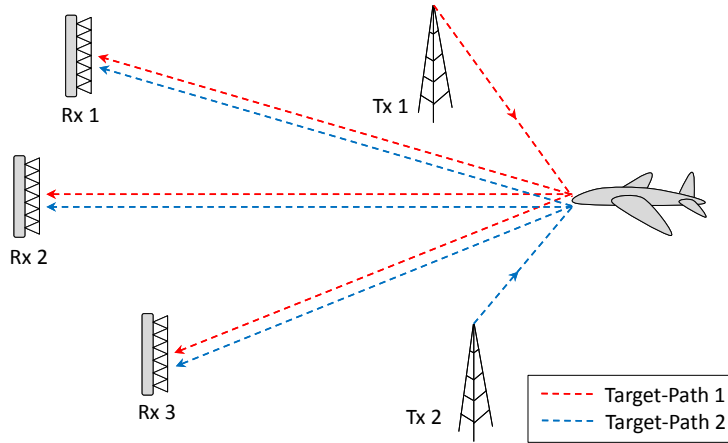


Figure 6. Passive MIMO Radar without Direct-Path References

1.5 Research Hypothesis and Methodology

Both of the detection approaches discussed in Sec. 1.4 represent partial rather than general solutions to the passive radar detection problem. This is because both approaches are based on incomplete views of the passive radar signal environment. The conventional approach assumes reception of distortionless direct-path signals, while the alternative approach ignores direct-path signals completely. In general, direct-path signals are present but distorted. Consequently, neither approach exploits the passive radar signal environment to full advantage. This motivates the hypothesis of this research program: *formulating the passive radar detection problem in terms of the actual received signal, which minimally includes the target-path signal, the direct-path signal, and receiver noise, will result in a detector that is suitable under all DNR conditions.* The performance of such a detector is expected to approximate the performance of the two current approaches under the appropriate DNR conditions, i.e., its sensitivity would approximate that of the conventional and alternative approaches under high- and low-DNR conditions, respectively. Furthermore, its performance would vary smoothly between these two extremes as a function of DNR. Consequently, it would represent a general solution to the passive radar detection problem.

Accordingly, the methodology of this research program is to: (a) formulate the PMR detection problem to account for target-path signals, direct-path signals, and receiver noise in the detection hypotheses; (b) derive the generalized likelihood ratio test (GLRT) for the resulting composite hypothesis testing problem; (c) investigate the probability distributions of the resulting test statistic under both hypotheses; (d) illustrate the detection and ambiguity properties of the resulting detector via numerical simulation; and (e) compare the detection and ambiguity performance of this detector to that of analogous GLRT detectors for AMR and PSL sensor networks.

1.6 Research Contributions

The main contributions of this research are:

1. The derivation and statistical characterization of a novel detector for the centralized PMR detection *without* direct-path references problem (Chapter III)
2. The derivation and statistical characterization of a novel detector for the centralized PMR detection *with* direct-path references problem (Chapter IV)
3. The introduction of a unified framework for detection in active and passive distributed RF sensor networks that encompasses active MIMO radar, passive MIMO radar, and passive source localization sensor networks (Chapter V)

Each contribution is described in detail in the following sections.

1.6.1 PMR Detection without References.

A novel GLRT detector is derived for centralized PMR detection without direct-path references, termed the surveillance-surveillance GLRT (SS-GLRT) because it performs pairwise processing of surveillance channels [38]. This detector extends prior formulations to account for multiple non-cooperative transmitters and multi-channel (array) receivers. These extensions significantly enhance probability of detection and reduce detection ambiguity. Then, using recent results from random matrix theory, the exact distribution of the detection test statistic is identified under both hypotheses. This is the first appearance of such distributions in the context of radar detection. These distributions show that detection sensitivity is only a function of the number of received signal samples, the number of transmitters and receivers in the PMR network, and the average target-path input signal-to-noise ratio (SNR). Furthermore, numerical examples demonstrate important properties of the detector, namely, that (a) receivers and transmitters contribute asymmetrically to detection

sensitivity (which is uncommon in radar detection), (b) integration gain grows non-coherently with increasing signal length, and (c) salient features of its ambiguity function can be explained in terms of TDOA, FDOA, and AOA.

1.6.2 PMR Detection with References.

A novel GLRT detector is derived for centralized PMR detection with direct-path references, termed the reference-surveillance GLRT (RS-GLRT) because it processes both reference and surveillance channels [37]. This detector extends the formulation of the SS-GLRT to include direct-path signals with arbitrary DNRs. It is shown that calculation of the RS-GLRT test statistic, which is expressed in terms of the largest eigenvalues of complex Wishart matrices, entails operations that may be interpreted as isolating the target-path and direct-path signals into surveillance and reference channels, respectively. Although the exact distribution of this test statistic appears to not exist under either hypothesis, it is shown that this statistic is approximately proportional under high-DNR conditions to a GLRT statistic for AMR detection, termed the matched filter GLRT (MF-GLRT), for which probability distributions are known under both detection hypotheses. It is also shown that: (a) its sensitivity is only a function of the number of received signal samples, the number of transmitters and receivers in the PMR network, the average target-path input SNR, *and* the average input DNR; and (b) salient features of its ambiguity function can be explained in terms of bistatic range, bistatic Doppler, and AOA. The RS-GLRT is the first PMR detector that shows how detection sensitivity depends on target-path SNR *and* DNR. Consequently, the RS-GLRT represents a general solution to the passive radar detection problem and confirms the research hypothesis.

1.6.3 Unified Detection Framework.

Finally, a novel theoretical framework for detection in active and passive distributed RF sensor networks is proposed. This framework, illustrated in Fig. 7, encompasses AMR, PMR, and PSL sensor networks. It identifies how AMR, PMR, and PSL are related by simple transformations of their signal environments. These relationships reveal that PMR is the key to linking AMR and PSL, which have traditionally been regarded as distinct, and suggest that PMR detection might exhibit properties of detection in both AMR and PSL sensor networks. Analysis of the RS-GLRT and SS-GLRT detectors shows this is true, i.e., PMR detection performance (sensitivity and ambiguity) varies between that of AMR and PSL as a function of the average DNR. In high-DNR scenarios, RS-GLRT performance approaches MF-GLRT performance, which is the GLRT for AMR sensor networks. In low-DNR scenarios, RS-GLRT performance approaches SS-GLRT performance, which is the GLRT detector for both PMR without references and PSL sensor networks. This is explained by observing that PSL and AMR represent two extremes in terms of knowledge about the transmitted signals, i.e., the signals are entirely unknown in PSL and entirely known in AMR. Direct-path signals provide PMR a varying degree of knowledge about the transmit signals that is quantified by the DNR. Thus, PMR unifies PSL and AMR within a common theoretical framework. This result provides fundamental insight into the natures of active and passive distributed RF sensing.

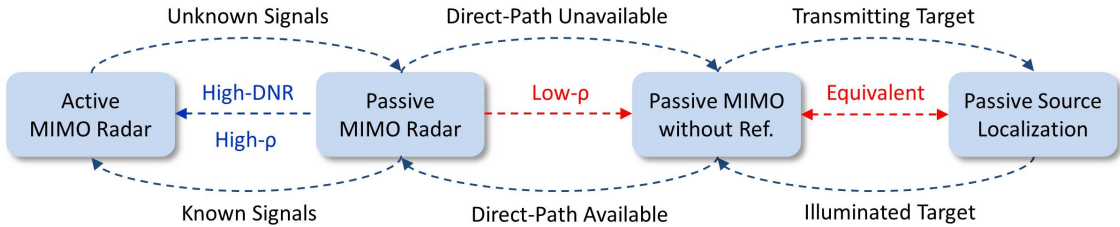


Figure 7. A Unified Framework for Active and Passive Distributed RF Sensing

1.7 Chapter Outline

The remainder of this dissertation is organized as follows:

Chapter II: presents a signal model for PMR.

Chapter III: considers the PMR detection *without* direct-path references problem.

The SS-GLRT detector is derived, and its detection and ambiguity performance is analyzed and illustrated via numerical simulation. PMR detection without direct-path references is shown to be equivalent to PSL detection.

Chapter IV: considers the PMR detection *with* direct-path references problem. The

RS-GLRT detector is derived, and its detection and ambiguity performance is analyzed and illustrated via numerical simulation. PMR detection performance is shown to vary between that of detection in AMR and PSL sensor networks in a manner that depends on the DNR.

Chapter V: presents the unified theoretical framework for detection in active and passive distributed RF sensor networks.

Chapter VI: summarizes the main contributions of this research, and discusses how it can be extended in future work.

II. Signal Model

This chapter presents a signal model for PMR that underlies Chapters III-V.

2.1 Scenario

Consider a scenario with N_t transmitters, N_r receivers, and one target. Fig. 8 depicts the geometry of the ij th transmitter-receiver pair, which consists of the i th transmitter and j th receiver. The position and velocity of the i th transmitter are denoted by \mathbf{d}^i and $\dot{\mathbf{d}}^i$, $i = 1 \dots N_t$, the position and velocity of the j th receiver by \mathbf{r}^j and $\dot{\mathbf{r}}^j$, $j = 1 \dots N_r$, and the target position and velocity by \mathbf{t} and $\dot{\mathbf{t}}$. The time dependence of \mathbf{d}^i , $\dot{\mathbf{d}}^i$, \mathbf{r}^j , $\dot{\mathbf{r}}^j$, \mathbf{t} , and $\dot{\mathbf{t}}$ is implicit to simplify notation; in general, transmitters, receivers, and the target may be in motion. Define $R_0^{ij}(t)$ as the direct-path range between the i th transmitter and j th receiver, $R_0^{ij}(t) = \|\mathbf{r}^j - \mathbf{d}^i\|$. Similarly, let $R_1^i(t) = \|\mathbf{t} - \mathbf{d}^i\|$ and $R_2^j(t) = \|\mathbf{r}^j - \mathbf{t}\|$ denote the lengths of the first and second legs of the ij th target-path channel between the i th transmitter, target, and j th receiver.

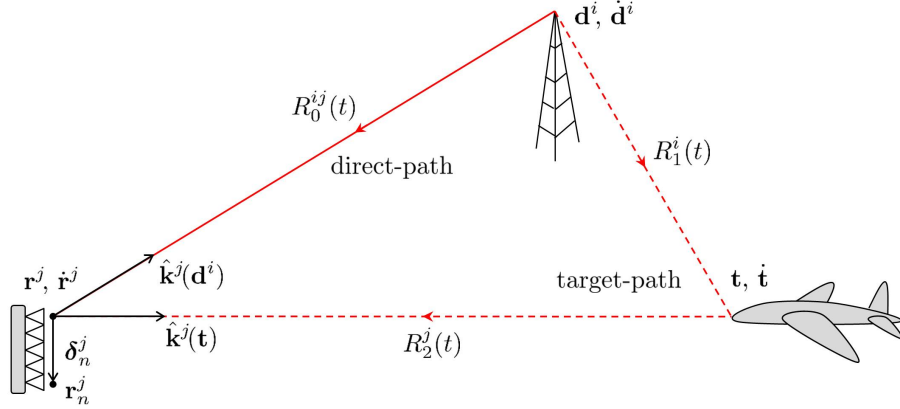


Figure 8. Geometry for the ij th Transmitter-Receiver Pair

The j^{th} receiver is assumed to have an array antenna consisting of N_e^j identical elements, with the n th element at location $\mathbf{r}_n^j = \mathbf{r}_1^j + \boldsymbol{\delta}_n^j$, where $\mathbf{r}_1^j = \mathbf{r}^j$ is the location of

the reference element, and $\boldsymbol{\delta}_n^j$ is the offset vector pointing from the reference element to the n th element, as shown in Fig. 8. Note that $\boldsymbol{\delta}_1^j = \mathbf{0}$. For simplicity, all arrays are assumed to have an equal number of array elements, i.e., $N_e^j = N_e$ for all j . Let $G_{e,n}^j(\mathbf{x})$ denote the element pattern of the n th element in the direction of \mathbf{x} . For simplicity, it is assumed that element patterns are equal across array elements within a given array, i.e., $G_{e,n}^j(\mathbf{x}) = G_e^j(\mathbf{x})$ for all n . Such a condition approximately holds for the aligned array elements within a planar array (e.g., GAMMA [65]), or for the azimuthally-isotropic elements within a circular array (e.g., PaRaDe [59]). Finally, let $\hat{\mathbf{k}}_n^j(\mathbf{x})$ denote the unit vector pointing from the n th element of the j th receiver to the position \mathbf{x} , i.e.,

$$\hat{\mathbf{k}}_n^j(\mathbf{x}) = \frac{\mathbf{x} - \mathbf{r}_n^j}{\|\mathbf{x} - \mathbf{r}_n^j\|} \quad (1)$$

For \mathbf{x} in the far field, $\hat{\mathbf{k}}_n^j(\mathbf{x}) \approx \hat{\mathbf{k}}_1^j(\mathbf{x}) \triangleq \hat{\mathbf{k}}^j(\mathbf{x})$, i.e., the unit vectors pointing from the array elements to a location in the far field are approximately equal.

2.2 Signal Environment

The i^{th} transmitter generates a continuous wave (CW)¹ narrowband bandpass waveform $\tilde{u}^i(t)$ with analytic representation

$$\tilde{u}^i(t) = u^i(t) e^{j\omega_c^i t}, \quad t \in [0, T] \quad (2)$$

where j is the imaginary unity, ω_c^i is the carrier frequency, T is the coherent processing interval (CPI), and $u^i(t)$ is the complex envelope with frequency representation $U^i(\omega)$ and bandwidth B^i in Hertz, $U^i(\omega) \approx 0$ for all $|\omega| > \pi B^i$. The transmitted signals $\{\tilde{u}^i(t) : i = 1 \dots N_t\}$ are assumed to occupy non-overlapping frequency channels such that they are separable in frequency. The complex envelope $u^i(t)$ is assumed to be

¹The term continuous wave is used to denote a signal with continuous transmission.

defined such that the energy of $\tilde{u}^i(t)$, denoted E^i , is given by

$$E^i = \int_0^T |\tilde{u}^i(t)|^2 dt = \int_0^T |u^i(t)|^2 dt = T \quad (3)$$

Note that this condition is satisfied for unit-modulus signals, $|u^i(t)|^2 = 1$.

The signal $\tilde{u}^i(t)$ is presented to the i th transmitter's aperture and radiated into the environment. This signal propagates to the j th receiver along the direct-path (transmitter-to-receiver) and target-path (transmitter-to-target-to-receiver) channels, as depicted in Fig. 8. It also propagates to the j th receiver along multiple clutter-path (transmitter-to-clutter-to-receiver) channels. The resulting clutter-path signals may be mitigated by adaptive spatial and temporal filtering as discussed in Sec. 1.1.2; consequently, they are ignored in the following. The signal received at the n th element of the j th receiver is the superposition of the direct-path and target-path signals from all transmitters within the receiver bandwidth and receiver noise. It is given by

$$\tilde{s}_n^j(t) = \sum_{i=1}^{N_t} a_d^{ij}(t) \tilde{u}^i(t - \tau_{d,n}^{ij}(t)) + \sum_{i=1}^{N_t} \alpha^{ij} a_t^{ij}(t) \tilde{u}^i(t - \tau_{t,n}^{ij}(t)) + \tilde{n}_n^{ij}(t) \quad (4)$$

where $a_d^{ij}(t)$ and $a_t^{ij}(t)$ denote real amplitude scaling coefficients associated with the direct-path and target-path channels, respectively, α^{ij} is the target's complex bistatic reflectivity associated with the ij th bistatic pair, $\tau_{d,n}^{ij}(t)$ and $\tau_{t,n}^{ij}(t)$ denote the propagation time delays associated with the direct-path and target-path channels, respectively, and $\tilde{n}_n^j(t)$ is wide-sense stationary (WSS) bandpass Gaussian white noise with power spectral density (PSD) $\tilde{P}_n^j(\omega) = N_0$ over $|\omega - \omega_c^j| \leq \pi B^j$, given a receiver bandwidth B^j in Hertz and center frequency ω_c^j . The channel coefficients $a_d^{ij}(t)$ and $a_t^{ij}(t)$ account for the composite amplitude scaling of $\tilde{u}^i(t)$ associated with transmission, propagation, and reception along the direct-path and target-path

channels, respectively. They are defined by

$$a_d^{ij}(t) = \sqrt{\frac{P_{\text{erp}}^i(\mathbf{r}^j)\lambda^{i2}G_e^j(\mathbf{d}^i)}{(4\pi)^2(R_0^{ij}(t))^2}} \quad (5)$$

$$a_t^{ij}(t) = \sqrt{\frac{P_{\text{erp}}^i(\mathbf{t})\lambda^{i2}G_e^j(\mathbf{t})}{(4\pi)^3(R_1^i(t)R_2^j(t))^2}} \quad (6)$$

where P_{erp}^i is the i th transmitter's effective radiated power toward \mathbf{x} , $\lambda^i = c/f_c^i$ is the wavelength of the i th transmitter, c is the speed of light, and $f_c^i = 2\pi/\omega_c^i$. Note that $R_0^{ij}(t)$, $R_1^i(t)$ and $R_2^j(t)$ are not expected to change significantly over the interval $[0, T]$. Consequently, let $a_d^{ij} \triangleq a_d^{ij}(t)|_{t=0}$ and $a_t^{ij} \triangleq a_t^{ij}(t)|_{t=0}$.

The signal $\tilde{s}_n^j(t)$ is down-converted and channelized in frequency to extract the complex baseband signal for each transmit channel. The resulting complex baseband signal for the i th channel, denoted $s_n^{ij}(t)$, is given using (2) and (4) by

$$\begin{aligned} s_n^{ij}(t) &= \text{LPF}^i \left\{ \tilde{s}_n^j(t) e^{j(\theta^j - p\omega_c^i t)} \right\} \quad (7) \\ &= a_d^{ij} e^{j(\theta^j - \omega_c^i \tau_{d,n}^{ij}(t))} u^i(t - \tau_{d,n}^{ij}(t)) + \alpha^{ij} a_t^{ij} e^{j(\theta^j - \omega_c^i \tau_{t,n}^{ij}(t))} u^i(t - \tau_{t,n}^{ij}(t)) + n_n^{ij}(t) \quad (8) \end{aligned}$$

where θ^j in (7) denotes an unknown phase associated with the j th receiver's downconversion oscillator, $\text{LPF}^i\{\cdot\}$ denotes a low pass filter that is matched to the bandwidth of the i th transmit channel, and $n_n^{ij}(t)$ is WSS complex baseband Gaussian white noise with PSD $P_n^{ij}(\omega) = N_0$ over $|\omega| \leq \pi B^i$. Note that the unknown phase θ^j in (7) indicates that the receivers are not phase-synchronized (coherent). Achieving coherence between widely distributed receivers is difficult in practice. However, the receivers are considered to be time-synchronized in the sense that they are aligned in time to within a small fraction of the resolution time of the each transmit channel, i.e., to within a small fraction of $1/B^i$ for all i . The direct-path and target-path components of (8) are discussed in turn.

2.2.1 Direct-Path Signal.

Let $s_{d,n}^{ij}(t)$ denote the direct-path component of (8),

$$s_{d,n}^{ij}(t) = a_d^{ij} e^{j(\theta^j - \omega_c^i \tau_{d,n}^{ij}(t))} u^i(t - \tau_{d,n}^{ij}(t)) \quad (9)$$

where $\tau_{d,n}^{ij}(t) = R_{0,n}^{ij}(t)/c$, and $R_{0,n}^{ij}(t)$ is the range between the i th transmitter and the n th element of the j th receiver array. The direct-path range can be expanded into a sum of two terms,

$$R_{0,n}^{ij}(t) = R_0^{ij}(t) + \Delta R_n^{ij}(t; \mathbf{d}^i) \quad (10)$$

where $R_0^{ij}(t)$ is the range between the i th transmitter and the reference element of the j th receiver, and $\Delta R_n^{ij}(t; \mathbf{d}^i)$ is the differential range of the n th array element with respect to the reference element. For \mathbf{d}^i in the far-field, it is shown in Appendix A that $\Delta R_n^{ij}(t; \mathbf{d}^i)$ may be approximated

$$\Delta R_n^{ij}(t; \mathbf{d}^i) \approx -\hat{\mathbf{k}}^j(\mathbf{d}^i) \cdot \boldsymbol{\delta}_n^j \quad (11)$$

Note that for \mathbf{d}^i in the far-field, $\hat{\mathbf{k}}^j(\mathbf{d}^i)$ is approximately constant over $t \in [0, T]$. Therefore, $\Delta R_n^{ij}(\mathbf{d}^i) \triangleq \Delta R_n^{ij}(t; \mathbf{d}^i)|_{t=0}$ is used in the following. From (10), the propagation delay $\tau_{d,n}^{ij}(t)$ can then be expressed as

$$\tau_{d,n}^{ij}(t) = \tau_d^{ij}(t) + \Delta \tau_n^{ij}(\mathbf{d}^i) \quad (12)$$

where $\tau_d^{ij}(t) = R_0^{ij}(t)/c$ and $\Delta \tau_n^{ij}(\mathbf{d}^i) = \Delta R_n^{ij}(\mathbf{d}^i)/c$.

Inserting (12) into (9),

$$s_{d,n}^{ij}(t) = a_d^{ij} e^{j(\theta^j - \omega_c^i \Delta \tau_n^{ij}(\mathbf{d}^i))} u^i(t - \tau_d^{ij}(t) - \Delta \tau_n^{ij}(\mathbf{d}^i)) e^{-j\omega_c^i \tau_d^{ij}(t)} \quad (13)$$

Note that the only remaining dependence on the element index n is in the complex exponential $e^{-j\omega_c^i \Delta\tau_n^{ij}(\mathbf{d}^i)}$. Let $\vartheta_n^{ij}(\mathbf{d}^i)$ denote the phase of this complex exponential, which can be written using (11) as

$$\vartheta_n^{ij}(\mathbf{d}^i) \triangleq -\omega_c^i \Delta\tau_n^{ij}(\mathbf{d}^i) \quad (14)$$

$$= -\left(\frac{\omega_c^i}{c}\right) \Delta R_n^{ij}(\mathbf{d}^i) \quad (15)$$

$$\approx \left(\frac{2\pi}{\lambda^i}\right) \hat{\mathbf{k}}^j(\mathbf{d}^i) \cdot \boldsymbol{\delta}_n^j \quad (16)$$

Then, applying the narrowband approximation to (13), in which the complex envelope of the signal is approximately constant across the elements of the array [81, p. 34],

$$s_{d,n}^{ij}(t) \approx a_d^{ij} e^{j(\theta^j + \vartheta_n^{ij}(\mathbf{d}^i))} u^i(t - \tau_d^{ij}(t)) e^{-j\omega_c^i \tau_d^{ij}(t)} \quad (17)$$

Next, consider a first-order approximation for $R_0^{ij}(t)$ about $t = 0$,

$$R_0^{ij}(t) \approx R_0^{ij}(t)|_{t=0} + \dot{R}_0^{ij}(t)|_{t=0} t \triangleq R_0^{ij} + \dot{R}_0^{ij} t \quad (18)$$

Then, using $\tau_d^{ij}(t) = R_0^{ij}(t)/c$ in (17),

$$s_{d,n}^{ij}(t) = a_d^{ij} e^{j(\theta^j + \vartheta_n^{ij}(\mathbf{d}^i))} u^i(t - R_0^{ij}(t)/c) e^{-j\omega_c^i R_0^{ij}(t)/c} \quad (19)$$

$$\approx a_d^{ij} e^{j(\theta^j + \vartheta_n^{ij}(\mathbf{d}^i))} u^i\left((1 - \dot{R}_0^{ij}/c)t - R_0^{ij}/c\right) e^{-j\omega_c^i (R_0^{ij} + \dot{R}_0^{ij} t)/c} \quad (20)$$

$$= a_d^{ij} e^{j(\theta^j + \vartheta_n^{ij}(\mathbf{d}^i))} u^i(\alpha t - \tau_d^{ij}) e^{-j\omega_c^i \tau_d^{ij}} e^{j\omega_d^{ij} t} \quad (21)$$

where $\tau_d^{ij} = R_0^{ij}/c$, $\alpha = 1 - \dot{R}_0^{ij}/c$ is a time scaling factor, and ω_d^{ij} is the Doppler

frequency defined as

$$\omega_d^{ij} \triangleq - \left(\frac{\omega_c^i}{c} \right) \dot{R}_0^{ij} \quad (22)$$

$$= - \left(\frac{2\pi}{\lambda^i} \right) \frac{(\mathbf{r}^j - \mathbf{d}^i) \cdot (\dot{\mathbf{r}}^j - \dot{\mathbf{d}}^i)}{\|\mathbf{r}^j - \mathbf{d}^i\|} \Big|_{t=0} \quad (23)$$

Note that $\alpha = 1 - \dot{R}_0^{ij}/c \approx 1$ for the range of expected \dot{R}_0^{ij} . Consequently, it is ignored in the following.

To summarize, the complex baseband direct-path signal received by the n th array element of the j th receiver originated by the i th transmitter is given by

$$s_{d,n}^{ij}(t) = \underbrace{a_d^{ij}}_{(a)} \underbrace{e^{j\theta^j}}_{(b)} \underbrace{e^{j\theta_n^{ij}(\mathbf{d}^i)}}_{(c)} \underbrace{e^{-j\omega_c^i \tau_d^{ij}}}_{(d)} \underbrace{u^i(t - \tau_d^{ij})}_{(e)} \underbrace{e^{j\omega_d^{ij} t}}_{(f)} \quad (24)$$

Equation (24) is comprised of six factors: (a) an amplitude scaling factor, (b) an unknown oscillator phase factor, (c) a differential carrier phase factor, (d) a reference carrier phase factor, (e) the time delayed complex baseband transmitted signal, and (f) a Doppler modulation factor. To simplify notation, (24) may be expressed as

$$s_{d,n}^{ij}(t) = \gamma_d^{ij} e^{j\theta_n^{ij}(\mathbf{d}^i)} u^i(t - \tau_d^{ij}) e^{j\omega_d^{ij} t} \quad (25)$$

where γ_d^{ij} is ij th direct-path channel coefficient, defined using (5) and (25) as

$$\gamma_d^{ij} \triangleq a_d^{ij} e^{j(\theta^j - \omega_c^i \tau_d^{ij})} \quad (26)$$

$$= e^{j(\theta^j - \omega_c^i \tau_d^{ij})} \sqrt{\frac{P_{\text{erp}}^i(\mathbf{r}^j) \lambda^{i2} G_e^j(\mathbf{d}^i)}{(4\pi)^2 (R_0^{ij})^2}} \quad (27)$$

2.2.2 Target-Path Signal.

Let $s_{t,n}^{ij}(t)$ denote the target-path component of (8),

$$s_{t,n}^{ij}(t) = \alpha^{ij} a_t^{ij} e^{j(\theta^j - \omega_c^i \tau_{t,n}^{ij}(t))} u^i(t - \tau_{t,n}^{ij}(t)) \quad (28)$$

Following a similar procedure to that used for the direct-path signal in Sec. 2.2.1, $s_{t,n}^{ij}(t)$ can be approximated as

$$s_{t,n}^{ij}(t) \approx \underbrace{\alpha^{ij} a_t^{ij}}_{(a)} \underbrace{e^{j\theta^j}}_{(b)} \underbrace{e^{j\vartheta_n^{ij}(\mathbf{t})}}_{(c)} \underbrace{e^{-j\omega_c^i \tau_t^{ij}}}_{(d)} \underbrace{u^i(t - \tau_t^{ij})}_{(e)} \underbrace{e^{j\omega_t^{ij} t}}_{(f)} \quad (29)$$

where τ_t^{ij} is the bistatic delay with respect to the i th transmitter, target, and j th receiver,

$$\tau_t^{ij} \triangleq \left(\frac{1}{c} \right) (R_1^i + R_2^j) \quad (30)$$

$$= \left(\frac{1}{c} \right) (\|\mathbf{t} - \mathbf{d}^i\| + \|\mathbf{r}^j - \mathbf{t}\|) \Big|_{t=0} \quad (31)$$

$\vartheta_n^{ij}(\mathbf{t})$ is the differential carrier phase of the n th element with respect to the reference element, defined as

$$\vartheta_n^{ij}(\mathbf{t}) \triangleq -\omega_c^i \Delta \tau_n^{ij}(\mathbf{t}) \quad (32)$$

$$= \mathbf{k}^{ij}(\mathbf{t}) \cdot \boldsymbol{\delta}_n^j \quad (33)$$

and ω_t^{ij} is the target-path bistatic Doppler shift,

$$\omega_t^{ij} \triangleq - \left(\frac{\omega_c^i}{c} \right) (\dot{R}_1^{ij} + \dot{R}_2^{ij}) \quad (34)$$

$$= - \left(\frac{2\pi}{\lambda^i} \right) \left[\frac{(\mathbf{t} - \mathbf{d}^i) \cdot (\dot{\mathbf{t}} - \dot{\mathbf{d}}^i)}{\|\mathbf{t} - \mathbf{d}^i\|} + \frac{(\mathbf{r}^j - \mathbf{t}) \cdot (\dot{\mathbf{r}}^j - \dot{\mathbf{t}})}{\|\mathbf{r}^j - \mathbf{t}\|} \right] \Big|_{t=0} \quad (35)$$

Similar to the direct-path signal in (25), (29) is comprised of six factors: (a) an amplitude scaling factor, (b) an unknown oscillator phase factor, (c) a differential carrier phase factor, (d) a reference carrier phase factor, (e) the time delayed complex base-band transmitted signal, and (f) a Doppler modulation factor. To simplify notation, (29) may be expressed as

$$s_{t,n}^{ij}(t) = \gamma_t^{ij} e^{j\theta_n^{ij}(\mathbf{t})} u^i(t - \tau_t^{ij}) e^{j\omega_t^{ij}t} \quad (36)$$

where γ_t^{ij} is the ij th target-path channel coefficient, defined using (6) and (36) as

$$\gamma_t^{ij} \triangleq \alpha^{ij} a_t^{ij} e^{j(\theta^j - \omega_c^i \tau_t^{ij})} \quad (37)$$

$$= \alpha^{ij} e^{j(\theta^j - \omega_c^i \tau_t^{ij})} \sqrt{\frac{P_{\text{erp}}^i(\mathbf{t}) \lambda^{i2} G_e^j(\mathbf{t})}{(4\pi)^3 (R_1^i R_2^j)^2}} \quad (38)$$

2.3 Discretization

The i th baseband signal at the n th element of the j th receiver is given by

$$s_n^{ij}(t) = s_{d,n}^{ij}(t) + s_{t,n}^{ij}(t) + n_n^{ij}(t) \quad (39)$$

Let (39) be sampled at rate $f_s^i = 1/T_s^i = B^i$ Hz such that $s_n^{ij}[l] = s_n^{ij}(lT_s^i)$, resulting in the discrete time representation

$$s_n^{ij}[l] = s_{d,n}^{ij}[l] + s_{t,n}^{ij}[l] + n_n^{ij}[l], \quad l = 0, \dots, L^i - 1 \quad (40)$$

where $L^i = \lfloor T f_s^i \rfloor$ is the total number of samples, and the direct-path and target-path signals are given using (25) and (36) by

$$s_{d,n}^{ij}[l] = \gamma_d^{ij} e^{j\vartheta_n^{ij}(\mathbf{d}^i)} u^i[l - \ell_d^{ij}] e^{j\nu_d^{ij}l} \quad (41)$$

$$s_{t,n}^{ij}[l] = \gamma_t^{ij} e^{j\vartheta_n^{ij}(\mathbf{t})} u^i[l - \ell_t^{ij}] e^{j\nu_t^{ij}l} \quad (42)$$

where $\nu_d^{ij} = \omega_d^{ij}/f_s^i$ and $\nu_t^{ij} = \omega_t^{ij}/f_s^i$ are normalized Doppler frequencies measured in radians per sample, and $\ell_d^{ij} = \tau_d^{ij}f_s^i$ and $\ell_t^{ij} = \tau_t^{ij}f_s^i$ are normalized delays measured in samples. The noise sequence $n_n^{ij}[l] \sim \mathcal{CN}(0, \sigma^2)$, where $\sigma^2 = N_0 B^i$ is the average noise power, $E \{n_n^{ij}[l](n_n^{i'j'}[k])^*\} = \sigma^2 \delta_{i-i'} \delta_{j-j'} \delta_{l-k}$, and δ_n is the Kronecker delta.

Let $\mathbf{u}^i \in \mathbb{C}^{L^i \times 1}$ denote the sampled transmit waveform vector such that the l^{th} element is defined $[\mathbf{u}^i]_l = u^i[l] = u^i(lT_s^i)$ for $l = 0, \dots, L^i - 1$. It can be shown using (3) that $\|\mathbf{u}^i\|^2 = L^i$. Specifically,

$$\|\mathbf{u}^i\|^2 = \sum_{l=0}^{L^i-1} |u^i(lT_s^i)|^2 \approx \frac{1}{T_s^i} \int_0^T |u^i(t)|^2 dt = f_s^i T = L^i \quad (43)$$

Let \mathbf{s}_n^{ij} , $\mathbf{s}_{d,n}^{ij}$, and $\mathbf{s}_{t,n}^{ij}$ be defined similarly, i.e., $[\mathbf{s}_n^{ij}]_l = s_n^{ij}[l]$, $[\mathbf{s}_{d,n}^{ij}]_l = s_{d,n}^{ij}[l]$, and $[\mathbf{s}_{t,n}^{ij}]_l = s_{t,n}^{ij}[l]$ for $l = 0, \dots, L^i - 1$. Furthermore, define $\mathbf{D}_L(x) \in \mathbb{C}^{L \times L}$ by

$$\mathbf{D}_L(x) = \text{diag}([e^{j(0)x}, e^{j(1)x}, \dots, e^{j(L-1)x}]) \quad (44)$$

where $\text{diag}(\mathbf{x})$ for $\mathbf{x} \in \mathbb{C}^L$ is the $L \times L$ square matrix with diagonal elements \mathbf{x} such that the $(n, n)^{th}$ element $[\text{diag}(\mathbf{x})]_{n,n} = [\mathbf{x}]_n$. Finally, let $\mathbf{W}_L \in \mathbb{C}^{L \times L}$ denote the unitary discrete Fourier transform (DFT) matrix such that the $(m, n)^{th}$ element is

$$[\mathbf{W}]_{m,n} = \frac{1}{\sqrt{L}} e^{-j(\frac{2\pi}{L})mn} \quad (45)$$

for $m = 0, \dots, L - 1$ and $n = 0, \dots, L - 1$.

Then, the direct-path signal (41) can be represented in vector form by

$$\mathbf{s}_{d,n}^{ij} = \gamma_d^{ij} e^{j\vartheta_n^{ij}(\mathbf{d}^i)} \mathbf{D}_{L^i}(\nu_d^{ij}) (\mathbf{W}_{L^i}^H \mathbf{D}_{L^i}(-2\pi\ell_d^{ij}/L^i) \mathbf{W}_{L^i}) \mathbf{u}^i \quad (46)$$

To simplify (46), define the delay-Doppler operator $\mathcal{D}(\ell, \nu) \in \mathbb{C}^{L^i \times L^i}$ as

$$\mathcal{D}(\ell, \nu) = \mathbf{D}_{L^i}(\nu) \mathbf{W}_{L^i}^H \mathbf{D}_{L^i}(-2\pi\ell/L^i) \mathbf{W}_{L^i} \quad (47)$$

which is the matrix representation of the delay by ℓ and Doppler shift by ν operators applied to a length- L^i time domain sampled signal. Note that (47) applies a *circular* delay of ℓ samples. In many cases the wrapping of the tail end of the signal is insignificant because the delay is only a small fraction of the total signal duration, i.e., $\ell \ll L$. Alternatively, such wrapping may be avoided by zero-padding the received signals to account for the longest expected delay. Note also that $\mathcal{D}(\ell_1, \nu_1) \mathcal{D}(\ell_2, \nu_2) = \mathcal{D}(\ell_1 + \ell_2, \nu_1 + \nu_2)$, and $\mathcal{D}^H(\ell, \nu) = \mathcal{D}(-\ell, -\nu)$. Consequently, the delay-Doppler operator is unitary, i.e., $\mathcal{D}^{-1}(\ell, \nu) = \mathcal{D}^H(\ell, \nu)$ such that $\mathcal{D}^H(\ell, \nu) \mathcal{D}(\ell, \nu) = \mathbf{I}_{L^i}$, where \mathbf{I}_L is the $L \times L$ identity matrix. Using (47) in (46), the direct-path signal becomes

$$\mathbf{s}_{d,n}^{ij} = \gamma_d^{ij} e^{j\vartheta_n^{ij}(\mathbf{d}^i)} \mathcal{D}(\ell_d^{ij}, \nu_d^{ij}) \mathbf{u}^i \quad (48)$$

Similarly, the target signal (42) can be represented in vector form as

$$\mathbf{s}_{t,n}^{ij} = \gamma_t^{ij} e^{j\vartheta_n^{ij}(\mathbf{t})} \mathcal{D}(\ell_t^{ij}, \nu_t^{ij}) \mathbf{u}^i \quad (49)$$

Therefore, the i th baseband signal at the n th element of the j th receiver array in

(40) can be written in vector form using (48) and (49) as

$$\mathbf{s}_n^{ij} = \gamma_d^{ij} e^{j\vartheta_n^{ij}(\mathbf{d}^i)} \mathcal{D}(\ell_d^{ij}, \nu_d^{ij}) \mathbf{u}^i + \gamma_t^{ij} e^{j\vartheta_n^{ij}(\mathbf{t})} \mathcal{D}(\ell_t^{ij}, \nu_t^{ij}) \mathbf{u}^i + \mathbf{n}_n^{ij} \quad (50)$$

where $\mathbf{n}_n^{ij} \sim \mathcal{CN}(\mathbf{0}_{L^i}, \sigma^2 \mathbf{I}_{L^i})$ and $\mathbf{0}_{L^i}$ is the zero vector of length L^i .

2.4 Summary

This chapter has presented a detailed derivation of the PMR signal model that underlies the remainder of this dissertation. In particular, Eq. (50), which represents the discretized complex baseband signal at the n th array element of the j th receiver associated with the i th transmitter channel, is the starting point for the mathematical developments in Chapters III and IV. It also underlies signal models for AMR and PSL sensor networks that are presented in Chapter V as part of the unified detection framework. The form of Eq. (50) foreshadows several of the challenges associated with passive radar detection. As discussed in Sec. 1.1, the simultaneous presence of the direct-path and target-path signals in (50) complicates detection due to the large power ratio between the direct-path and target-path signals, $|\gamma_d^{ij}|^2/|\gamma_t^{ij}|^2 \gg 1$, that is typical in passive radar scenarios. In addition, the presence of receiver noise \mathbf{n}_n^{ij} guarantees that the direct-path signal will not be able to be isolated without distortion. Finally, the delays and Doppler shifts of the target-path and direct-path signals, encoded by the delay-Doppler operators $\mathcal{D}(\ell_d^{ij}, \nu_d^{ij})$ and $\mathcal{D}(\ell_t^{ij}, \nu_t^{ij})$ require careful consideration. These challenges are addressed in Chapters III and IV.

III. Passive MIMO Radar Detection without References

This chapter¹ addresses the problem of target detection in PMR networks when direct-path signals are unavailable, shown in Fig. 9. As discussed in Sec. 1.1.2, direct-path signals are typically the dominant signals (and interferers) in passive radar applications [30]. However, it is possible they might not be present if there is physical blockage of the line-of-sight paths between transmitters and receivers, or if illuminators were to utilize highly directive transmission and/or null the receiver directions. In such cases, the absence of direct-path signals would preclude the conventional approach to detection described in Sec. 1.4.1, and would necessitate a fundamentally different type of processing. This has given rise to recent theoretical interest in target detection in PMR networks when direct-path signals are unavailable [10, 84].

Wang and Yazici present a centralized detector for this problem that is constrained to be linear in the measurements [84]. Their formulation assumes that targets scatter isotropically, which is unlikely to hold for complex targets in multistatic geometries [88]. Their formulation also assumes phase-synchronized (coherent) receivers, which is a stringent requirement in distributed applications. Bialkowski *et al.* derive a

¹The material in this chapter appears in [38].

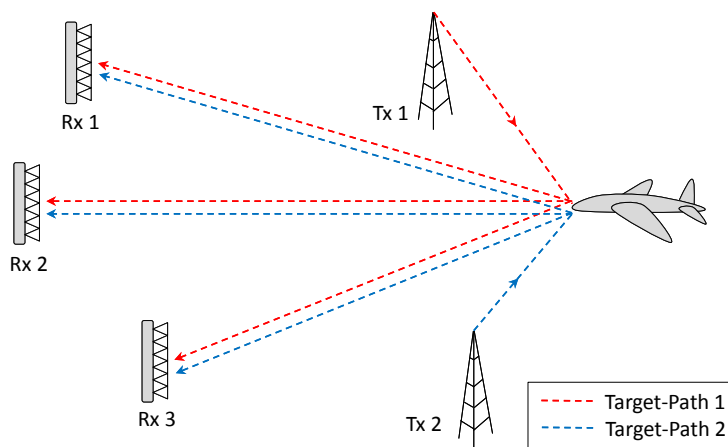


Figure 9. Passive MIMO Radar without Direct-Path Signals

generalized likelihood ratio test (GLRT) without constraining the detector to be linear in the measurements [10]. The resulting non-linear detector implicitly accounts for non-isotropic target reflectivity and non-coherent receivers. However, neither [84] nor [10] address the probability distributions of their detection statistics.

In this chapter, the results of [10] are extended in several ways. First, the formulation of [10] is extended from one transmitter to multiple transmitters, and from single-channel receivers to multichannel (array) receivers. The GLRT is then derived. These extensions significantly enhance probability of detection and reduce detection ambiguity. Second, using recent results from random matrix theory, the exact distribution of the test statistic is identified under both hypotheses. To the author’s knowledge, this is the first appearance of these distributions in the context of radar detection. These distributions show that detection sensitivity is only a function of the number of transmitters, the number of receivers, the number of signal samples, and the average input SNR. Numerical examples demonstrate important properties of the detector, namely, that (a) receivers and transmitters contribute asymmetrically to detection sensitivity, which is uncommon in radar applications, and (b) integration gain grows non-coherently with increasing signal length. Third, an equivalence is demonstrated between PMR detection without direct-path signals and detection in PSL networks. This generalizes PSL to the scenario in which multiple transmitters are co-located on the “source” platform, and establishes equivalence between detection ambiguity and “source” localization. Finally, the ambiguity performance of the proposed detector is investigated, and it is shown that salient features of the detector ambiguity function can be explained in terms of the time-difference of arrival (TDOA), frequency-difference of arrival (FDOA), and angle-of-arrival (AOA) of the target signals.

3.1 Signal Model

Consider a PMR network like the one shown in Fig. 9. Let there be N_t transmitters and N_r receivers. Fig. 10 depicts the geometry and signal environment of the ij th bistatic pair, consisting of the i th transmitter and j th receiver. The position and velocity of the i th transmitter are denoted by \mathbf{d}^i and $\dot{\mathbf{d}}^i$, and the position and velocity of the j th receiver by \mathbf{r}^j and $\dot{\mathbf{r}}^j$. The spatial states of all transmitters and receivers are assumed known. Assume the transmitted signals are narrowband and separable in frequency, and that each receiver is equipped with an N_e -element array. The incident signal at the n th element of the j th receiver is channelized in frequency, demodulated to baseband and sampled in time. Let $\mathbf{s}_n^{ij} \in \mathbb{C}^{L^i \times 1}$ denote the length- L^i sampled complex baseband signal on the i th frequency channel of the n th element of the j th receiver array. For simplicity, it is assumed that $L^i = L \forall i$, i.e., all received signals have the same length L . An expression for \mathbf{s}_n^{ij} is given by Eq. (50) in Chapter II. Assuming a target at position \mathbf{t} and velocity $\dot{\mathbf{t}}$, and ignoring the direct-path signal in (50), \mathbf{s}_n^{ij} is given by

$$\mathbf{s}_n^{ij} = \gamma_t^{ij} e^{j\vartheta_n^{ij}(\mathbf{t})} \mathcal{D}(\ell_t^{ij}, \nu_t^{ij}) \mathbf{u}^i + \mathbf{n}_n^{ij} \quad (51)$$

where $\mathbf{u}^i \in \mathbb{C}^{L \times 1}$ is the complex baseband signal emitted by the i th transmitter; $\mathcal{D}(\ell_t^{ij}, \nu_t^{ij}) \in \mathbb{C}^{L \times L}$ is the unitary linear operator that accounts for the delay and Doppler shift imparted to the i th transmit signal as it propagates to the j th receiver along the target-path channel, defined by Eq. (47) in Sec. 2.3; ℓ_t^{ij} is the target-path propagation delay in samples; ν_t^{ij} is the target-path Doppler shift in radians per sample; $\vartheta_n^{ij}(\mathbf{t})$ is the differential phase at the n th array element with respect to a reference element due to plane wave propagation from the target direction, defined by Eq. (33) in Sec. 2.2.2; γ_t^{ij} is a complex channel coefficient that accounts for the composite

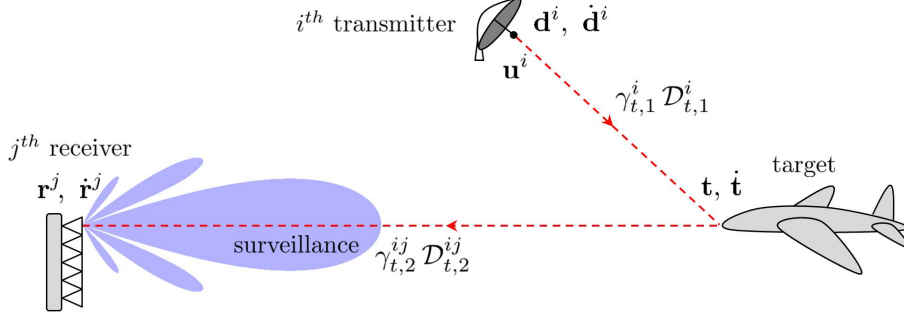


Figure 10. The ij th Bistatic Pair in a PMR Network without Direct-Path Signals

scaling of \mathbf{u}^i associated with the ij th target-path channel, defined by Eq. (38) in Sec. 2.2.2; $\mathbf{n}_n^{ij} \in \mathbb{C}^{L \times 1}$ is circular Gaussian noise distributed as $\mathcal{CN}(\mathbf{0}_L, \sigma^2 \mathbf{I}_L)$ with known variance σ^2 ; and $j = \sqrt{-1}$. Here, $\mathbf{0}_L$ denotes the length- L zero vector, and \mathbf{I}_L is the $L \times L$ identity matrix. Noise is assumed to be independent across transmit bands, receivers, and array elements, i.e., $\mathbb{E}\{\mathbf{n}_n^{ij}(\mathbf{n}_m^{kl})^H\} = \sigma^2 \delta_{n-m} \delta_{i-k} \delta_{j-l} \mathbf{I}_L$, where $(\cdot)^H$ is the Hermitian transpose and δ_x is the Kronecker delta. The transmit signal \mathbf{u}^i is defined such that $\|\mathbf{u}^i\|^2 = L$. Additional detail on the terms in (51) is provided in Chapter II. To simplify notation, \mathcal{D}_t^{ij} is used in place of $\mathcal{D}(\ell_t^{ij}, \nu_t^{ij})$ in the following.

Fig. 10 shows that the channel coefficient γ_t^{ij} may be expressed as the product of two coefficients that correspond to the two legs of the bistatic target-path channel, $\gamma_t^{ij} = \gamma_{t,1}^i \gamma_{t,2}^{ij}$, where $\gamma_{t,1}^i$ and $\gamma_{t,2}^{ij}$ are defined using (38) as

$$\gamma_{t,1}^i(\mathbf{t}) = e^{-j\omega_c^i R_1^i(\mathbf{t})/c} \sqrt{\frac{P_{\text{erp}}^i(\mathbf{t})}{4\pi(R_1^i(\mathbf{t}))^2}} \quad (52)$$

$$\gamma_{t,2}^{ij}(\mathbf{t}) = \alpha^{ij} e^{j(\theta^i - \omega_c^i R_2^j(\mathbf{t})/c)} \sqrt{\frac{\lambda^2 G_e^j(\mathbf{t})}{(4\pi R_2^j(\mathbf{t}))^2}} \quad (53)$$

$\omega_c^i = 2\pi f_c^i$, f_c^i is the i th transmitter's carrier frequency in Hertz, $R_1^i(\mathbf{t}) = \|\mathbf{t} - \mathbf{d}^i\|$, $R_2^j(\mathbf{t}) = \|\mathbf{r}^j - \mathbf{t}\|$, c is the speed of light, $P_{\text{erp}}^i(\mathbf{t})$ is the i th transmitter's effective radiated power in the direction of \mathbf{t} , α^{ij} is the target's bistatic reflectivity as observed by the ij th Tx-Rx channel, θ^j is a random phase associated with the j th receiver,

$\lambda^i = c/f_c^i$ is the wavelength of the i th transmitter, and $G_e^j(\mathbf{t})$ is the array element pattern in the direction of \mathbf{t} . Similarly, the delay-Doppler operator \mathcal{D}_t^{ij} may be expressed as the composition of two unitary linear operators that correspond to the two legs of the bistatic target-path channel, i.e., $\mathcal{D}_t^{ij} = \mathcal{D}_{t,2}^{ij} \mathcal{D}_{t,1}^i$, where $\mathcal{D}_{t,1}^i$ and $\mathcal{D}_{t,2}^{ij}$ characterize the delay and Doppler shift of the first and second legs of the target-path channel, respectively.

Let $\mathbf{a}^{ij}(\mathbf{x}) \in \mathbb{C}^{N_e \times 1}$ denote the spatial steering vector in the direction of \mathbf{x} ,

$$\mathbf{a}^{ij}(\mathbf{x}) = \begin{bmatrix} e^{j\vartheta_1^{ij}(\mathbf{x})} & e^{j\vartheta_2^{ij}(\mathbf{x})} & \dots & e^{j\vartheta_{N_e}^{ij}(\mathbf{x})} \end{bmatrix}^T \quad (54)$$

The concatenation of the time series vectors from all N_e elements of the j th receiver in the i th frequency band, $\mathbf{s}^{ij} = [(\mathbf{s}_1^{ij})^T \dots (\mathbf{s}_{N_e}^{ij})^T]^T \in \mathbb{C}^{N_e L \times 1}$, can be written as

$$\mathbf{s}^{ij} = \mathbf{M}_t^{ij} \mathbf{u}^i + \mathbf{n}^{ij} \quad (55)$$

where $\mathbf{n}^{ij} = [(\mathbf{n}_1^{ij})^T \dots (\mathbf{n}_{N_e}^{ij})^T]^T \in \mathbb{C}^{N_e L \times 1}$, and the matrix $\mathbf{M}_t^{ij} \in \mathbb{C}^{N_e L \times L}$ is defined

$$\mathbf{M}_t^{ij} = \gamma_t^{ij} (\mathbf{a}_t^{ij} \otimes \mathcal{D}_t^{ij}) \quad (56)$$

where $\mathbf{a}_t^{ij} = \mathbf{a}^{ij}(\mathbf{t})$ for brevity, and \otimes is the Kronecker product.

3.2 Surveillance-Surveillance GLRT

Consider testing for the presence of a target within a position-velocity cell $(\mathbf{p}, \dot{\mathbf{p}})$, termed the ‘*cell under test*,’ where \mathbf{p} and $\dot{\mathbf{p}}$ are the hypothesized emitter position and velocity, respectively. This detection problem may be formulated as a binary

hypothesis test between alternative (\mathcal{H}_1) and null (\mathcal{H}_0) hypotheses:

$$\begin{aligned}\mathcal{H}_1 : \quad \mathbf{s}^{ij} &= \mathbf{M}_p^{ij} \mathbf{u}^i + \mathbf{n}^{ij} \\ \mathcal{H}_0 : \quad \mathbf{s}^{ij} &= \mathbf{n}^{ij}\end{aligned}\tag{57}$$

for $i = 1 \dots N_t$ and $j = 1 \dots N_r$. In (57), the matrix $\mathbf{M}_p^{ij} \in \mathbb{C}^{N_e L \times L}$ is defined

$$\mathbf{M}_p^{ij} = \gamma_p^{ij} (\mathbf{a}_p^{ij} \otimes \mathcal{D}_p^{ij})\tag{58}$$

where γ_p^{ij} is the target-path channel coefficient associated with the hypothesized position \mathbf{p} , $\mathbf{a}_p^{ij} = \mathbf{a}^{ij}(\mathbf{p})$ for brevity, $\mathcal{D}_p^{ij} = \mathcal{D}(\ell_p^{ij}, \nu_p^{ij})$, ℓ_p^{ij} is the bistatic delay associated with the hypothesized position \mathbf{p} in samples, and ν_p^{ij} is the bistatic Doppler shift associated with the cell under test $(\mathbf{p}, \dot{\mathbf{p}})$ in radians per sample. Let \mathbf{s}^i denote the concatenation of all receiver measurements associated with the i th transmitter, and let \mathbf{s} denote the concatenation of all \mathbf{s}^i across transmitters,

$$\mathbf{s}^i = [(\mathbf{s}^{i1})^T, \dots, (\mathbf{s}^{iN_r})^T]^T \in \mathbb{C}^{N_r L \times 1}\tag{59}$$

$$\mathbf{s} = [(\mathbf{s}^1)^T, \dots, (\mathbf{s}^{N_t})^T]^T \in \mathbb{C}^{N_t N_r L \times 1}\tag{60}$$

Similarly, let $\boldsymbol{\gamma}_p^i$ denote the vector of coefficients associated with the i th transmitter, and let $\boldsymbol{\gamma}_p$ denote the concatenation of all $\boldsymbol{\gamma}_p^i$ across transmitters,

$$\boldsymbol{\gamma}_p^i = [\gamma_p^{i1} \dots \gamma_p^{iN_r}]^T \in \mathbb{C}^{N_r \times 1}\tag{61}$$

$$\boldsymbol{\gamma}_p = [(\boldsymbol{\gamma}_p^1)^T \dots (\boldsymbol{\gamma}_p^{N_t})^T]^T \in \mathbb{C}^{N_t N_r \times 1}\tag{62}$$

Finally, let $\mathbf{u} = [(\mathbf{u}^1)^T \dots (\mathbf{u}^{N_t})^T]^T \in \mathbb{C}^{N_t L \times 1}$.

Due to the independence of the receiver noise across transmitter channels, the conditional probability density function (PDF) of \mathbf{s} under \mathcal{H}_1 , $p_1(\mathbf{s}|\boldsymbol{\gamma}_p, \mathbf{u})$, factors

according to

$$p_1(\mathbf{s} | \boldsymbol{\gamma}_p, \mathbf{u}) = \prod_{i=1}^{N_t} p_1^i(\mathbf{s}^i | \boldsymbol{\gamma}_p^i, \mathbf{u}^i) \quad (63)$$

where

$$p_1^i(\mathbf{s}^i | \boldsymbol{\gamma}_p^i, \mathbf{u}^i) = \frac{1}{(\pi\sigma^2)^{N_r L}} \exp \left\{ -\frac{1}{\sigma^2} \sum_{j=1}^{N_r} \|\mathbf{s}^{ij} - \mathbf{M}_p^{ij} \mathbf{u}^i\|^2 \right\} \quad (64)$$

Similarly, the PDF of \mathbf{s} under \mathcal{H}_0 , $p_0(\mathbf{s})$, is given by

$$p_0(\mathbf{s}) = \frac{1}{(\pi\sigma^2)^{N_t N_r L}} \exp \left\{ -\frac{1}{\sigma^2} \|\mathbf{s}\|^2 \right\} \quad (65)$$

In this formulation, the transmit signals \mathbf{u} and channel coefficients $\boldsymbol{\gamma}_p$ are considered deterministic and unknown. Thus, hypothesis \mathcal{H}_1 is composite because $p_1(\mathbf{s} | \boldsymbol{\gamma}_p, \mathbf{u})$ is parameterized by \mathbf{u} and $\boldsymbol{\gamma}_p$. Therefore, the GLRT is derived, which replaces each unknown parameter by its maximum likelihood estimate (MLE) in the likelihood ratio test [49]. This derivation follows the approach of Bialkowski *et al.* in [10], yet extends their formulation from one transmitter to multiple transmitters, and from single-channel receivers to multichannel array receivers.

Let $l_1(\boldsymbol{\gamma}_p, \mathbf{u} | \mathbf{s}) = \log p_1(\mathbf{s} | \boldsymbol{\gamma}_p, \mathbf{u})$ denote the log-likelihood function under \mathcal{H}_1 . Similarly, let $l_0(\mathbf{s}) = \log p_0(\mathbf{s})$. Then, the GLRT may be written as

$$\max_{\{\boldsymbol{\gamma}_p, \mathbf{u}\}} l_1(\boldsymbol{\gamma}_p, \mathbf{u} | \mathbf{s}) - l_0(\mathbf{s}) \underset{\mathcal{H}_0}{\overset{\mathcal{H}_1}{\gtrless}} \kappa \quad (66)$$

where κ is chosen to maintain a desired probability of false alarm. From (63), $l_1(\boldsymbol{\gamma}_p, \mathbf{u} | \mathbf{s})$ may be written as

$$l_1(\boldsymbol{\gamma}_p, \mathbf{u} | \mathbf{s}) = \sum_{i=1}^{N_t} l_1^i(\boldsymbol{\gamma}_p^i, \mathbf{u}^i | \mathbf{s}^i) \quad (67)$$

where, from (64) and ignoring an additive constant,

$$l_1^i(\boldsymbol{\gamma}_p^i, \mathbf{u}^i | \mathbf{s}^i) = -\frac{1}{\sigma^2} \sum_{j=1}^{N_r} \|\mathbf{s}^{ij} - \mathbf{M}_p^{ij} \mathbf{u}^i\|^2 \quad (68)$$

Substituting (68) into (56),

$$l_1^i(\boldsymbol{\gamma}_p^i, \mathbf{u}^i | \mathbf{s}^i) = -\frac{1}{\sigma^2} \sum_{j=1}^{N_r} \|\mathbf{s}^{ij} - \gamma^{ij}(\mathbf{a}_p^{ij} \otimes \mathcal{D}_p^{ij}) \mathbf{u}^i\|^2 \quad (69)$$

From (69), the MLE of γ_p^{ij} , $\hat{\gamma}_p^{ij}$, is given by

$$\hat{\gamma}_p^{ij} = \frac{((\mathbf{a}_p^{ij} \otimes \mathcal{D}_p^{ij}) \mathbf{u}^i)^H \mathbf{s}^{ij}}{\|(\mathbf{a}_p^{ij} \otimes \mathcal{D}_p^{ij}) \mathbf{u}^i\|^2} \quad (70)$$

This may be simplified to

$$\hat{\gamma}_p^{ij} = \frac{\mathbf{u}^{iH} \tilde{\mathbf{s}}_s^{ij}}{\sqrt{N_e} \|\mathbf{u}^i\|^2} \quad (71)$$

where

$$\tilde{\mathbf{s}}_s^{ij} = (\mathcal{D}_p^{ij})^H \mathbf{s}_s^{ij} \quad (72)$$

and

$$\mathbf{s}_s^{ij} = \frac{1}{\sqrt{N_e}} \sum_{n=1}^{N_e} [\mathbf{a}_p^{ij}]_n^* \mathbf{s}_n^{ij} \quad (73)$$

The notation $[\mathbf{x}]_n$ denotes the n^{th} element of \mathbf{x} . Note that \mathbf{s}_s^{ij} may be interpreted as a surveillance channel for the i th transmit channel that is formed at the j th receiver by beamforming in the direction of \mathbf{p} , and $\tilde{\mathbf{s}}_s^{ij}$ is this channel after removal of the delay and Doppler shift resulting from bistatic propagation with respect to the cell under test $(\mathbf{p}, \dot{\mathbf{p}})$. Substituting (71) for γ_p^{ij} in (69), and simplifying, gives

$$l_1^i(\hat{\boldsymbol{\gamma}}_p^i, \mathbf{u}^i | \mathbf{s}^i) = -\frac{1}{\sigma^2} \left(\|\mathbf{s}^i\|^2 - \frac{\mathbf{u}^{iH} \Phi_s^i \Phi_s^{iH} \mathbf{u}^i}{\|\mathbf{u}^i\|^2} \right) \quad (74)$$

where $\Phi_s^i = [\tilde{\mathbf{s}}_s^{i1}, \dots, \tilde{\mathbf{s}}_s^{iN_r}] \in \mathbb{C}^{L \times N_r}$. Let $\lambda_1(\cdot)$ denote the largest eigenvalue of its matrix argument, and let $\mathbf{v}_1(\cdot)$ denote the associated eigenvector. Then, the Rayleigh quotient in (74) achieves its maximum value, $\lambda_1(\Phi_s^i \Phi_s^{iH})$, when $\mathbf{u} = \mathbf{v}_1(\Phi_s^i \Phi_s^{iH})$ [44, p. 176]. Therefore $\hat{\mathbf{u}}^i = \mathbf{v}_1(\Phi_s^i \Phi_s^{iH})$, and

$$l_1^i(\hat{\gamma}_p^i, \hat{\mathbf{u}}^i | \mathbf{s}^i) = -\frac{1}{\sigma^2} \left(\|\mathbf{s}^i\|^2 - \lambda_1(\Phi_s^i \Phi_s^{iH}) \right) \quad (75)$$

Noting that $\lambda_1(\Phi_s^i \Phi_s^{iH}) = \lambda_1(\Phi_s^{iH} \Phi_s^i)$, and that typically $N_r \ll L$, it is more computationally efficient to consider the *Gram matrix* $\mathbf{G}_{ss}^i = (\Phi_s^i)^H \Phi_s^i \in \mathbb{C}^{N_r \times N_r}$, giving

$$l_1^i(\hat{\gamma}_p^i, \hat{\mathbf{u}}^i | \mathbf{s}^i) = -\frac{1}{\sigma^2} \left(\|\mathbf{s}^i\|^2 - \lambda_1(\mathbf{G}_{ss}^i) \right) \quad (76)$$

Therefore, using (67) and (76),

$$l_1(\hat{\gamma}_p, \hat{\mathbf{u}} | \mathbf{s}) = -\frac{1}{\sigma^2} \|\mathbf{s}\|^2 + \left(\frac{1}{\sigma^2} \right) \sum_{i=1}^{N_t} \lambda_1(\mathbf{G}_{ss}^i) \quad (77)$$

It can similarly be shown under \mathcal{H}_0 that

$$l_0(\mathbf{s}) = -\frac{1}{\sigma^2} \|\mathbf{s}\|^2 \quad (78)$$

Using (77) and (78) in (66), the resulting GLRT is given by

$$\xi_{ss} = \frac{1}{\sigma^2} \sum_{i=1}^{N_t} \lambda_1(\mathbf{G}_{ss}^i) \underset{\mathcal{H}_0}{\overset{\mathcal{H}_1}{\gtrless}} \kappa \quad (79)$$

The statistic ξ_{ss} in Eq. (79) is termed the *surveillance-surveillance* GLRT (SS-GLRT) because the elements of the matrices $\{\mathbf{G}_{ss}^i : i = 1 \dots N_t\}$ consist of the pairwise inner products of delay-Doppler compensated surveillance signals.

3.3 Distribution

In this section, PDFs are presented for the test statistic ξ_{ss} in (79) under \mathcal{H}_1 and \mathcal{H}_0 . This development considers the presence or absence of a target within the cell under test $(\mathbf{p}, \dot{\mathbf{p}})$, where \mathbf{p} and $\dot{\mathbf{p}}$ are the hypothesized target position and velocity, respectively. Under this condition, the surveillance signal $\tilde{\mathbf{s}}_s^{ij}$ in (72) reduces to

$$\tilde{\mathbf{s}}_s^{ij} = b_1 \mu_s^{ij} \mathbf{u}^i + \tilde{\mathbf{n}}_s^{ij} \quad (80)$$

where $\mu_s^{ij} = \gamma_p^{ij} \sqrt{N_e}$, $b_1 = 1$ under \mathcal{H}_1 and $b_1 = 0$ under \mathcal{H}_0 , and $\tilde{\mathbf{n}}_s^{ij}$ is distributed as $\mathcal{CN}(\mathbf{0}_L, \sigma^2 \mathbf{I}_L)$. Note that μ_s^{ij} is the channel coefficient γ^{ij} scaled by a beamforming gain of $\sqrt{N_e}$. Then, $\tilde{\mathbf{s}}_s^{ij}$ is distributed as

$$\tilde{\mathbf{s}}_s^{ij} \sim \mathcal{CN}(b_1 \mu_s^{ij} \mathbf{u}^i, \sigma^2 \mathbf{I}_L) \quad (81)$$

To begin, note that $\xi_{ss} = \sum_{i=1}^{N_t} \xi_{ss}^i$, where

$$\xi_{ss}^i = \lambda_1 \left(\frac{1}{\sigma^2} \mathbf{G}_{ss}^i \right) \quad (82)$$

Because the receiver noise is independent across transmit channels, the PDF of ξ_{ss} , denoted $p_{\xi_{ss}}(\xi)$, is

$$p_{\xi_{ss}}(\xi) = [p_{\xi_{ss}}^1 * p_{\xi_{ss}}^2 * \cdots * p_{\xi_{ss}}^{N_t}] (\xi) \quad (83)$$

where $*$ denotes convolution, and $p_{\xi_{ss}}^i(\xi)$ is the PDF of ξ_{ss}^i . The problem is then finding $p_{\xi_{ss}}^i(\xi)$ under both hypotheses.

3.3.1 Alternative Hypothesis.

Using (80), the Gram matrix \mathbf{G}_{ss}^i under the alternative hypothesis, \mathcal{H}_1 , becomes

$$\mathbf{G}_{ss}^i = \begin{bmatrix} (\mu_s^{i1} \mathbf{u}^i + \tilde{\mathbf{n}}_s^{i1})^H \\ \vdots \\ (\mu_s^{iN_r} \mathbf{u}^i + \tilde{\mathbf{n}}_s^{iN_r})^H \end{bmatrix} [\mu_s^{i1} \mathbf{u}^i + \tilde{\mathbf{n}}_s^{i1} \cdots \mu_s^{iN_r} \mathbf{u}^i + \tilde{\mathbf{n}}_s^{iN_r}] \quad (84)$$

$$= \underbrace{(\mathbf{u}^i (\boldsymbol{\mu}_s^i)^T + \tilde{\mathbf{N}}_s^i)^H}_{= (\Phi_s^i)^H} \underbrace{(\mathbf{u}^i (\boldsymbol{\mu}_s^i)^T + \tilde{\mathbf{N}}_s^i)}_{= \Phi_s^i} \quad (85)$$

where $\boldsymbol{\mu}_s^i = [\mu_s^{i1}, \dots, \mu_s^{iN_r}]^T$ and $\tilde{\mathbf{N}}_s^i = [\tilde{\mathbf{n}}_s^{i1}, \dots, \tilde{\mathbf{n}}_s^{iN_r}]$. Thus, the columns of $(\Phi_s^i)^H$ are independent N_r -variate complex Gaussian vectors, where the k th column is distributed as $\mathcal{CN}((\boldsymbol{\mu}_s^i)^* [\mathbf{u}^i]_k^*, \sigma^2 \mathbf{I}_{N_r})$. Consequently, \mathbf{G}_{ss}^i is a non-central uncorrelated complex Wishart matrix [47, 90], denoted $\mathbf{G}_{ss}^i \sim \mathbf{W}_{N_r}(L, \boldsymbol{\Sigma}^i, \boldsymbol{\Omega}^i)$, where $\boldsymbol{\Sigma}^i = \sigma^2 \mathbf{I}_{N_r}$ is the covariance matrix of the columns of $(\Phi_s^i)^H$, and

$$\boldsymbol{\Omega}^i \triangleq (\boldsymbol{\Sigma}^i)^{-1} \mathbb{E}\{(\Phi_s^i)^H\} \mathbb{E}\{\Phi_s^i\} = \left(\frac{L \|\boldsymbol{\mu}_s^i\|^2}{\sigma^2} \right) (\hat{\boldsymbol{\mu}}_s^i)^* (\hat{\boldsymbol{\mu}}_s^i)^T \quad (86)$$

is a rank-1 non-centrality matrix with non-zero eigenvalue ζ_{ss}^i given by

$$\zeta_{ss}^i = \frac{L \|\boldsymbol{\mu}_s^i\|^2}{\sigma^2} \quad (87)$$

and eigenvector $(\hat{\boldsymbol{\mu}}_s^i)^* = (\boldsymbol{\mu}_s^i)^* / \|\boldsymbol{\mu}_s^i\|$.

In general, the PDF of the largest eigenvalue ϕ of a matrix $\boldsymbol{\Sigma}^{-1} \mathbf{X}$, where $\mathbf{X} \sim \mathbf{W}_s(t, \boldsymbol{\Sigma}, \boldsymbol{\Omega})$ with rank-1 noncentrality matrix $\boldsymbol{\Omega}$, is given by [48] as

$$f_1(\phi; s, t, \zeta) = \frac{e^{-\zeta} |\boldsymbol{\Psi}(\phi)| \text{tr}(\boldsymbol{\Psi}^{-1}(\phi) \boldsymbol{\Phi}(\phi)) U(\phi)}{\Gamma(t-s+1) \prod_{k=1}^{s-1} \Gamma(t-k) \Gamma(s-k)} \quad (88)$$

where ζ is the largest eigenvalue of $\boldsymbol{\Omega}$, $\Gamma(\cdot)$ is the gamma function [3, Eq. (6.1.1)],

$\text{tr}(\cdot)$ denotes the trace, $|\cdot|$ denotes the determinant, $U(\cdot)$ is the unit step function, $\Phi(\phi)$ is the $s \times s$ matrix with entries

$$[\Phi(\phi)]_{m,n} = \begin{cases} \phi^{t-m} e^{-\phi} {}_0F_1(t-s+1; \zeta\phi) & n = 1 \\ \phi^{t+s-m-n} e^{-\phi} & n > 1 \end{cases} \quad (89)$$

${}_0F_1(\cdot; \cdot)$ denotes the generalized hypergeometric function ${}_pF_q(a_1 \cdots a_p; b_1 \cdots b_q; z)$ [29, Eq. (9.14.1)] with $p = 0$ and $q = 1$, $\Psi(\phi)$ is the $s \times s$ matrix with entries

$$[\Psi(\phi)]_{m,n} = \begin{cases} \int_0^\phi y^{t-m} e^{-y} {}_0F_1(t-s+1; \zeta y) dy & n = 1 \\ \gamma(t+s-m-n+1, \phi) & n > 1 \end{cases} \quad (90)$$

and $\gamma(\cdot, \cdot)$ is the incomplete gamma function [3, Eq. (6.5.2)]. Therefore, the PDF of ξ_{ss}^i under \mathcal{H}_1 is

$$p_{\xi_{ss}}^i(\xi; \mathcal{H}_1) = f_1(\xi; N_r, L, \zeta_{ss}^i) \quad (91)$$

3.3.2 Null Hypothesis.

Under the null hypothesis, \mathcal{H}_0 , \mathbf{G}_{ss}^i in (85) reduces to

$$\mathbf{G}_{ss}^i = (\tilde{\mathbf{N}}_s^i)^H \tilde{\mathbf{N}}_s^i \quad (92)$$

which is a central uncorrelated complex Wishart matrix, denoted $\mathbf{G}_{ss}^i \sim \mathbf{W}_{N_r}(L, \Sigma^i)$, with $\Sigma^i = \sigma^2 \mathbf{I}_{N_r}$. In general, the PDF of the largest eigenvalue ϕ of a matrix $\Sigma^{-1} \mathbf{X}$, where $\mathbf{X} \sim \mathbf{W}_s(t, \Sigma)$, is given by [48] as

$$f_0(\phi; s, t) = \frac{|\Psi_c(\phi)| \text{tr}(\Psi_c^{-1}(\phi) \Phi_c(\phi)) U(\phi)}{\prod_{k=1}^s \Gamma(t-k+1) \Gamma(s-k+1)} \quad (93)$$

where $\Psi_c(\phi)$ and $\Phi_c(\phi)$ are $s \times s$ matrices with elements

$$[\Psi_c(\phi)]_{m,n} = \gamma(t + s - m - n + 1, \phi) \quad (94)$$

$$[\Phi_c(\phi)]_{m,n} = \phi^{t+s-m-n} e^{-\phi} \quad (95)$$

Therefore, the PDF of ξ_{ss}^i under \mathcal{H}_0 is

$$p_{\xi_{ss}}^i(\xi; \mathcal{H}_0) = f_0(\xi; N_r, L) \quad (96)$$

3.3.3 Dependence on SNR.

The PDF $p_{\xi_{ss}}^i(\xi; \mathcal{H}_1)$ in (91) depends on the transmit signal \mathbf{u}^i and channel coefficients $\gamma^i = \boldsymbol{\mu}_s^i / \sqrt{N_e}$ through only the received signal length L and the non-centrality parameter ζ_{ss}^i in (87), which may alternatively be expressed as

$$\zeta_{ss}^i = L N_r \text{SNR}_{\text{avg}}^i, \quad (97)$$

where

$$\text{SNR}_{\text{avg}}^i = \|\boldsymbol{\mu}_s^i\|^2 / (N_r \sigma^2) \quad (98)$$

is the average input SNR associated with the i th transmitter after surveillance channel formation. Consequently, the PDF $p_{\xi_{ss}}(\xi; \mathcal{H}_1)$, which is the convolution of the individual $p_{\xi_{ss}}^i(\xi; \mathcal{H}_1)$ across transmitters, is a function of only N_t , N_r , L , and $\{\text{SNR}_{\text{avg}}^i\}$. Thus, detection performance does not depend on the specific structure of the transmit waveforms $\{\mathbf{u}^i\}$, but only their energies and lengths. In addition, it does not depend on the specific input SNRs at each receiver channel; rather, it depends on only the average SNR for each transmitter across receivers.

3.4 Interpretation

This section discusses the relationship between PMR and PSL sensor networks. PSL sensor networks are comprised of geographically separated receivers that detect and localize targets by intercepting and processing target-emitted signals. An example PSL sensor network is illustrated in Fig. 11. Comparison with Fig. 9 suggests that PMR sensor networks without direct-path signals may be interpreted as PSL sensor networks. In particular, the received signal \mathbf{s}_n^{ij} in (51) may be expressed in terms of the channel coefficients and delay-Doppler operators of each leg of the target-path channel, shown in Fig. 10, as

$$\mathbf{s}_n^{ij} = \gamma_{t,1}^i \gamma_{t,2}^{ij} e^{j\theta_n^{ij}(\mathbf{t})} \mathcal{D}_{t,2}^{ij} \mathcal{D}_{t,1}^i \mathbf{u}^i + \mathbf{n}_n^{ij} \quad (99)$$

and then simplified to

$$\mathbf{s}_n^{ij} = \gamma_{t,2}^{ij} e^{j\theta_n^{ij}(\mathbf{t})} \mathcal{D}_{t,2}^{ij} \tilde{\mathbf{u}}^i + \mathbf{n}_n^{ij} \quad (100)$$

where $\tilde{\mathbf{u}}^i = \gamma_{t,1}^i \mathcal{D}_{t,1}^i \mathbf{u}^i$. Eq. (100) states that the received signal \mathbf{s}_n^{ij} in a PMR scenario is equivalent to the signal that would have been received if the signal $\tilde{\mathbf{u}}^i$ had been emitted by a transmitter at the target state $(\mathbf{t}, \dot{\mathbf{t}})$. This hypothetical situation is illustrated in Fig. 12. In this figure, the first leg of the target-path channel, which is faded, is replaced by the emission of $\tilde{\mathbf{u}}^i$ from the target. Note that $\tilde{\mathbf{u}}^i$ is simply the incident signal at the target after scaling and delay-Doppler compensation associated with one-way propagation from the transmitter at $(\mathbf{d}^i, \dot{\mathbf{d}}^i)$ to the target at $(\mathbf{t}, \dot{\mathbf{t}})$. Note also that the bistatic reflectivity α^{ij} , which typically differs between transmitter-receiver pairs in multistatic geometries, is incorporated into the channel coefficient $\gamma_{t,2}^{ij}(\mathbf{t})$ according to (53). This result is intuitive because a target may be interpreted as “emitting” each incident signal via the scattering process, where the reflectivity α^{ij} represents the “antenna gain” in the direction of the j th receiver.

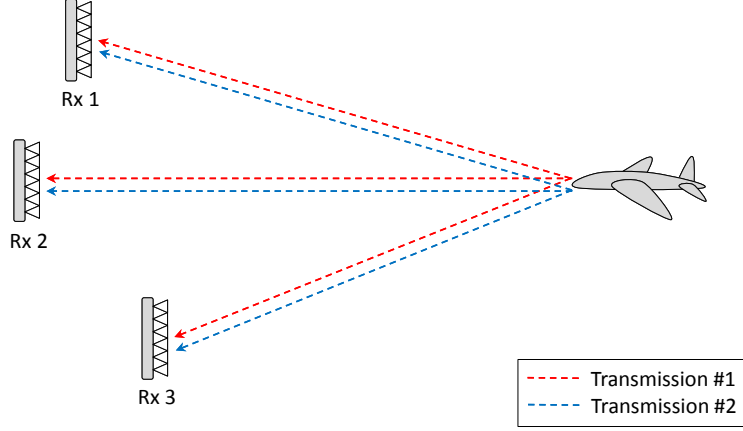


Figure 11. A PSL Sensor Network with Three Receivers

One consequence of this interpretation is that knowledge of the transmitter states $\{(\mathbf{d}^i, \dot{\mathbf{d}}^i)\}$ is unnecessary for detection in PMR networks that lack direct-path references. This can be seen for ξ_{ss} by examining the jk th element of \mathbf{G}_{ss}^i . Let $\mathcal{D}_p^{ij} = \mathcal{D}_{p,2}^{ij} \mathcal{D}_{p,1}^i$, where $\mathcal{D}_{p,1}^i$ and $\mathcal{D}_{p,2}^{ij}$ denote the delay-Doppler operators of the first and second legs of the target-path channel with respect to the i th transmitter, j th receiver, and hypothesized state $(\mathbf{p}, \dot{\mathbf{p}})$. Then

$$[\mathbf{G}_{ss}^i]_{jk} = \tilde{\mathbf{s}}_s^{ijH} \tilde{\mathbf{s}}_s^{ik} \quad (101)$$

$$= (\mathcal{D}_p^{ijH} \mathbf{s}_s^{ij})^H (\mathcal{D}_p^{ikH} \mathbf{s}_s^{ik}) \quad (102)$$

$$= \mathbf{s}_s^{ijH} \mathcal{D}_{p,2}^{ij} \mathcal{D}_{p,1}^i \mathcal{D}_{p,1}^{iH} \mathcal{D}_{p,2}^{ikH} \mathbf{s}_s^{ik} \quad (103)$$

$$= (\mathcal{D}_{p,2}^{ijH} \mathbf{s}_s^{ij})^H (\mathcal{D}_{p,2}^{ikH} \mathbf{s}_s^{ik}) \quad (104)$$

Therefore, $\tilde{\mathbf{s}}_s^{ij}$ may equivalently be defined to consider only one-way delay-Doppler compensation with respect to $(\mathbf{p}, \dot{\mathbf{p}})$,

$$\tilde{\mathbf{s}}_s^{ij} = \mathcal{D}_{p,2}^{ijH} \mathbf{s}_s^{ij} \quad (105)$$

because any delay-Doppler compensation with respect to the first leg of the target-

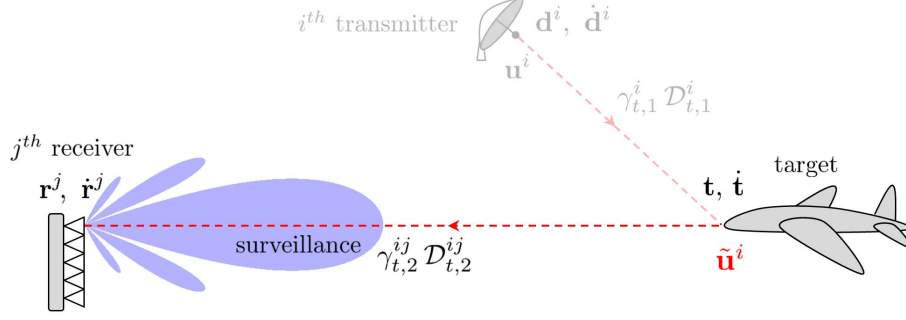


Figure 12. Interpretation of PMR without References as a PSL Scenario

path channel cancels in calculation of $[\mathbf{G}_{ss}^i]_{jk}$. Note that Wang and Yazici make the same observation with regard to calculation of their statistic [84]. Note also that the GLRT statistic ξ_{ss} reduces to the statistic of Vankayalapati and Kay derived for detection in PSL sensor networks in [83] when: single-channel receivers are used ($N_e = 1$); the target emits on a single transmit channel ($N_t = 1$); and (105) is used for $\tilde{\mathbf{s}}_s^{ij}$. This confirms the equivalence between PSL sensor networks and PMR sensor networks that lack direct-path references.

Additional insight into this equivalence is provided by examining the ambiguity characteristics of the proposed detector, i.e., examining how ξ_{ss} varies with mismatch between the hypothesized cell under test $(\mathbf{p}, \dot{\mathbf{p}})$ and the true target state $(\mathbf{t}, \dot{\mathbf{t}})$. If there is mismatch between \mathbf{t} and \mathbf{p} , then the target angle-of-arrival is possibly mismatched to the hypothesized angle-of-arrival, resulting in a mismatch loss. In this circumstance, the surveillance signal \mathbf{s}_s^{ij} in (73) may be expressed as

$$\mathbf{s}_s^{ij} = \tilde{\mu}_s^{ij} \mathbf{D}_t^{ij} \mathbf{u}^i + \mathbf{n}_s^{ij} \quad (106)$$

where $\tilde{\mu}_s^{ij} = \beta_{pt}^{ij} \mu_s^{ij}$ and $\beta_{pt}^{ij} = (\mathbf{a}_p^{ij})^H \mathbf{a}_t^{ij} / N_e$ quantifies the angular mismatch loss. Note that $|\beta_{pt}^{ij}| \leq 1$, and $\beta_{pt}^{ij} = 1$ iff $\mathbf{a}_p^{ij} = \mathbf{a}_t^{ij}$, i.e., when \mathbf{p} and \mathbf{t} are at the same angle with

respect to the j th receiver. Inserting (106) into (104), and ignoring receiver noise,

$$[\mathbf{G}_{ss}^i]_{jk} = \tilde{\mu}_s^{ij*} \tilde{\mu}_s^{ik} \mathbf{u}^{iH} \mathcal{D}_t^{ijH} \mathcal{D}_{p,2}^{ij} \mathcal{D}_{p,2}^{ikH} \mathcal{D}_t^{ik} \mathbf{u}^i \quad (107)$$

Recall that $\mathcal{D}_t^{ij} = \mathcal{D}(\ell_t^{ij}, \nu_t^{ij})$, where $\mathcal{D}(\ell, \nu)$ is the delay-by- ℓ and Doppler shift-by- ν operator defined by (47) in Sec. 2.3, ℓ_t^{ij} is the target-path propagation delay in samples, and ν_t^{ij} is the target-path Doppler shift in radians per sample. Similarly, $\mathcal{D}_{p,2}^{ij} = \mathcal{D}(\ell_{p,2}^j, \nu_{p,2}^{ij})$, where $\ell_{p,2}^j$ is the direct-path delay between the hypothesized state and the j th receiver in samples, and $\nu_{p,2}^{ij}$ is the corresponding direct-path Doppler shift in radians per sample. Then, (107) may be expressed after simplification as

$$[\mathbf{G}_{ss}^i]_{jk} = \tilde{\mu}_s^{ij*} \tilde{\mu}_s^{ik} \mathbf{u}^{iH} \mathcal{D}(\Delta \ell_p^{jk} - \Delta \ell_t^{jk}, \Delta \nu_p^{jk} - \Delta \nu_t^{jk}) \mathbf{u}^i \quad (108)$$

$$= \tilde{\mu}_s^{ij*} \tilde{\mu}_s^{ik} \chi^i(\Delta \ell_p^{jk} - \Delta \ell_t^{jk}, \Delta \nu_p^{i,jk} - \Delta \nu_t^{i,jk}) \quad (109)$$

where $\Delta \ell_p^{jk}$ and $\Delta \ell_t^{jk}$ are the TDOAs of the hypothesized and actual target signals with respect to the j th and k th receivers, respectively,

$$\Delta \ell_p^{jk} = \ell_{p,2}^j - \ell_{p,2}^k \quad (110)$$

$$\Delta \ell_t^{jk} = \ell_t^j - \ell_t^k \quad (111)$$

$\Delta \nu_p^{i,jk}$ and $\Delta \nu_t^{i,jk}$ are the FDOAs of the hypothesized and actual target signals with respect to the i th transmit channel and j th and k th receivers, respectively,

$$\Delta \nu_p^{i,jk} = \nu_{p,2}^{ij} - \nu_{p,2}^{ik} \quad (112)$$

$$\Delta \nu_t^{i,jk} = \nu_t^{ij} - \nu_t^{ik} \quad (113)$$

and $\chi^i(\Delta\ell, \Delta\nu)$ is the ambiguity function (AF) of \mathbf{u}^i ,

$$\chi^i(\Delta\ell, \Delta\nu) = \sum_{l=0}^{L-1} [\mathbf{u}^i]_l [\mathbf{u}^i]_{l+\Delta\ell}^* e^{j\Delta\nu l} \quad (114)$$

Noting that $\chi^i(\Delta\ell, \Delta\nu)$ peaks when its arguments are zero leads to the following iso-TDOA and iso-FDOA conditions:

$$\Delta\ell_p^{jk} = \Delta\ell_t^{jk} \quad (115)$$

$$\Delta\nu_p^{i,jk} = \Delta\nu_t^{i,jk} \quad (116)$$

In words, $[\mathbf{G}_{ss}^i]_{jk}$ peaks when (a) the hypothesized TDOA equals the actual target TDOA and (b) the hypothesized FDOA equals the actual target FDOA. This is representative of distributed PSL networks, which localize targets along contours of constant TDOA and FDOA [16, 86].

The preceding analysis considers only the elements of \mathbf{G}_{ss}^i , and it is not immediately clear how these entries affect the maximum eigenvalue of \mathbf{G}_{ss}^i . However, the simulation results in Sec. 3.5.2 confirm that the salient ambiguity properties of ξ_{ss} , which is a function of these eigenvalues, can be explained in terms of these iso-TDOA and iso-FDOA conditions.

3.5 Simulations

This section illustrates the detection and ambiguity performance of the proposed detector via numerical simulation. Numerical challenges associated with calculating the distributions presented in Sec. 3.3 are also discussed.

3.5.1 Detection Performance.

This section illustrates how detection performance varies with $\text{SNR}_{\text{avg}}^i$ and the system parameters N_t , N_r , and L . Recall from Sec. 3.3.3 that the distributions of ξ_{ss} are functions of only these four quantities; accordingly, these quantities determine detection performance. The influence of N_t and N_r on detection is discussed first, followed by L .

3.5.1.1 Number of Transmitters and Receivers.

Fig. 13 depicts probability of detection (P_d) curves as a function of $\text{SNR}_{\text{avg}}^i$ for a scenario with $L = 100$ samples per received signal and a varying number of transmitter and receivers². Both predicted and simulated P_d curves are shown for each transmitter-receiver configuration. The predicted curves are calculated according to the distributions presented in Sec. 3.3. The simulated curves are calculated using 10^5 trials under \mathcal{H}_0 to determine a detection threshold that achieves a probability of false alarm of 10^{-3} , and then using 5×10^4 trials for each $\text{SNR}_{\text{avg}}^i$ to determine P_d . For convenience, $\text{SNR}_{\text{avg}}^i$ are assumed to be equal across transmitters, i.e., $\text{SNR}_{\text{avg}}^i = \text{SNR}_{\text{avg}} \forall i$. The channel coefficients $\{\boldsymbol{\mu}_s^i : i = 1 \dots N_t\}$ are chosen randomly and scaled to achieve the desired $\text{SNR}_{\text{avg}}^i$ relative to the fixed noise power $\sigma^2 = 10^{-6}$. The transmit signals $\{\mathbf{u}^i : i = 1 \dots N_t\}$ are also chosen randomly according to $\mathbf{u}^i = \exp\{j\boldsymbol{\theta}^i\}$, where $\boldsymbol{\theta}^i \in \mathbb{R}^{L \times 1}$ is a random phase vector with i.i.d. elements uniformly distributed on $[0, 2\pi]$, such that $\|\mathbf{u}^i\|^2 = L$. Recall from the discussion in Sec. 3.3.3 that detection performance is independent of the specific values of $\boldsymbol{\mu}_s^i$ and \mathbf{u}^i , and depends on only

²Note that $\text{SNR}_{\text{avg}}^i$ describes the average SNR following surveillance channel formation. This may be regarded as an average *input* SNR because it does not include processing gain. In contrast, detection performance is often quantified in active radar in terms of the *output* SNR, which includes processing gain. Input SNR is chosen here rather than output SNR because, in contrast to active radar processing, the concept of processing gain is not well defined for passive processing as performed by the SS-GLRT. In particular, the SS-GLRT statistic cannot be divided into signal and noise terms, thereby preventing calculation of their power ratio.

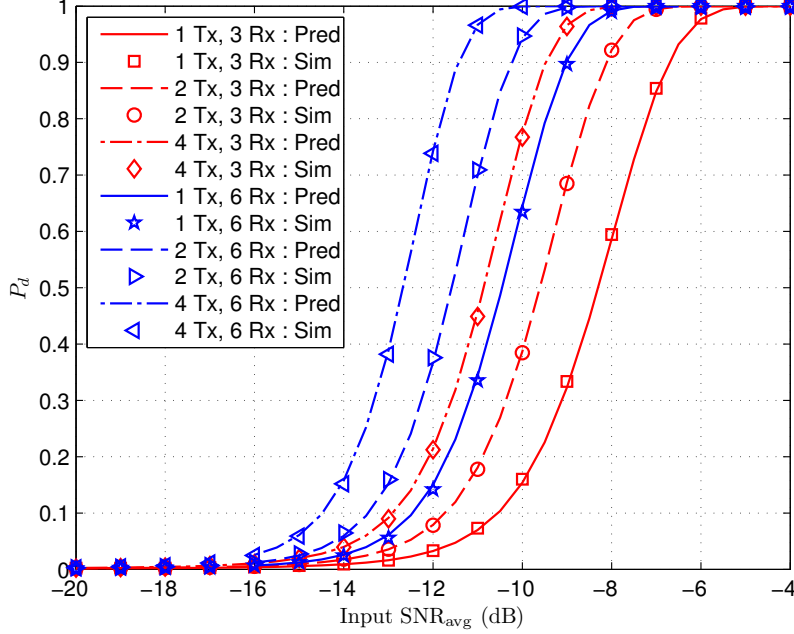


Figure 13. Predicted (Pred) and Simulated (Sim) P_d Curves for a PMR Network with a Varying Number of Transmitters and Receivers

their respective energies.

In all cases, the predicted and simulated results agree, verifying the distributions presented in Sec. 3.3. In addition, detection sensitivity appears to improve monotonically with increasing $\text{SNR}_{\text{avg}}^i$, N_t , and N_r , as expected. It also appears that detection sensitivity is improved more significantly by the number of receivers in the network than by the number of transmitters. Specifically, detection sensitivity does not depend solely on the number of bistatic pairs; rather, for a given total number of pairs, detection sensitivity improves with an increasing number of receivers. For example, consider the results for $(N_t, N_r) = (2, 3)$ and $(N_t, N_r) = (1, 6)$. Although both configurations use $N_t N_r = 6$ bistatic pairs, $(N_t, N_r) = (1, 6)$ exhibits superior detection sensitivity. The same holds when comparing $(N_t, N_r) = (4, 3)$ and $(N_t, N_r) = (2, 6)$, where $(N_t, N_r) = (2, 6)$ exhibits superior detection sensitivity. This result contrasts with active MIMO radar with distributed antennas, where detection sensitivity depends on only the total number of bistatic pairs in the system [24]. This

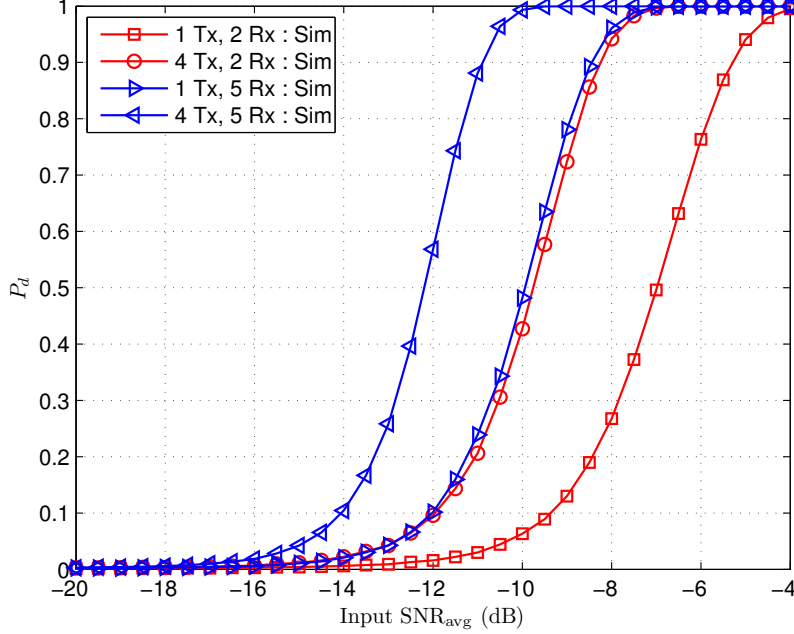


Figure 14. Additional P_d Curves for PMR Networks with a Varying Number of Transmitters and Receivers

asymmetry between transmitters and receivers is also evident when comparing networks with the same number of independent TDOAs/FDOAs. This is illustrated in Fig. 14, which depicts additional P_d curves for different cases than were previously considered in Fig. 13. Consider the results for $(N_t, N_r) = (4, 2)$ and $(N_t, N_r) = (1, 5)$. Although both configurations realize $N_t(N_r - 1) = 4$ independent TDOAs/FDOAs, $(N_t, N_r) = (1, 5)$ exhibits slightly superior detection sensitivity.

Although the specific reason for this asymmetry is unclear, it might be explained by noting that increasing the number of transmitters introduces more nuisance parameters into the problem in the form of unknown transmitted signals. Conversely, increasing the number of receivers provides more observations of each unknown transmitted signal, which enables each signal to be (implicitly) estimated more precisely during calculation of the SS-GLRT statistic.

3.5.1.2 Received Signal Length.

The previous experiment for $(N_t, N_r) = (2, 3)$ was repeated as L was varied over $L = [1, 3, 10, 30, 100, 300, 1000, 3000, 10000]$. The resulting P_d curves for $L = 1$ to $L = 1000$ are shown in Fig. 15. As expected, detection sensitivity improves with increasing L . This improvement may be quantified in terms of an integration gain $G_{\text{int}}(L)$, defined as the separation between the P_d curve for a given length $L > 1$ and the P_d curve for $L = 1$ at $P_d = 0.90$. For instance, the difference between the $L = 1$ and $L = 30$ curves at $P_d = 0.90$ is approximately 10 dB, indicating $G_{\text{int}} \approx 10$ dB. Fig. 16 shows G_{int} versus L . As shown, G_{int} varies between $L^{0.7}$ at $L = 10$ (10 dB) to just below $L^{0.6}$ at $L = 10000$ (40 dB). This behavior is inconsistent with coherent integration of L samples in active radar processing, for which $G_{\text{int}}(L) = L$. Rather, it is suggestive of non-coherent integration of L samples, for which G_{int} generally approaches $L^{0.5}$ with large L [71]. This result is likely due to the fact that each element of \mathbf{G}_{ss}^i is the inner product of two noisy surveillance signals. Calculation of this inner product results in signal-noise cross terms that are similar to those produced in square-law non-coherent integration. In contrast, coherent integration is realized in active radar processing by matched filtering, in which each noisy surveillance signal is correlated with a noiseless reference signal.

3.5.2 Ambiguity Performance.

This section illustrates the ambiguity performance of the SS-GLRT for a scenario with two stationary transmitters at $\mathbf{d}^1 = [0.5, 4]$ km and $\mathbf{d}^2 = [-0.5, -4]$ km, three stationary receivers at $\mathbf{r}^1 = [-4, 2]$ km, $\mathbf{r}^2 = [-4, 0.5]$ km and $\mathbf{r}^3 = [-4, -2.5]$ km, and a target at $\mathbf{t} = [4, 0]$ km. Both single-element and 6-element uniform linear array (ULA) receivers are considered. The transmitters have carrier frequencies of 8.0 and 8.1 GHz, respectively, and isotropic $P_{\text{erp}}^i = 50$ W. Complex baseband signals \mathbf{s}_n^{ij} are

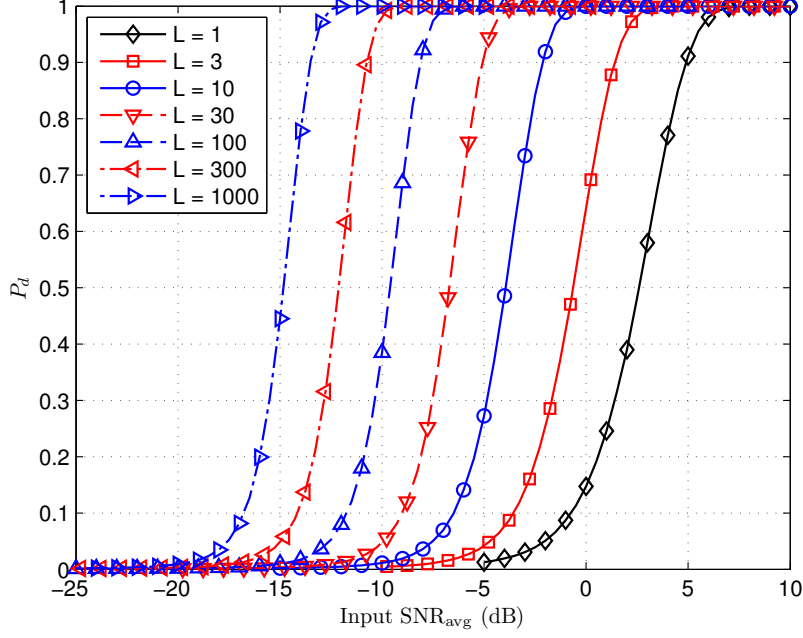


Figure 15. P_d Curves for a PMR Scenario with 2 Transmitters, 3 Receivers, and $L = [1, 3, 10, 30, 100, 300, 1000]$ Samples per Signal

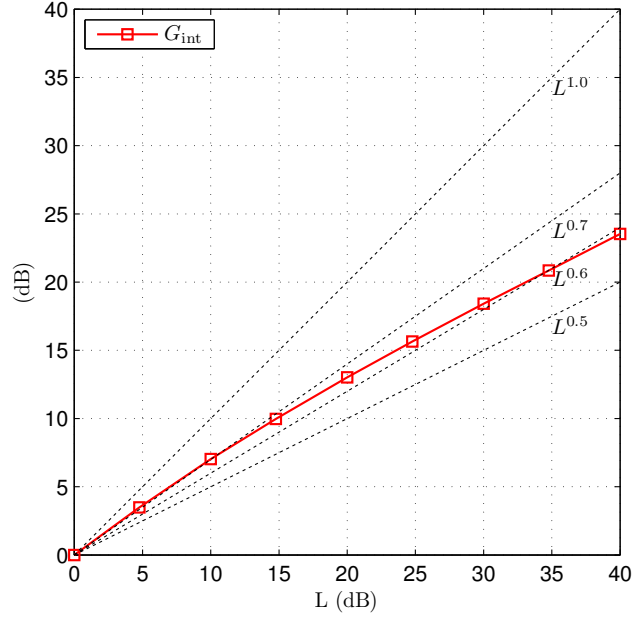


Figure 16. Integration Gain G_{int} as a Function of L for a PMR Scenario with 2 Transmitters and 3 Receivers

simulated according to (51) (ignoring receiver noise) with sampling rate $f_s = 500$ kHz, length $T = 10$ ms, and $\mathbf{u}^i = \exp\{j\boldsymbol{\theta}^i\}$, where $\boldsymbol{\theta}^i \in \mathbb{R}^{L \times 1}$ is a random phase vector with

i.i.d. elements uniformly distributed on $[0, 2\pi]$ and length $L = f_s T = 5000$. The target has an isotropic 10 dBsm RCS, i.e., $\alpha^{ij} = \sqrt{10}$ for all i and j . Note that the receivers are not phase-synchronized due to the random phase θ^j in the channel coefficient γ_t^{ij} according to (38) in Sec. 2.2.2.

In contrast to usual discussions of radar ambiguity, which examine the effect of delay and Doppler mismatch on the matched filter output assuming a given transmit waveform, this section examines the effect of position and velocity mismatch between the hypothesized state $(\mathbf{p}, \dot{\mathbf{p}})$ and the actual target state $(\mathbf{t}, \dot{\mathbf{t}})$ on the SS-GLRT test statistic ξ_{ss} . This perspective provides insight into how system properties, such as the number of receivers and transmitters and their relative geometries, affect system-level ambiguity in the detection domain, which in this formulation is Cartesian position-velocity space. Nonetheless, as discussed in Sec. 3.4, system-level ambiguity in Cartesian position-velocity space depends on waveform ambiguity in delay-Doppler space in that the elements of the Gram matrix \mathbf{G}_{ss}^i sample the AF of the i th transmit waveform \mathbf{u}^i , $\chi^i(\Delta\ell, \Delta\nu)$. Fig. 17 depicts the normalized AF for one of the signals in the present scenario as a function of delay $\Delta\tau = \Delta\ell/f_s$ and Doppler $\Delta f_d = f_s \Delta\nu/(2\pi)$ mismatch. As shown, delay resolution is $1/f_s = 2 \mu\text{s}$, Doppler resolution is $1/T = 100$ Hz, and the AF floor is $10 \log_{10}(L) \approx 37$ dB below the mainlobe peak.

3.5.2.1 Stationary Target.

Consider, first, a stationary target. Fig. 18 depicts ξ_{ss} as a function of hypothesized position $\mathbf{p} = [p_x, p_y]$ when the hypothesized velocity is matched to the true target velocity $\dot{\mathbf{p}} = \dot{\mathbf{t}} = \mathbf{0}$, i.e., $\xi_{ss}(\mathbf{p}, \dot{\mathbf{p}})|_{\dot{\mathbf{p}}=\mathbf{0}}$. Each receiver consists of a single element, $N_e = 1$, with isotropic element pattern $G_e^j(\mathbf{x}) = 1 \forall j$. As shown, the test statistic peaks at the true target position, and it exhibits a ridge along the target iso-TDOA contours associated with each of the three receiver-receiver pairs. Each iso-TDOA

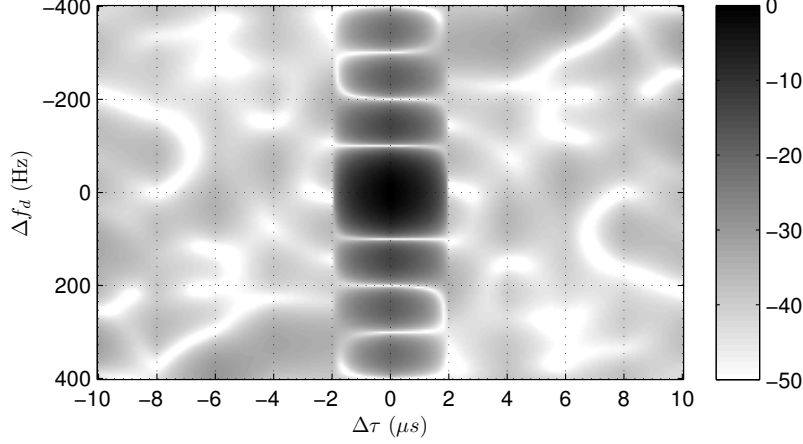


Figure 17. Example Transmit Signal Ambiguity Function $\chi^i(\Delta\tau, \Delta f_d)$ (dB)

contour represents the positions at which the TDOA of the hypothesized state equals that of the actual target state, i.e., $\Delta\ell_p^{jk} = \Delta\ell_t^{jk}$ for the jk th receiver-receiver pair. This is illustrated in Fig. 19, which depicts the TDOA $\Delta\tau_p^{jk} = \Delta\ell_p^{jk}/f_s$ as a function of \mathbf{p} for $j = 2$ and $k = 3$. The target iso-TDOA contour $\Delta\tau_p^{23} = \Delta\tau_t^{23}$ is denoted by the red dash-dotted hyperbola. Note that $\Delta\nu_p^{i,jk} = \Delta\nu_t^{i,jk} = 0$ for all i, j, k and \mathbf{p} in this example, i.e., the hypothesized and actual FDOAs equal zero everywhere, because the considered scenario is stationary.

This result is consistent with the analysis presented in Sec. 3.4. From (109), the jk th element of \mathbf{G}_{ss}^i is proportional to $\chi^i(\Delta\ell_p^{jk} - \Delta\ell_t^{jk}, 0)$. When $\Delta\ell_p^{jk} = \Delta\ell_t^{jk}$, i.e., along the target iso-TDOA contour, this element samples the AF peak. When there is mismatch between $\Delta\ell_p^{jk}$ and $\Delta\ell_t^{jk}$, this element samples the AF at a location that is offset from the AF peak along the zero-Doppler ($\Delta f_d = 0$) cut. This results in the appearance of ambiguity “ridges” along the iso-TDOA lines that correspond to the target signal TDOA.

The effect of multichannel receivers is seen in Fig. 20, which depicts $\xi_{ss}(\mathbf{p}, \dot{\mathbf{p}})|_{\dot{\mathbf{p}}=\mathbf{0}}$ when each receiver is a 6-element ULA facing the $+p_x$ direction with 1.875 cm element spacing and unity element patterns. In comparison to Fig. 18, beamforming

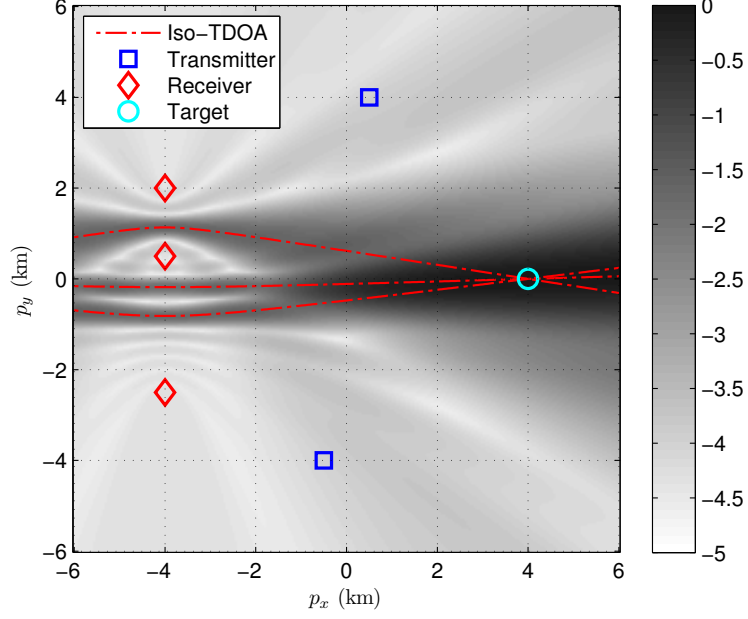


Figure 18. $\xi_{ss}(\mathbf{p}, \dot{\mathbf{p}})|_{\dot{\mathbf{p}}=0}$ (dB) for $\dot{\mathbf{t}} = 0$ and Single-Element Receivers

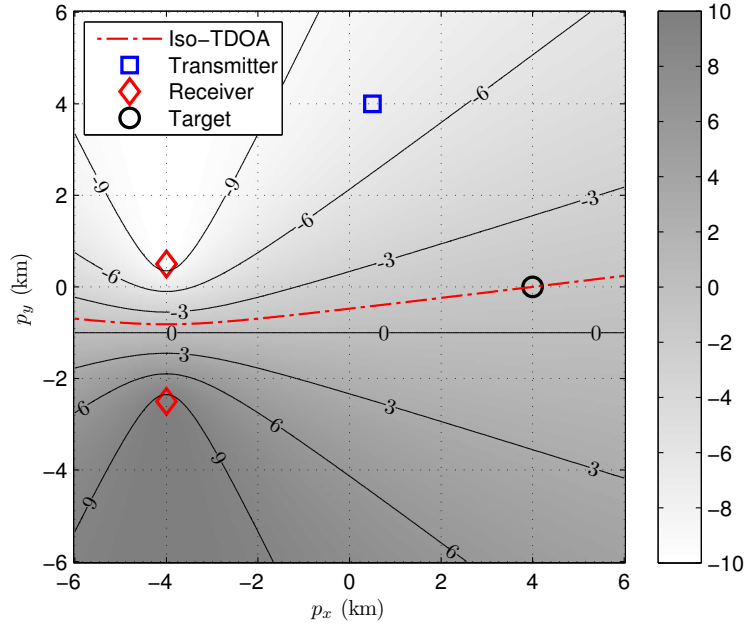


Figure 19. TDOA $\Delta\tau_p^{jk} = \Delta\ell_p^{jk}/f_s$ (μs) for $j = 2$ and $k = 3$

during surveillance channel formation sharpens the response of ξ_{ss} around \mathbf{t} . This is expected from the discussion of the angular mismatch loss β_{pt}^{ij} in Sec. 3.4. Thus, use of multichannel receivers appears to reduce detection ambiguity (and improve target

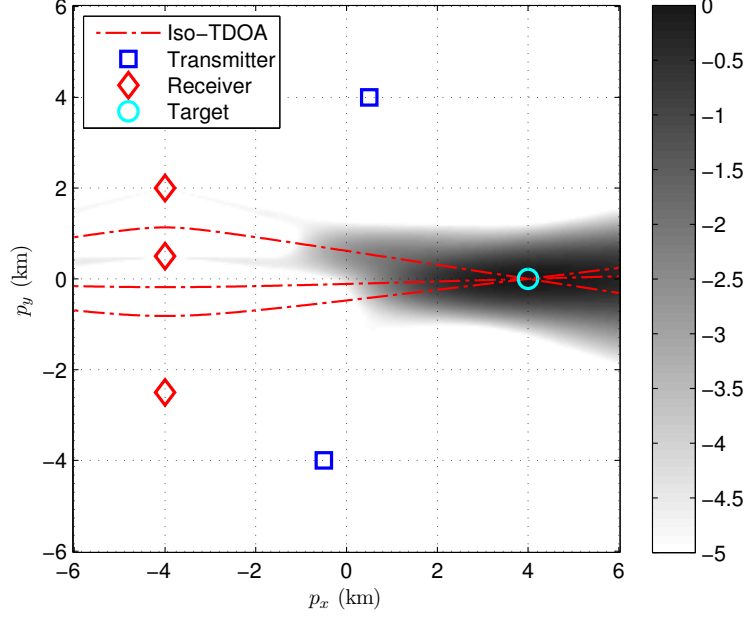


Figure 20. $\xi_{ss}(\mathbf{p}, \dot{\mathbf{p}})|_{\dot{\mathbf{p}}=0}$ (dB) for $\dot{\mathbf{t}} = 0$ and Six-Element ULA Receivers

localization performance) in comparison to single-element receivers.

3.5.2.2 Moving Target.

Next, consider a moving target with velocity $\dot{\mathbf{t}} = [\dot{p}_x, \dot{p}_y] = [-75, 75]$ m/s. Fig. 21 depicts ξ_{ss} as a function of \mathbf{p} when $\dot{\mathbf{p}} = \dot{\mathbf{t}}$ assuming isotropic single-element receivers. As expected, ξ_{ss} still peaks at $\mathbf{p} = \mathbf{t}$, where the iso-TDOA and iso-FDOA constraints are satisfied for all receiver-receiver pairs. However, in comparison to Fig. 18, Fig. 21 exhibits the additional effects of FDOA mismatch between receiver pairs when $\mathbf{p} \neq \mathbf{t}$. This is seen by the manner in which ξ_{ss} decreases with separation from the target iso-FDOA contours, which are depicted by dashed blue lines, in addition to the iso-TDOA contours. Such FDOA mismatch results even though $\dot{\mathbf{p}} = \dot{\mathbf{t}}$ at all \mathbf{p} because the hypothesized FDOA that is induced for each receiver-receiver pair still varies as a function of \mathbf{p} . This is illustrated in Fig. 22, which illustrates the hypothesized FDOA (kHz) as a function of \mathbf{p} for one receiver-receiver pair, assuming $\dot{\mathbf{p}} = \dot{\mathbf{t}}$. The target iso-FDOA contour is shown by the dashed blue line. Unlike iso-TDOA contours,

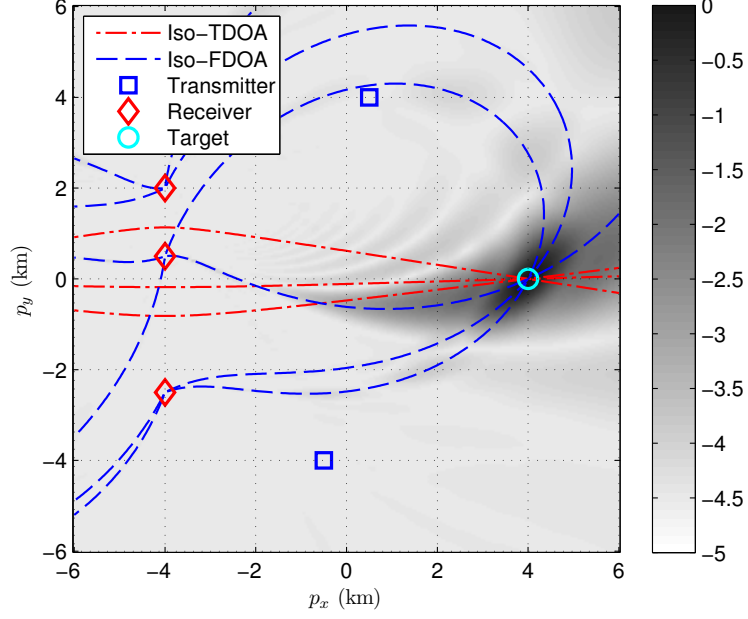


Figure 21. $\xi_{ss}(\mathbf{p}, \dot{\mathbf{p}})|_{\dot{\mathbf{p}}=\mathbf{0}}$ (dB) for $\dot{\mathbf{t}} = \mathbf{0}$ and Single-Element Receivers

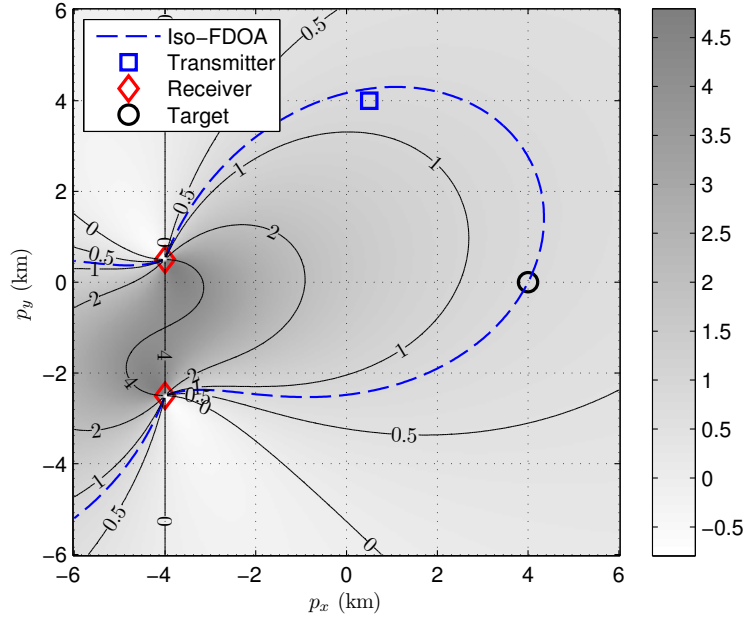


Figure 22. FDOA $\left(\frac{f_s}{2\pi}\right)\Delta\nu_p^{i,jk}(\mathbf{p}, \dot{\mathbf{p}})|_{\dot{\mathbf{p}}=\dot{\mathbf{t}}}$ (kHz) for $i = 1$, $j = 2$, and $k = 3$

which are hyperbolas in two dimensions, iso-FDOA contours do not admit a simple analytic description.

Finally, Fig. 23 depicts $\xi_{ss}(\mathbf{p}, \dot{\mathbf{p}})|_{\dot{\mathbf{p}}=\dot{\mathbf{t}}}$ when each receiver is the 6-element ULA

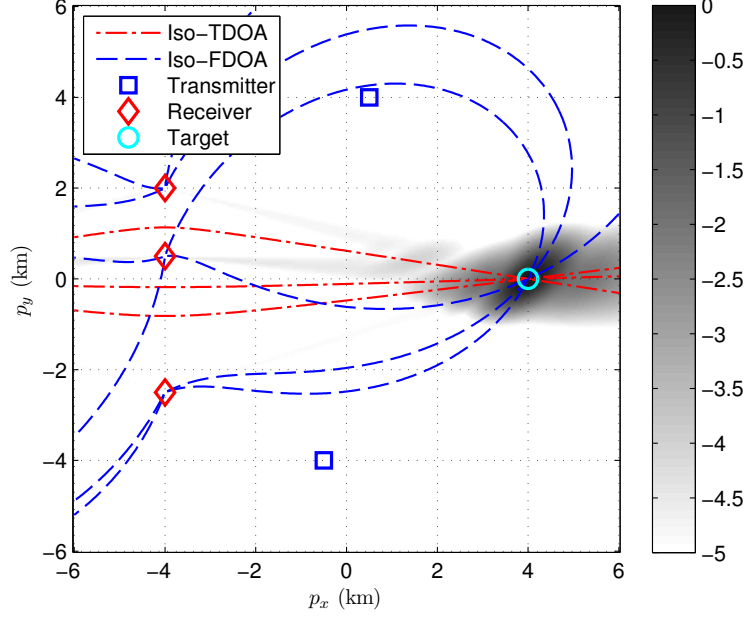


Figure 23. $\xi_{ss}(\mathbf{p}, \hat{\mathbf{p}})|_{\hat{\mathbf{p}}=\mathbf{0}}$ (dB) for $\dot{\mathbf{t}} = \mathbf{0}$ and Six-Element ULA Receivers

described previously. Similar to Fig. 20, the peak around the true target position is sharpened due to the attenuation resulting from angular mismatch between the actual and hypothesized target positions. Thus, the statistic ξ_{ss} is influenced by an angular constraint with multichannel receivers in addition to the iso-TDOA and iso-FDOA constraints.

3.5.3 Numerical Challenges.

Calculating the distributions required for Fig. 13 proved challenging. Direct calculation of the PDF $f_1(\xi; N_r, L, \zeta_{ss}^i)$ in (88) proved infeasible for large ζ_{ss}^i and order $L \geq 10$ without variable precision arithmetic because the required calculations exceeded the largest double precision floating-point number defined by IEEE Standard 754, which is approximately 1.79769×10^{308} . Use of variable precision arithmetic in Mathematica alleviated this problem; however, the resulting calculations were extremely time consuming. It was found that estimating this PDF by numerically differentiating the associated cumulative distribution function (CDF), which is also

given by [48], provided a significant speed improvement. This approach avoids calculation of the matrix inverse $\Psi^{-1}(\phi)$, which is a challenging operation because $\Psi(\phi)$ is often poorly conditioned due to the large dynamic range of its entries. The PDF $f_1(\xi; N_r, L, \zeta_{ss}^i)$ was successfully calculating using this approach over the range of considered SNR_{avg} for $L \leq 100$ when $N_r \leq 6$. Calculations for larger L or N_r did not result in valid CDFs and remains a topic for future investigation.

3.6 Conclusion

In this chapter, a GLRT for centralized detection in PMR networks that operate without direct-path reference signals, termed the surveillance-surveillance GLRT, was presented. The distributions of the SS-GLRT test statistic were identified under both hypotheses using recent results from random matrix theory that pertain to the distributions of the largest eigenvalues of complex Wishart matrices. This detection problem was shown to be equivalent to detection in PSL sensor networks when the source simultaneously emits on multiple transmit channels. Through numerical simulation, it was shown that transmitters and receivers contribute asymmetrically to detection sensitivity in such sensor networks. It was also shown that increasing the received signal length improves sensitivity in a manner that is consistent with non-coherent integration gain rather than coherent integration gain. Analysis and simulation of system-level ambiguity also showed that the SS-GLRT localizes targets in angle, TDOA, and FDOA, in a manner analogous to PSL sensor networks that utilize AOA, TDOA, and FDOA.

IV. Passive MIMO Radar Detection with References

This chapter¹ addresses the problem of target detection in PMR networks when direct-path signals are available, shown in Fig. 24. As discussed in Sec. 1.4.1, the conventional approach to PMR detection approximates the matched filter processing used in AMR networks. In particular, for each bistatic (transmitter-receiver) pair, the direct-path and target-path signals are isolated into reference and surveillance channels, respectively, and the reference-surveillance cross-ambiguity function (CAF) is calculated. Calculation of the CAF is analogous to matched filtering in active radar, except the (noisy) reference channel is used in place of a known transmit signal. As discussed in Sec. 1.4.1, this approach is *ad hoc* for PMR because matched filtering is only optimal for known transmit signals. In low-DNR scenarios, this approach is severely degraded due to mismatch between reference channels and the originally transmitted signals. Consequently, this approach does not represent a general solution to the PMR detection with references problem, but is only suitable for high-DNR scenarios, in which references closely approximate the unknown transmit signals.

This chapter presents a novel centralized GLRT for the PMR with references

¹The material in this chapter appears in [37].

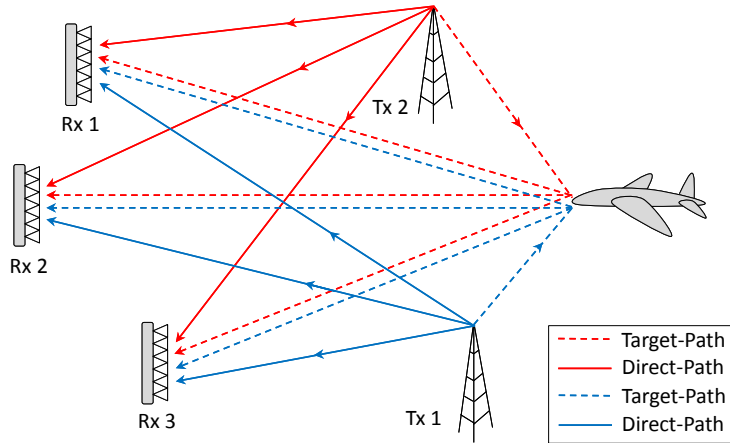


Figure 24. A Passive MIMO Radar Sensor Network

detection problem. This detection problem is formulated in terms of the incident signal at each element of a passive radar array receiver, which is the superposition of a target-path signal, a direct-path signal, and receiver noise. In addition, the detection problem formulation assumes non-isotropic target scattering, and makes no assumption about coherence between receivers. The resulting detector, termed the *reference-surveillance* GLRT (RS-GLRT) because it forms and processes both reference and surveillance channels, represents a general solution to the PMR detection problem that addresses how detection sensitivity depends on both SNR and DNR. In this way, the RS-GLRT confirms the research hypothesis presented in Sec. 1.5.

The detection and ambiguity performance of the RS-GLRT is compared against that of two closely related detectors, termed the matched filter GLRT (MF-GLRT) and surveillance-surveillance GLRT (SS-GLRT), which are GLRTs for centralized detection in AMR and PSL sensor networks, respectively. PSL and AMR represent two extremes in terms of knowledge about the transmitted signals, i.e., the signals are entirely unknown in PSL and entirely known in AMR. It is shown that the RS-GLRT varies between both extremes as a function of the average DNR. When the DNR is low, PMR detection performance approximates PSL detection performance. When the DNR is high, PMR detection performance approaches AMR detection performance. It is also shown that the RS-GLRT test statistic, which is a function of the largest eigenvalues of complex Wishart matrices, is approximately proportional to the AMR test statistic under the high-DNR condition. These results lay the groundwork for the unified detection framework presented in Chapter V.

4.1 Signal Model

Consider a PMR network with N_t transmitters and N_r receivers. Fig. 25 depicts the geometry and signal environment of the ij th bistatic pair, consisting of the

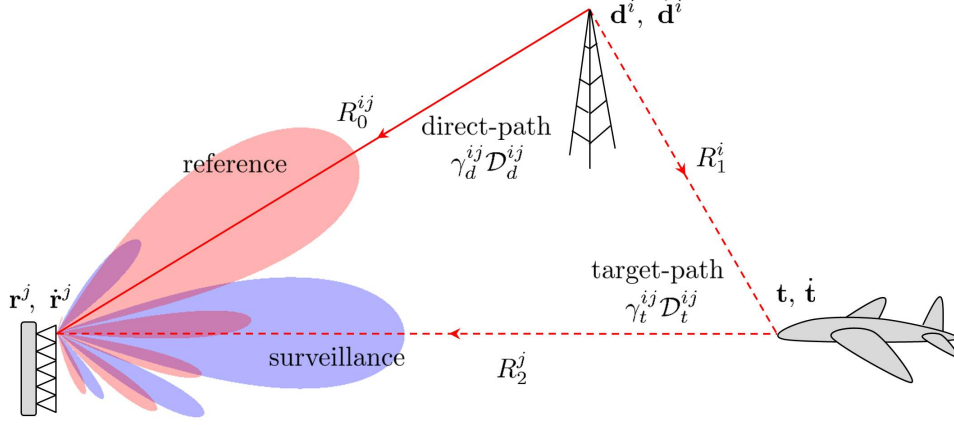


Figure 25. The ij th Bistatic (Transmitter-Receiver) Pair in a PMR Network

i th transmitter and j th receiver. The position and velocity of the i th transmitter are denoted by \mathbf{d}^i and $\dot{\mathbf{d}}^i$, and the position and velocity of the j th receiver by \mathbf{r}^j and $\dot{\mathbf{r}}^j$. The spatial states of all transmitters and receivers are assumed known. In the passive radar signal environment, direct-path, target-path, and clutter-path signals are incident at each array. It will be shown that the RS-GLRT can be interpreted as forming surveillance and reference channels, and clutter can be mitigated in these channels through a variety of techniques discussed in Sec. 1.1.2. Furthermore, detection performance in a clutter-free noise-only environment represents an upper bound against which the performance of clutter-suppressing detectors can be compared. As such, only direct-path and target-path signals are considered here.

Assume the transmitted signals are separable in frequency, and that each receiver is equipped with an N_e -element array. The incident signal at the n th element of the j th receiver is the sum of the direct-path and target-path signals from each transmitter. This signal is channelized in frequency, demodulated to baseband, and sampled in time. Chapter II describes this process in detail. Let $\mathbf{s}_n^{ij} \in \mathbb{C}^{L^i \times 1}$ denote the length- L^i sampled complex baseband signal on the i th frequency channel of the n th array element of the j th receiver array. For simplicity, it is assumed that $L^i = L \forall i$. Assuming a target at position \mathbf{t} and velocity $\dot{\mathbf{t}}$, \mathbf{s}_n^{ij} is given by Eq. (50) in

Sec. 2.3 as

$$\mathbf{s}_n^{ij} = \gamma_d^{ij} e^{j\vartheta_n^{ij}(\mathbf{d}^i)} \mathcal{D}_d^{ij} \mathbf{u}^i + \gamma_t^{ij} e^{j\vartheta_n^{ij}(\mathbf{t})} \mathcal{D}_t^{ij} \mathbf{u}^i + \mathbf{n}_n^{ij} \quad (117)$$

where $\mathbf{u}^i \in \mathbb{C}^{L \times 1}$ is the length- L discrete-time complex baseband signal emitted by the i th transmitter; $\mathcal{D}_d^{ij} \in \mathbb{C}^{L \times L}$ and $\mathcal{D}_t^{ij} \in \mathbb{C}^{L \times L}$ are unitary linear operators that account for the delays and Doppler shifts imparted to the i th transmit signal as it propagates to the j th receiver along the direct-path and target-path channels, respectively; $\vartheta_n^{ij}(\mathbf{d}^i)$ and $\vartheta_n^{ij}(\mathbf{t})$ are differential phases at the n th array element with respect to a reference element due to plane wave propagation from the i th transmitter and target directions, respectively; γ_d^{ij} and γ_t^{ij} account for the complex scaling of \mathbf{u}^i associated with the ij th direct-path and target-path channels, respectively; $\mathbf{n}_n^{ij} \in \mathbb{C}^{L \times 1}$ is circular Gaussian noise distributed as $\mathcal{CN}(\mathbf{0}_L, \sigma^2 \mathbf{I}_L)$ with known variance σ^2 ; and $j = \sqrt{-1}$. Here, $\mathbf{0}_L$ denotes the length- L zero vector, and \mathbf{I}_L is the $L \times L$ identity matrix. The delay-Doppler operators \mathcal{D}_d^{ij} and \mathcal{D}_t^{ij} are defined

$$\mathcal{D}_d^{ij} = \mathcal{D}(\ell_d^{ij}, \nu_d^{ij}) \quad (118)$$

$$\mathcal{D}_t^{ij} = \mathcal{D}(\ell_t^{ij}, \nu_t^{ij}) \quad (119)$$

where $\mathcal{D}(\ell, \nu)$ is the delay-by- ℓ and Doppler shift-by- ν operator defined by Eq. (47) in Sec. 2.3, ℓ_d^{ij} and ℓ_t^{ij} are the delays of the direct-path and target-path channels in samples, respectively, and ν_d^{ij} and ν_t^{ij} are the Doppler shifts of the direct-path and target-path channels in radians per sample, respectively. Noise is assumed to be independent across transmit bands, receivers, and array elements, i.e., $\mathbb{E}\{\mathbf{n}_n^{ij}(\mathbf{n}_m^{kl})^H\} = \sigma^2 \delta_{n-m} \delta_{i-k} \delta_{j-l} \mathbf{I}_L$, where $(\cdot)^H$ is the Hermitian transpose and δ_x is the Kronecker delta. The transmit signal \mathbf{u}^i is defined such that $\|\mathbf{u}^i\|^2 = L$. Additional detail on the terms in (117) is found in Chapter II.

Let $\mathbf{a}^{ij}(\mathbf{x}) \in \mathbb{C}^{N_e \times 1}$ denote the spatial steering vector in the direction of \mathbf{x} ,

$$\mathbf{a}^{ij}(\mathbf{x}) = \begin{bmatrix} e^{j\theta_1^{ij}(\mathbf{x})} & e^{j\theta_2^{ij}(\mathbf{x})} & \dots & e^{j\theta_{N_e}^{ij}(\mathbf{x})} \end{bmatrix}^T \quad (120)$$

For convenience, let $\mathbf{a}_d^{ij} = \mathbf{a}^{ij}(\mathbf{d}^i)$ and $\mathbf{a}_t^{ij} = \mathbf{a}^{ij}(\mathbf{t})$. Then, the concatenation of the time series vectors from all N_e elements of the j th receiver in the i th frequency band, $\mathbf{s}^{ij} = [(\mathbf{s}_1^{ij})^T \dots (\mathbf{s}_{N_e}^{ij})^T]^T \in \mathbb{C}^{N_e L \times 1}$, can be written as

$$\mathbf{s}^{ij} = (\mathbf{M}_d^{ij} + \mathbf{M}_t^{ij})\mathbf{u}^i + \mathbf{n}^{ij} \quad (121)$$

where $\mathbf{n}^{ij} = [(\mathbf{n}_1^{ij})^T \dots (\mathbf{n}_{N_e}^{ij})^T]^T \in \mathbb{C}^{N_e L \times 1}$, the matrices \mathbf{M}_d^{ij} and \mathbf{M}_t^{ij} are defined as

$$\mathbf{M}_d^{ij} = \gamma_d^{ij} (\mathbf{a}_d^{ij} \otimes \mathcal{D}_d^{ij}) \in \mathbb{C}^{N_e L \times L} \quad (122)$$

$$\mathbf{M}_t^{ij} = \gamma_t^{ij} (\mathbf{a}_t^{ij} \otimes \mathcal{D}_t^{ij}) \in \mathbb{C}^{N_e L \times L} \quad (123)$$

and \otimes is the Kronecker product.

4.2 Detectors

This section presents a derivation of the RS-GLRT detector. Following this, the SS-GLRT and MF-GLRT detectors, which correspond to detection in PSL and AMR sensor networks, respectively, are presented.

4.2.1 Reference-Surveillance GLRT.

For a given position-velocity cell under test $(\mathbf{p}, \dot{\mathbf{p}})$, the detection problem may be formulated as a binary hypothesis test between \mathcal{H}_1 and \mathcal{H}_0 hypotheses as

$$\mathcal{H}_1 : \mathbf{s}^{ij} = (\mathbf{M}_d^{ij} + \mathbf{M}_p^{ij})\mathbf{u}^i + \mathbf{n}^{ij} \quad (124)$$

$$\mathcal{H}_0 : \mathbf{s}^{ij} = \mathbf{M}_d^{ij}\mathbf{u}^i + \mathbf{n}^{ij} \quad (125)$$

for $i = 1 \dots N_t$ and $j = 1 \dots N_r$. In (124), \mathbf{M}_p^{ij} is defined

$$\mathbf{M}_p^{ij} = \gamma_p^{ij} (\mathbf{a}_p^{ij} \otimes \mathcal{D}_p^{ij}) \in \mathbb{C}^{N_e L \times L} \quad (126)$$

where γ_p^{ij} is the target-path channel coefficient associated with \mathbf{p} , $\mathbf{a}_p^{ij} = \mathbf{a}^{ij}(\mathbf{p})$, and \mathcal{D}_p^{ij} is the delay-Doppler operator associated with the hypothesized state $(\mathbf{p}, \dot{\mathbf{p}})$. Let \mathbf{s}^i denote the concatenation of all receiver measurements associated with the i th transmitter, and let \mathbf{s} denote the concatenation of all \mathbf{s}^i across transmitters,

$$\mathbf{s}^i = [(\mathbf{s}^{i1})^T, \dots, (\mathbf{s}^{iN_r})^T]^T \in \mathbb{C}^{N_r L \times 1} \quad (127)$$

$$\mathbf{s} = [(\mathbf{s}^1)^T, \dots, (\mathbf{s}^{N_t})^T]^T \in \mathbb{C}^{N_t N_r L \times 1} \quad (128)$$

Similarly, let $\boldsymbol{\gamma}_{(d,p)}^i$ denote the vector of channel coefficients associated with the i th transmitter, where the subscript notation $(\cdot)_{(d,p)}$ denotes either $(\cdot)_d$ or $(\cdot)_p$, and let $\boldsymbol{\gamma}_{(d,p)}$ denote the concatenation of all $\boldsymbol{\gamma}_{(d,p)}^i$ across transmitters²,

$$\boldsymbol{\gamma}_{(d,p)}^i = [\gamma_{(d,p)}^{i1} \dots \gamma_{(d,p)}^{iN_r}]^T \in \mathbb{C}^{N_r \times 1} \quad (129)$$

$$\boldsymbol{\gamma}_{(d,p)} = [(\boldsymbol{\gamma}_{(d,p)}^1)^T \dots (\boldsymbol{\gamma}_{(d,p)}^{N_t})^T]^T \in \mathbb{C}^{N_t N_r \times 1} \quad (130)$$

²Note that vectors are in bold (e.g., $\boldsymbol{\gamma}_d^i$ and $\boldsymbol{\gamma}_d$) while scalars are not (e.g., γ_d^{ij}). This distinction can be difficult to see in print; in such cases, note that symbols are also distinguished by their sub/superscripts.

Finally, let $\mathbf{u} = [(\mathbf{u}^1)^T \dots (\mathbf{u}^{N_t})^T]^T \in \mathbb{C}^{N_t L \times 1}$.

Due to the independence of the receiver noise across transmitter channels, the conditional PDF of \mathbf{s} under \mathcal{H}_1 , $p_1(\mathbf{s} | \gamma_d, \gamma_p, \mathbf{u})$, factors according to

$$p_1(\mathbf{s} | \gamma_d, \gamma_p, \mathbf{u}) = \prod_{i=1}^{N_t} p_1^i(\mathbf{s}^i | \gamma_d^i, \gamma_p^i, \mathbf{u}^i) \quad (131)$$

where

$$p_1^i(\mathbf{s}^i | \gamma_d^i, \gamma_p^i, \mathbf{u}^i) = c_1 \exp \left\{ -\frac{1}{\sigma^2} \sum_{j=1}^{N_r} \|\mathbf{s}^{ij} - \mathbf{M}_1^{ij} \mathbf{u}^i\|^2 \right\} \quad (132)$$

and $\mathbf{M}_1^{ij} = \mathbf{M}_d^{ij} + \mathbf{M}_p^{ij}$. The PDF of \mathbf{s} under \mathcal{H}_0 , $p_0(\mathbf{s} | \gamma_d, \mathbf{u})$, is defined similarly.

In this formulation, the transmit signals \mathbf{u} and channel coefficients γ_d and γ_p are considered deterministic and unknown. Thus, hypothesis \mathcal{H}_1 is composite because the PDF of \mathbf{s} in (131) is parameterized by γ_d , γ_p , and \mathbf{u} . Hypothesis \mathcal{H}_0 is also composite, parameterized by γ_d and \mathbf{u} . Therefore, the GLRT is derived, which replaces these unknowns with their MLEs in the likelihood ratio test [49]. Let $l_1(\gamma_d, \gamma_p, \mathbf{u} | \mathbf{s}) = \log p_1(\mathbf{s} | \gamma_d, \gamma_p, \mathbf{u})$ and $l_0(\gamma_d, \mathbf{u} | \mathbf{s}) = \log p_0(\mathbf{s} | \gamma_d, \mathbf{u})$ denote the log-likelihood functions under \mathcal{H}_1 and \mathcal{H}_0 . Then, the GLRT may be written as

$$\max_{\{\gamma_d, \gamma_p, \mathbf{u}\}} l_1(\gamma_d, \gamma_p, \mathbf{u} | \mathbf{s}) - \max_{\{\gamma_d, \mathbf{u}\}} l_0(\gamma_d, \mathbf{u} | \mathbf{s}) \underset{\mathcal{H}_0}{\overset{\mathcal{H}_1}{\gtrless}} \kappa_{rs} \quad (133)$$

Consider the log-likelihood $l_1(\gamma_d, \gamma_p, \mathbf{u} | \mathbf{s})$. From (131),

$$l_1(\gamma_d, \gamma_p, \mathbf{u} | \mathbf{s}) = \sum_{i=1}^{N_t} l_1^i(\gamma_d^i, \gamma_p^i, \mathbf{u}^i | \mathbf{s}^i) \quad (134)$$

where, from (132) and ignoring an additive constant,

$$l_1^i(\gamma_d^i, \gamma_p^i, \mathbf{u}^i | \mathbf{s}^i) = -\frac{1}{\sigma^2} \sum_{j=1}^{N_r} \|\mathbf{s}^{ij} - \mathbf{M}_1^{ij} \mathbf{u}^i\|^2 \quad (135)$$

It is shown in Appendix B that

$$\|\mathbf{s}^{ij} - \mathbf{M}_1^{ij} \mathbf{u}^i\|^2 \approx \|\tilde{\mathbf{s}}_s^{ij} - \mu_s^{ij} \mathbf{u}^i\|^2 + \|\tilde{\mathbf{s}}_r^{ij} - \mu_r^{ij} \mathbf{u}^i\|^2 + E_{(rs)^\perp}^{ij} \quad (136)$$

where $\tilde{\mathbf{s}}_r^{ij} = (\mathcal{D}_d^{ij})^H \mathbf{s}_r^{ij}$ and $\tilde{\mathbf{s}}_s^{ij} = (\mathcal{D}_p^{ij})^H \mathbf{s}_s^{ij}$ are delay-Doppler compensated reference and surveillance signals defined by (241) and (243), μ_r^{ij} and μ_s^{ij} are complex scalars defined in (246) and (247) that account for the composite scaling of the reference and surveillance channels, and $E_{(rs)^\perp}^{ij}$ represents the energy of \mathbf{s}^{ij} not captured by $\tilde{\mathbf{s}}_r^{ij}$ and $\tilde{\mathbf{s}}_s^{ij}$, defined in (230). Note that μ_r^{ij} and μ_s^{ij} are defined in terms of γ_d^{ij} and γ_p^{ij} , respectively. Thus, they may also be regarded as deterministic unknowns, and they replace γ_d^{ij} and γ_p^{ij} in the following development. Accordingly, let $\boldsymbol{\mu}_{(r,s)}^i$ and $\boldsymbol{\mu}_{(r,s)}$ be defined as

$$\boldsymbol{\mu}_{(r,s)}^i = [\mu_{(r,s)}^{i1} \cdots \mu_{(r,s)}^{iN_r}]^T \in \mathbb{C}^{N_r \times 1} \quad (137)$$

$$\boldsymbol{\mu}_{(r,s)} = [(\boldsymbol{\mu}_{(r,s)}^1)^T \cdots (\boldsymbol{\mu}_{(r,s)}^{N_t})^T]^T \in \mathbb{C}^{N_t N_r \times 1} \quad (138)$$

where $(\cdot)_{(r,s)}$ denotes either $(\cdot)_r$ or $(\cdot)_s$. Using (136) in (135),

$$l_1^i(\boldsymbol{\mu}_r^i, \boldsymbol{\mu}_s^i, \mathbf{u}^i | \mathbf{s}^i) \approx -\frac{1}{\sigma^2} \sum_{j=1}^{N_r} \left(\|\tilde{\mathbf{s}}_s^{ij} - \mu_s^{ij} \mathbf{u}^i\|^2 + \|\tilde{\mathbf{s}}_r^{ij} - \mu_r^{ij} \mathbf{u}^i\|^2 + E_{(rs)^\perp}^{ij} \right) \quad (139)$$

The MLE of $\mu_{(r,s)}^{ij}$ is given from (139) by

$$\hat{\mu}_{(r,s)}^{ij} = \frac{(\mathbf{u}^i)^H \tilde{\mathbf{s}}_{(r,s)}^{ij}}{\|\mathbf{u}^i\|^2} \quad (140)$$

Substituting (140) into (139), and simplifying, gives

$$l_1^i(\hat{\boldsymbol{\mu}}_r^i, \hat{\boldsymbol{\mu}}_s^i, \mathbf{u}^i | \mathbf{s}^i) = -\frac{1}{\sigma^2} \left(E^i - \frac{\mathbf{u}^{iH} \Phi_1^i \Phi_1^{iH} \mathbf{u}^i}{\|\mathbf{u}^i\|^2} \right) \quad (141)$$

where $\Phi_1^i = [\Phi_s^i \ \Phi_r^i]$, the matrices Φ_s^i and Φ_r^i are defined as

$$\Phi_{(r,s)}^i = [\tilde{\mathbf{s}}_{(r,s)}^{i1}, \dots, \tilde{\mathbf{s}}_{(r,s)}^{iN_r}] \in \mathbb{C}^{L \times N_r} \quad (142)$$

the scalar $E^i = \sum_j \|\mathbf{s}^{ij}\|^2$ denotes the cumulative energy of the measurements associated with the i th transmitter, and

$$\|\mathbf{s}^{ij}\|^2 = \|\tilde{\mathbf{s}}_r^{ij}\|^2 + \|\tilde{\mathbf{s}}_s^{ij}\|^2 + E_{(rs)^\perp}^{ij} \quad (143)$$

Let $\lambda_1(\cdot)$ denote the largest eigenvalue of its matrix argument, and let $\mathbf{v}_1(\cdot)$ denote the associated eigenvector. Then, the Rayleigh quotient in (141) achieves its maximum value, $\lambda_1(\Phi_1^i \Phi_1^{iH})$, when $\mathbf{u}^i = \mathbf{v}_1(\Phi_1^i \Phi_1^{iH})$ [44, p. 176]. Therefore, $\hat{\mathbf{u}}^i = \mathbf{v}_1(\Phi_1^i \Phi_1^{iH})$, and (141) becomes

$$l_1^i(\hat{\boldsymbol{\mu}}_r^i, \hat{\boldsymbol{\mu}}_s^i, \hat{\mathbf{u}}^i | \mathbf{s}^i) = -\frac{1}{\sigma^2} \left(E^i - \lambda_1(\Phi_1^i \Phi_1^{iH}) \right) \quad (144)$$

Noting that $\lambda_1(\Phi_1^i \Phi_1^{iH}) = \lambda_1(\Phi_1^{iH} \Phi_1^i)$, and that typically $2N_r \ll L$, it is more efficient to consider the *Gram matrix* $\mathbf{G}_1^i = (\Phi_1^i)^H \Phi_1^i \in \mathbb{C}^{2N_r \times 2N_r}$, giving

$$l_1^i(\hat{\boldsymbol{\mu}}_r^i, \hat{\boldsymbol{\mu}}_s^i, \hat{\mathbf{u}}^i | \mathbf{s}^i) = -\frac{1}{\sigma^2} \left(E^i - \lambda_1(\mathbf{G}_1^i) \right) \quad (145)$$

Therefore, using (134) and (145),

$$l_1(\hat{\boldsymbol{\mu}}_r, \hat{\boldsymbol{\mu}}_s, \hat{\mathbf{u}} | \mathbf{s}) = -\frac{1}{\sigma^2} \sum_{i=1}^{N_t} \left(E^i - \lambda_1(\mathbf{G}_1^i) \right) \quad (146)$$

By a similar procedure, it can be shown under \mathcal{H}_0 that

$$l_0(\hat{\boldsymbol{\mu}}_r, \hat{\mathbf{u}} | \mathbf{s}) = -\frac{1}{\sigma^2} \sum_{i=1}^{N_t} \left(E^i - \lambda_1(\mathbf{G}_{rr}^i) \right) \quad (147)$$

where $\mathbf{G}_{rr}^i = (\Phi_r^i)^H \Phi_r^i \in \mathbb{C}^{N_r \times N_r}$. Using (146) and (147), the RS-GLRT results from (133) as

$$\xi_{rs} = \frac{1}{\sigma^2} \sum_{i=1}^{N_t} \left(\lambda_1(\mathbf{G}_1^i) - \lambda_1(\mathbf{G}_{rr}^i) \right) \underset{\mathcal{H}_0}{\overset{\mathcal{H}_1}{\geq}} \kappa_{rs} \quad (148)$$

4.2.2 Surveillance-Surveillance GLRT.

Alternatively, a PMR system may use only the target-path signals for target detection. The resulting detector is a special case of the RS-GLRT in (148) when only surveillance channels are formed at each receiver, i.e., $\tilde{\mathbf{s}}_r^{ij} = \mathbf{0}$ for all i and j ,

$$\xi_{ss} = \frac{1}{\sigma^2} \sum_{i=1}^{N_t} \lambda_1(\mathbf{G}_{ss}^i) \underset{\mathcal{H}_0}{\overset{\mathcal{H}_1}{\geq}} \kappa_{ss} \quad (149)$$

where $\mathbf{G}_{ss}^i = (\Phi_s^i)^H \Phi_s^i$. This is the SS-GLRT detector discussed previously in Chapter III, where it was shown that PMR detection in the absence of direct-path signals is equivalent to PSL detection, as the target in PMR can be interpreted as “emitting” the scattered target-path signals [40].

4.2.3 Matched Filter GLRT.

For comparison, the detector that results when the transmit signals \mathbf{u} are assumed known, termed the matched filter GLRT (MF-GLRT), is also considered. It can be derived by following the RS-GLRT derivation through (141) under \mathcal{H}_1 , and performing the analogous steps under \mathcal{H}_0 , resulting in

$$\xi_{mf} = \frac{1}{\sigma^2} \sum_{i=1}^{N_t} \sum_{j=1}^{N_r} |(\mathbf{u}^i)^H \tilde{\mathbf{s}}_s^{ij}|^2 \underset{\mathcal{H}_0}{\overset{\mathcal{H}_1}{\geq}} \kappa_{mf} \quad (150)$$

Assuming \mathbf{u} is known represents an AMR scenario. Note that ξ_{mf} is formed by delay-Doppler compensating the surveillance signals, matched filtering each bistatic pair, and non-coherently integrating. This structure is common in AMR detection [24, 43].

4.3 Distributions

This section presents PDFs for ξ_{mf} and ξ_{rs} under \mathcal{H}_1 and \mathcal{H}_0 ³. The development considers the presence or absence of a target within the cell under test $(\mathbf{p}, \hat{\mathbf{p}})$. Under this condition, the surveillance signal $\tilde{\mathbf{s}}_s^{ij}$ in (243) reduces to

$$\tilde{\mathbf{s}}_s^{ij} = b_1 \mu_s^{ij} \mathbf{u}^i + \tilde{\mathbf{n}}_s^{ij} \quad (151)$$

where $\tilde{\mathbf{n}}_s^{ij}$ is distributed as $\mathcal{CN}(\mathbf{0}_L, \sigma^2 \mathbf{I}_L)$, $b_1 = 1$ under \mathcal{H}_1 , and $b_1 = 0$ under \mathcal{H}_0 . Consequently, $\tilde{\mathbf{s}}_s^{ij}$ is distributed as

$$\tilde{\mathbf{s}}_s^{ij} \sim \mathcal{CN}(b_1 \mu_s^{ij} \mathbf{u}^i, \sigma^2 \mathbf{I}_L) \quad (152)$$

Similarly, $\tilde{\mathbf{s}}_r^{ij} \sim \mathcal{CN}(\mu_r^{ij} \mathbf{u}^i, \sigma^2 \mathbf{I}_L)$ under both hypotheses.

4.3.1 Matched Filter GLRT Distributions.

First, consider the MF-GLRT statistic ξ_{mf} in (150). From (152), the inner product $(\mathbf{u}^i)^H \tilde{\mathbf{s}}_s^{ij}$ is distributed as $\mathcal{CN}(b_1 \mu_s^{ij} L, \sigma^2 L)$, and the statistic ξ_{mf} can be written as

$$\xi_{mf} = \left(\frac{L}{2} \right) \chi_{(2N_t N_r), \zeta_{mf}}^2 \quad (153)$$

where $\chi_{(k), \zeta}^2$ is a non-central chi-squared random variable with k degrees of freedom and non-centrality parameter ζ , and

$$\zeta_{mf} = \frac{2}{\sigma^2 L} \sum_{i=1}^{N_t} \sum_{j=1}^{N_r} |b_1 \mu_s^{ij} L|^2 \quad (154)$$

$$= 2 b_1 L N_r \sum_{i=1}^{N_t} \text{SNR}_{\text{avg}}^i \quad (155)$$

³Note that PDFs for ξ_{ss} have already been presented under \mathcal{H}_1 and \mathcal{H}_0 in Sec. 3.3.

where $\text{SNR}_{\text{avg}}^i = \|\boldsymbol{\mu}_s^i\|^2/(N_r\sigma^2)$ is the average input target-path SNR associated with the i th transmitter after surveillance channel formation. Consequently, the PDF of ξ_{mf} , denoted $p_{mf}(\xi)$, is given by

$$p_{mf}(\xi) = \left(\frac{2}{L}\right) f_{\chi^2}\left(\frac{2\xi}{L}; 2N_tN_r, \zeta_{mf}\right) \quad (156)$$

where $f_{\chi^2}(x; k, \zeta)$ is the PDF of $\chi_{(k),\zeta}^2$, i.e.,

$$f_{\chi^2}(x; k, \zeta) = \frac{1}{2} e^{-(x+\zeta)/2} \left(\frac{x}{\zeta}\right)^{(k-2)/4} I_{k/2-1}(\sqrt{\zeta x}) \quad (157)$$

and $I_\nu(z)$ is the modified Bessel function of the first kind of order ν . Note that $\zeta_{mf} = 0$ under \mathcal{H}_0 , and (157) reduces to the central chi-squared distribution with k degrees of freedom.

4.3.2 Reference-Surveillance GLRT Distributions.

Next, consider the RS-GLRT statistic ξ_{rs} in (148). The Gram matrix \mathbf{G}_{rr}^i follows the non-central uncorrelated complex Wishart distribution under both \mathcal{H}_1 and \mathcal{H}_0 . In particular, $\mathbf{G}_{rr}^i \sim \mathbf{W}_{N_r}(L, \boldsymbol{\Sigma}_{rr}^i, \boldsymbol{\Omega}_{rr}^i)$, where $\boldsymbol{\Sigma}_{rr}^i = \sigma^2 \mathbf{I}_{N_r}$ and $\boldsymbol{\Omega}_{rr}^i$ is a rank-1 non-centrality matrix with non-zero eigenvalue ζ_{rr}^i given by

$$\zeta_{rr}^i = \frac{L\|\boldsymbol{\mu}_r^i\|^2}{\sigma^2} = LN_r \text{DNR}_{\text{avg}}^i \quad (158)$$

and $\text{DNR}_{\text{avg}}^i = \|\boldsymbol{\mu}_r^i\|^2/(N_r\sigma^2)$ is the average input direct-path SNR associated with the i th transmitter after reference channel formation. This distribution is unchanged between hypotheses because the Gram matrix \mathbf{G}_{rr}^i depends only on the direct-path signals. The Gram matrix \mathbf{G}_1^i also follows the non-central uncorrelated complex Wishart distribution under both hypotheses, i.e., $\mathbf{G}_1^i \sim \mathbf{W}_{2N_r}(L, \boldsymbol{\Sigma}_1^i, \boldsymbol{\Omega}_1^i)$, where $\boldsymbol{\Sigma}_1^i =$

$\sigma^2 \mathbf{I}_{2N_r}$ and $\mathbf{\Omega}_1^i$ is a rank-1 non-centrality matrix with a non-zero eigenvalue ζ_1^i that varies between hypotheses as

$$\zeta_1^i = \begin{cases} LN_r(\text{DNR}_{\text{avg}}^i + \text{SNR}_{\text{avg}}^i) & \text{under } \mathcal{H}_1 \\ LN_r \text{ DNR}_{\text{avg}}^i & \text{under } \mathcal{H}_0 \end{cases} \quad (159)$$

Therefore, the individual PDFs of $\lambda_1(\mathbf{G}_{rr}^i)$ and $\lambda_1(\mathbf{G}_1^i)$ may be found using the result in [48]. However, $\lambda_1(\mathbf{G}_1^i)$ and $\lambda_1(\mathbf{G}_{rr}^i)$ are not independent because \mathbf{G}_{rr}^i is a diagonal block of \mathbf{G}_1^i . The joint distribution of the eigenvalues of a complex Wishart matrix and the eigenvalues of its diagonal blocks does not appear to exist, precluding determination of the exact distribution of ξ_{rs} for now.

Nonetheless, it is now shown that ξ_{rs} approximates ξ_{mf} within a scalar constant assuming high-DNR, i.e., $\text{DNR}_{\text{avg}}^i \gg 1 \forall i$, and assuming a high average power ratio $\bar{\rho}^i$ between the direct-path and target-path signals, i.e., $\bar{\rho}^i = \|\boldsymbol{\mu}_r^i\|^2 / \|\boldsymbol{\mu}_s^i\|^2 \gg 1 \forall i$. Let $\lambda_n(\cdot)$ denote the n th largest eigenvalue of its matrix argument. Under high-DNR, \mathbf{G}_1^i is approximately rank-1, i.e., $\lambda_1(\mathbf{G}_1^i) / \lambda_j(\mathbf{G}_1^i) \gg 1$ for $2 \leq j \leq 2N_r$. Consequently,

$$\lambda_1(\mathbf{G}_1^i) \approx \sqrt{\lambda_1^2(\mathbf{G}_1^i) + \dots + \lambda_{2N_r}^2(\mathbf{G}_1^i)} = \|\mathbf{G}_1^i\|_F \quad (160)$$

where $\|\cdot\|_F$ denotes the Frobenius norm of its matrix argument. Note that \mathbf{G}_1^i can be partitioned into four blocks,

$$\mathbf{G}_1^i = \begin{bmatrix} \Phi_s^{iH} \Phi_s^i & \Phi_s^{iH} \Phi_r^i \\ \Phi_r^{iH} \Phi_s^i & \Phi_r^{iH} \Phi_r^i \end{bmatrix} \triangleq \begin{bmatrix} \mathbf{G}_{ss}^i & \mathbf{G}_{sr}^i \\ \mathbf{G}_{rs}^i & \mathbf{G}_{rr}^i \end{bmatrix} \quad (161)$$

where $(\mathbf{G}_{rs}^i)^H = \mathbf{G}_{sr}^i$. Accordingly,

$$\|\mathbf{G}_1^i\|_F = \sqrt{\|\mathbf{G}_{ss}^i\|_F^2 + 2\|\mathbf{G}_{rs}^i\|_F^2 + \|\mathbf{G}_{rr}^i\|_F^2} \quad (162)$$

Let $F_{ss}^i = \|\mathbf{G}_{ss}^i\|_F$, $F_{rs}^i = \|\mathbf{G}_{rs}^i\|_F$, and $F_{rr}^i = \|\mathbf{G}_{rr}^i\|_F$. Then, letting $\tilde{F}_{rs}^i = F_{rs}^i/F_{rr}^i$,

$$\|\mathbf{G}_1^i\|_F = F_{rr}^i \sqrt{1 + \frac{F_{ss}^{i2} + 2F_{rs}^{i2}}{F_{rr}^{i2}}} \quad (163)$$

$$\approx F_{rr}^i \sqrt{1 + 2\tilde{F}_{rs}^{i2}} \quad (164)$$

$$= F_{rr}^i \left(1 + \tilde{F}_{rs}^{i2} + \mathcal{O}(\tilde{F}_{rs}^{i4})\right) \quad (165)$$

$$\approx F_{rr}^i (1 + \tilde{F}_{rs}^{i2}) \quad (166)$$

The approximation in (164) results because $2F_{rs}^{i2} \gg F_{ss}^{i2}$ under the high- $\bar{\rho}^i$ condition. Eq. 165 results from applying the Taylor series expansion for $\sqrt{1+x}$ around $x=0$, $\sqrt{1+x} = 1 + x/2 + \mathcal{O}(x^2)$, which converges for $|x| < 1$. Note that $2F_{rs}^{i2} \ll F_{rr}^{i2}$ under the high- $\bar{\rho}^i$ condition, which justifies the approximation in (166).

Similarly, the matrix \mathbf{G}_{rr}^i is also approximately rank-1 under the high-DNR condition. Consequently,

$$\lambda_1(\mathbf{G}_{rr}^i) \approx F_{rr}^i \quad (167)$$

Therefore, using (166) and (167),

$$\xi_{rs} \approx \frac{1}{\sigma^2} \sum_{i=1}^{N_t} \frac{F_{rs}^{i2}}{F_{rr}^i} \quad (168)$$

Furthermore, ignoring the noise in $\tilde{\mathbf{s}}_r^{ij}$ due to the high-DNR condition, i.e., $\tilde{\mathbf{s}}_r^{ij} \approx \mu_r^{ij} \mathbf{u}^i$, F_{rs}^{i2} may be expanded as

$$F_{rs}^{i2} = \sum_{j=1}^{N_r} \sum_{k=1}^{N_r} |\tilde{\mathbf{s}}_r^{ijH} \tilde{\mathbf{s}}_s^{ik}|^2 \quad (169)$$

$$\approx \|\boldsymbol{\mu}_r^i\|^2 \sum_{k=1}^{N_r} |\mathbf{u}^{iH} \tilde{\mathbf{s}}_s^{ik}|^2 \quad (170)$$

Similarly,

$$F_{rr}^i \approx L \|\boldsymbol{\mu}_r^i\|^2 \quad (171)$$

Using (170) and (171) in (168),

$$\xi_{rs} \approx \frac{1}{\sigma^2} \sum_{i=1}^{N_t} \sum_{k=1}^{N_r} \frac{|\mathbf{u}^{iH} \tilde{\mathbf{s}}_s^{ik}|^2}{L} \quad (172)$$

$$= \left(\frac{1}{L}\right) \xi_{mf} \quad (173)$$

Consequently, ξ_{rs} can be approximated as

$$\xi_{rs} \approx \left(\frac{1}{2}\right) \chi_{(2N_t N_r), \zeta_{mf}}^2 \quad (174)$$

and its distribution is $p_{rs}(\xi) = 2f_{\chi^2}(2\xi; 2N_t N_r, \zeta_{mf})$. Since detection performance is unaffected by scaling of the test statistic (provided the detection threshold is similarly scaled), the RS-GLRT detector is equivalent to the MF-GLRT detector under the high-DNR and high- $\bar{\rho}^i$ conditions.

The validity of (174) is verified in Fig. 26, which compares normalized histograms generated from 10^5 simulated realizations of ξ_{rs} and the associated predicted PDFs according to (174) under both hypotheses. The simulation involves a scenario with 2 transmitters, 3 receivers, and $L = 1000$ samples per transmit signal. The channel scale factors μ_r^{ij} and μ_s^{ij} were selected randomly and scaled to achieve $\text{SNR}_{\text{avg}}^i = -20$ dB and $\text{DNR}_{\text{avg}}^i = +20$ dB for all i , assuming $\sigma^2 = 10^{-6}$, such that $\bar{\rho}^i = +40$ dB. As shown, the predicted PDFs closely match the empirical results.

4.3.3 Dependence on SNR and DNR.

It is worth noting that all the presented PDFs depend only on $\text{SNR}_{\text{avg}}^i$, $\text{DNR}_{\text{avg}}^i$, N_t , and N_r . This is seen by examining the non-centrality parameter ζ_{mf} in (155) and

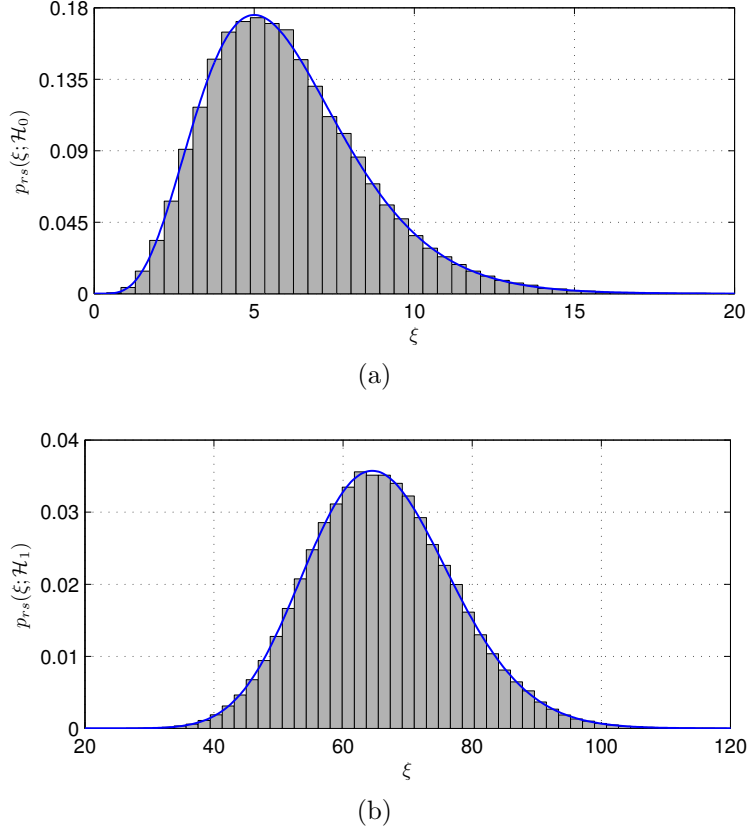


Figure 26. Empirical and Predicted PDFs for ξ_{rs} Under (a) \mathcal{H}_0 and (b) \mathcal{H}_1

the complex Wishart non-centrality matrix eigenvalues ζ_{ss}^i , ζ_{rr}^i , and ζ_1^i in (87), (158), and (159), respectively, all of which are functions of $LN_r \text{SNR}_{\text{avg}}^i$ and/or $LN_r \text{DNR}_{\text{avg}}^i$. The dependence on N_t is seen in the non-centrality parameter ζ_{mf} in (155) and by the convolution over N_t PDFs in (83). Consequently, detection performance does not depend on the specific structure of the transmit waveforms or on the specific values of the target-path and direct-path SNRs across receivers. Rather, it depends only on the transmit waveform energy $\|\mathbf{u}^i\|^2 = L$ and the average target-path and direct-path SNRs across receivers. Note that the LN_r factor may be interpreted as signal processing gain resulting from coherent integration in time and across receiver channels. In addition, detection performance is expected to increase monotonically in $LN_r \text{SNR}_{\text{avg}}^i$. This is demonstrated by the empirical results presented in Sec. 4.5.

4.4 Interpretations

This section discusses the relationship between the statistics ξ_{rs} , ξ_{ss} , and ξ_{mf} . In particular, the Gram matrix \mathbf{G}_1^i in ξ_{rs} is examined, and it is shown that calculation of its block matrices \mathbf{G}_{ss}^i and \mathbf{G}_{sr}^i entails operations that are characteristic of PSL and AMR, respectively. The following discussion distinguishes between the true target state $(\mathbf{t}, \dot{\mathbf{t}})$ and the hypothesized cell under test $(\mathbf{p}, \dot{\mathbf{p}})$. If there is a mismatch between \mathbf{t} and \mathbf{p} , then the target angle-of-arrival is possibly mismatched to the hypothesized angle-of-arrival, resulting in a mismatch loss. Using (231), it can be shown that the surveillance signal following beamforming, \mathbf{s}_s^{ij} , is given by

$$\mathbf{s}_s^{ij} = \tilde{\mu}_s^{ij} \mathcal{D}_t^{ij} \mathbf{u}^i + \mathbf{n}_s^{ij} \quad (175)$$

where $\tilde{\mu}_s^{ij} = \zeta_p^{ij} \mu_s^{ij}$, and ζ_p^{ij} is the angular mismatch loss,

$$\zeta_p^{ij} = \frac{\beta_{pt}^{ij} - (\beta_{dp}^{ij})^* \beta_{dt}^{ij}}{1 - |\beta_{dp}^{ij}|^2} \quad (176)$$

and the scalars β_{pt}^{ij} , β_{dt}^{ij} and β_{dp}^{ij} are defined by

$$\beta_{pt}^{ij} = \frac{(\mathbf{a}_p^{ij})^H \mathbf{a}_t^{ij}}{N_e}, \quad \beta_{dt}^{ij} = \frac{(\mathbf{a}_d^{ij})^H \mathbf{a}_t^{ij}}{N_e}, \quad \beta_{dp}^{ij} = \frac{(\mathbf{a}_d^{ij})^H \mathbf{a}_p^{ij}}{N_e} \quad (177)$$

Note that $|\zeta_p^{ij}| \leq 1$, and $\zeta_p^{ij} = 1$ when $\mathbf{a}_p^{ij} = \mathbf{a}_t^{ij}$, i.e., when \mathbf{p} and \mathbf{t} are at the same angle with respect to the j th receiver.

4.4.1 Surveillance-Surveillance Processing.

Consider \mathbf{G}_{ss}^i , the upper-left block of \mathbf{G}_1^i in (161). The elements of this matrix consist of the pairwise inner products of the surveillance signals $\{\tilde{\mathbf{s}}_s^{ij} : j = 1 \dots N_r\}$.

Specifically, the jk th element of \mathbf{G}_{ss}^i may be expressed as

$$[\mathbf{G}_{ss}^i]_{jk} = \tilde{\mathbf{s}}_s^{ijH} \tilde{\mathbf{s}}_s^{ik} \quad (178)$$

$$= \mathbf{s}_s^{ijH} \mathcal{D}_p^{ij} \mathcal{D}_p^{ikH} \mathbf{s}_s^{ik} \quad (179)$$

$$= \mathbf{s}_s^{ijH} \mathcal{D}(\ell_p^{ij}, \nu_p^{ij}) \mathcal{D}^H(\ell_p^{ik}, \nu_p^{ik}) \mathbf{s}_s^{ik} \quad (180)$$

$$= \mathbf{s}_s^{ijH} \mathcal{D}(\underbrace{\ell_p^{ij} - \ell_p^{ik}}_{\triangleq \Delta \ell_p^{i,jk}}, \underbrace{\nu_p^{ij} - \nu_p^{ik}}_{\triangleq \Delta \nu_p^{i,jk}}) \mathbf{s}_s^{ik} \quad (181)$$

$$= \chi_{ss}^{i,jk}(\Delta \ell_p^{i,jk}, \Delta \nu_p^{i,jk}) \quad (182)$$

where $\chi_{ss}^{i,jk}(\Delta \ell, \Delta \nu)$ is the CAF between the i th surveillance channels of the j th and k th receivers, defined as

$$\chi_{ss}^{i,jk}(\Delta \ell, \Delta \nu) = \sum_{l=0}^{L-1} [\mathbf{s}_s^{ik}]_l [\mathbf{s}_s^{ij}]_{l+\Delta \ell}^* e^{j\Delta \nu l} \quad (183)$$

$\Delta \ell_p^{i,jk}$ is the hypothesized TDOA at the j th and k th receivers, and $\Delta \nu_p^{i,jk}$ is the corresponding hypothesized FDOA. Thus, the elements of \mathbf{G}_{ss}^i may be interpreted as samples of the pairwise surveillance-surveillance CAFs. This is termed *surveillance-surveillance processing*.

The elements of \mathbf{G}_{ss}^i may also be expressed in terms of the ambiguity function (AF) of the i th transmit signal \mathbf{u}^i . Substituting (175) for $\tilde{\mathbf{s}}_s^{ij}$ and $\tilde{\mathbf{s}}_s^{ik}$ in (181), and ignoring receiver noise, $[\mathbf{G}_{ss}^i]_{jk}$ may be expressed as

$$[\mathbf{G}_{ss}^i]_{jk} = \mathbf{s}_s^{ijH} \mathcal{D}(\Delta \ell_p^{i,jk}, \Delta \nu_p^{i,jk}) \mathbf{s}_s^{ik} \quad (184)$$

$$= (\tilde{\mu}_s^{ij} \mathcal{D}_t^{ij} \mathbf{u}^i)^H \mathcal{D}(\Delta \ell_p^{i,jk}, \Delta \nu_p^{i,jk}) (\tilde{\mu}_s^{ik} \mathcal{D}_t^{ik} \mathbf{u}^i) \quad (185)$$

$$= \tilde{\mu}_s^{ij*} \tilde{\mu}_s^{ik} \mathbf{u}^{iH} \mathcal{D}^H(\Delta \ell_t^{i,jk}, \Delta \nu_t^{i,jk}) \mathcal{D}(\Delta \ell_p^{i,jk}, \Delta \nu_p^{i,jk}) \mathbf{u}^i \quad (186)$$

$$= \tilde{\mu}_s^{ij*} \tilde{\mu}_s^{ik} \chi^i(\Delta \ell_p^{i,jk} - \Delta \ell_t^{i,jk}, \Delta \nu_p^{i,jk} - \Delta \nu_t^{i,jk}) \quad (187)$$

where $\chi^i(\Delta\ell, \Delta\nu)$ is the AF of \mathbf{u}^i , defined as

$$\chi^i(\Delta\ell, \Delta\nu) \triangleq \sum_{l=0}^{L-1} [\mathbf{u}^i]_l [\mathbf{u}^i]_{l+\Delta\ell}^* e^{j\Delta\nu l} \quad (188)$$

Noting that $\chi^i(\Delta\ell, \Delta\nu)$ peaks when its arguments are zero leads to the following iso-range and iso-Doppler conditions:

$$\Delta\ell_p^{i,jk} = \Delta\ell_t^{i,jk} \quad (189)$$

$$\Delta\nu_p^{i,jk} = \Delta\nu_t^{i,jk} \quad (190)$$

In words, $[\mathbf{G}_{ss}^i]_{jk}$ peaks when (a) the hypothesized TDOA equals the actual target TDOA and (b) the hypothesized FDOA equals the actual target FDOA. This is representative of PSL sensor networks, which localize targets along contours of constant TDOA and FDOA [16, 86].

4.4.2 Reference-Surveillance Processing.

Next, consider \mathbf{G}_{sr}^i , the upper-right block of \mathbf{G}_1^i in (161). The elements of this matrix consist of the pairwise inner products of the surveillance signals $\{\tilde{\mathbf{s}}_s^{ij} : j = 1 \dots N_r\}$ with the reference signals $\{\tilde{\mathbf{s}}_r^{ij} : j = 1 \dots N_r\}$. It can similarly be shown that the elements of \mathbf{G}_{sr}^i can be expressed as

$$[\mathbf{G}_{sr}^i]_{jk} = \tilde{\mathbf{s}}_s^{ijH} \tilde{\mathbf{s}}_r^{ik} \quad (191)$$

$$= \mathbf{s}_s^{ijH} \mathcal{D}_p^{ij} \mathcal{D}_d^{ikH} \mathbf{s}_r^{ik} \quad (192)$$

$$= \mathbf{s}_s^{ijH} \mathcal{D}(\ell_p^{ij}, \nu_p^{ij}) \mathcal{D}^H(\ell_d^{ik}, \nu_d^{ik}) \mathbf{s}_r^{ik} \quad (193)$$

$$= \mathbf{s}_s^{ijH} \mathcal{D}(\ell_p^{ij} - \ell_d^{ik}, \nu_p^{ij} - \nu_d^{ik}) \mathbf{s}_r^{ik} \quad (194)$$

$$= \chi_{sr}^{i,jk}(\Delta\ell_{pd}^{i,jk}, \Delta\nu_{pd}^{i,jk}) \quad (195)$$

where $\Delta\ell_{pd}^{i,jk} = \ell_p^{ij} - \ell_d^{ik}$ is relative delay, defined as the difference between the hypothesized bistatic delay ℓ_p^{ij} and the direct-path delay ℓ_d^{ik} , $\Delta\nu_{pd}^{i,jk} = \nu_p^{ij} - \nu_d^{ik}$ is relative Doppler, defined as the difference between the hypothesized bistatic Doppler ν_p^{ij} and the direct-path Doppler ν_d^{ik} , and $\chi_{sr}^{i,jk}(\Delta\ell, \Delta\nu)$ is the CAF between the i th surveillance channel of the j th receiver and the i th reference channel of the k th receiver, defined as

$$\chi_{sr}^{i,jk}(\Delta\ell, \Delta\nu) \triangleq \sum_{l=0}^{L-1} [\mathbf{s}_r^{ik}]_l [\mathbf{s}_s^{ij}]_{l+\Delta\ell}^* e^{j\Delta\nu l} \quad (196)$$

Thus, the elements of \mathbf{G}_{sr}^i may be interpreted as samples of the pairwise reference-surveillance CAFs. This is termed *reference-surveillance processing*.

Similarly, $[\mathbf{G}_{sr}^i]_{jk}$ may also be expressed (ignoring noise) as

$$[\mathbf{G}_{sr}^i]_{jk} = \mathbf{s}_s^{ijH} \mathcal{D}(\Delta\ell_{pd}^{i,jk}, \Delta\nu_{pd}^{i,jk}) \mathbf{s}_r^{ik} \quad (197)$$

$$= (\tilde{\mu}_s^{ij} \mathcal{D}_t^{ij} \mathbf{u}^i)^H \mathcal{D}(\Delta\ell_{pd}^{i,jk}, \Delta\nu_{pd}^{i,jk}) (\mu_r^{ik} \mathcal{D}_d^{ik} \mathbf{u}^i) \quad (198)$$

$$= \tilde{\mu}_s^{ij*} \mu_r^{ik} \chi^i(\ell_p^{ij} - \ell_t^{ij}, \nu_p^{ij} - \nu_t^{ij}) \quad (199)$$

Noting that $\chi^i(\Delta\ell, \Delta\nu)$ peaks when its arguments are zero leads to the following iso-range and iso-Doppler conditions:

$$\ell_p^{ij} = \ell_t^{ij} \quad (200)$$

$$\nu_p^{ij} = \nu_t^{ij} \quad (201)$$

In words, $[\mathbf{G}_{sr}^i]_{jk}$ peaks when (a) the hypothesized bistatic delay equals the actual target bistatic delay and (b) the hypothesized bistatic Doppler equals the actual target bistatic Doppler. This is representative of the processing associated with each bistatic pair in active multistatic and MIMO radar, which localize targets along contours of constant bistatic range and bistatic Doppler [64, 42].

4.5 Simulations

This section compares the detection and ambiguity performance of the RS-GLRT, SS-GLRT, and MF-GLRT detectors via numerical simulation. Discussion of the significance of these simulation results follows in Sec. 4.6.

4.5.1 Detection Performance.

This section illustrates how the detection performance of each GLRT varies with $\text{SNR}_{\text{avg}}^i$, $\text{DNR}_{\text{avg}}^i$, and L . Fig. 27 depicts probability of detection (P_d) curves as a function of $\text{SNR}_{\text{avg}}^i$ for a scenario with $N_t = 2$ transmitters, $N_r = 3$ receivers, and $L = 1000$ samples per signal. Each curve is generated empirically using 10^5 trials under \mathcal{H}_0 to determine the detection threshold that achieves a probability of false alarm (P_{fa}) of 10^{-3} . P_d is calculated under \mathcal{H}_1 using 10^4 trials for each value of $\text{SNR}_{\text{avg}}^i$. A separate RS-GLRT curve is calculated for each $\text{DNR}_{\text{avg}}^i$ as it is varied from -40 to +20 dB in 5 dB increments. For convenience, $\text{SNR}_{\text{avg}}^i$ and $\text{DNR}_{\text{avg}}^i$ are assumed to be equal across transmitters, i.e., $\text{SNR}_{\text{avg}}^i = \text{SNR}_{\text{avg}} \forall i$ and $\text{DNR}_{\text{avg}}^i = \text{DNR}_{\text{avg}} \forall i$. As shown in Fig. 27, the detection sensitivity of the RS-GLRT improves with increasing DNR_{avg} . Specifically, sensitivity asymptotes at low and high values of DNR_{avg} and improves monotonically with increasing DNR_{avg} at intermediate DNR_{avg} . This asymptotic sensitivity is slightly inferior to that of the SS-GLRT at low DNR_{avg} and equal to that of the MF-GLRT at high DNR_{avg} .

Another view of these results is shown in Fig. 28, which plots the RS-GLRT P_d as a function of SNR_{avg} and DNR_{avg} . $P_d = 0.5$ and $P_d = 0.9$ iso-contours are depicted as solid black lines. SNR_{avg} values at which the SS-GLRT and MF-GLRT achieve $P_d = 0.5$ and $P_d = 0.9$ are shown as vertical dash-dotted red (SS-GLRT) and dashed blue (RS-GLRT) lines. Lines of constant \bar{p} are also depicted. As shown, detection performance may be divided into three regions: a low- \bar{p} region; a high-DNR region;

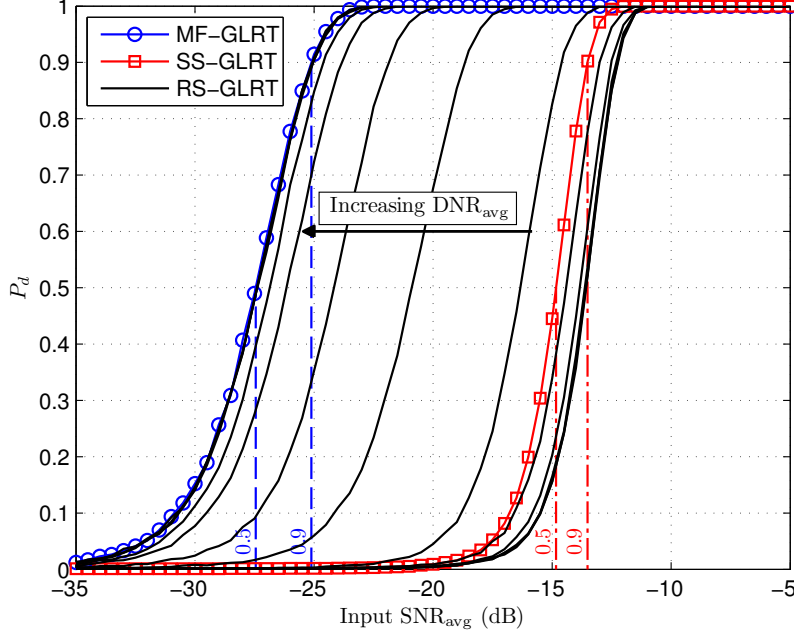


Figure 27. Probability of Detection Curves for $N_t = 2$, $N_r = 3$, and $L = 1000$

and a transition region. The low- $\bar{\rho}$ border is defined as the power ratio at which the SNR_{avg} of the RS-GLRT $P_d = 0.9$ iso-contour decreases one 1 dB below its asymptotic value. Similarly, the High-DNR border is defined as the value of DNR_{avg} at which the SNR_{avg} of the $P_d = 0.9$ iso-contour increases 1 dB above its asymptotic value.

The rationale for defining the region boundaries in this manner is seen by examining the effect of L on detection performance. Fig. 29 depicts $P_d = 0.9$ iso-contours for the three GLRTs over $L = [1, 3, 10, 30, 100, 300, 1000, 3000, 10000]$. As shown, the upper boundary occurs at approximately the same DNR_{avg} for all L ; the average for $L \geq 10$ at $\text{DNR}_{\text{avg}} = 1.21$ dB is depicted. Similarly, the lower boundary occurs at approximately the same $\bar{\rho}$ for all L ; the average for $L \geq 10$ at $\bar{\rho} = -4.51$ dB is depicted. Thus, the upper and lower region boundaries are defined in terms of a constant DNR_{avg} and constant $\bar{\rho}$, respectively. Note that the single-sample ($L = 1$) performance of all three GLRTs converges.

Fig. 29 shows that detection sensitivity improves with increasing L for every detec-

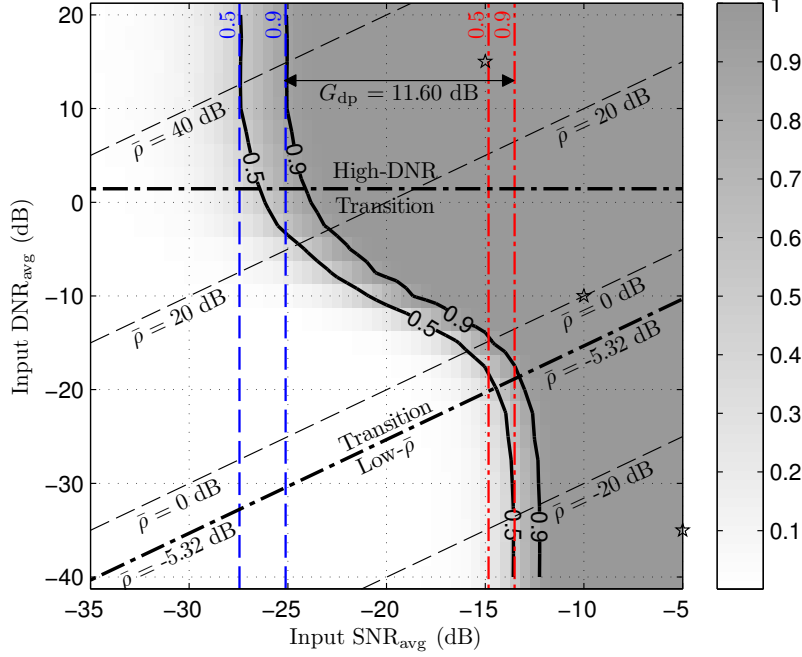


Figure 28. 2D View of RS-GLRT P_d for $N_t = 2$, $N_r = 3$, and $L = 1000$

tor, however the rate of sensitivity improvement with increasing L differs between detectors. This improvement may be quantified in terms of an integration gain $G_{\text{int}}(L)$, defined as the separation between the P_d curve for a given detector and length $L > 1$ and the P_d curve for that same detector with $L = 1$ at $P_d = 0.90$. For instance, the difference between the $L = 1$ and $L = 100$ curves at $P_d = 0.90$ for the MF-GLRT detector is 20 dB, indicating an integration gain of 20 dB. Fig. 30 shows G_{int} versus L for the MF-GLRT, SS-GLRT, and the RS-GLRT in both the high-DNR and low- $\bar{\rho}$ regions. As shown, the MF-GLRT exhibits an integration gain of $G_{\text{int}}(L) = L$, which reflects coherent integration. The SS-GLRT exhibits G_{int} that varies between $L^{0.7}$ at $L = 10$ (10 dB) to just below $L^{0.6}$ at $L = 10000$ (40 dB). This reflects non-coherent integration, and was discussed previously in Sec. 3.5.1.2. Finally, the RS-GLRT realizes an integration gain that is coherent in the high-DNR region and non-coherent in the low- $\bar{\rho}$ region. The significance of this result is discussed in Sec. 4.6.

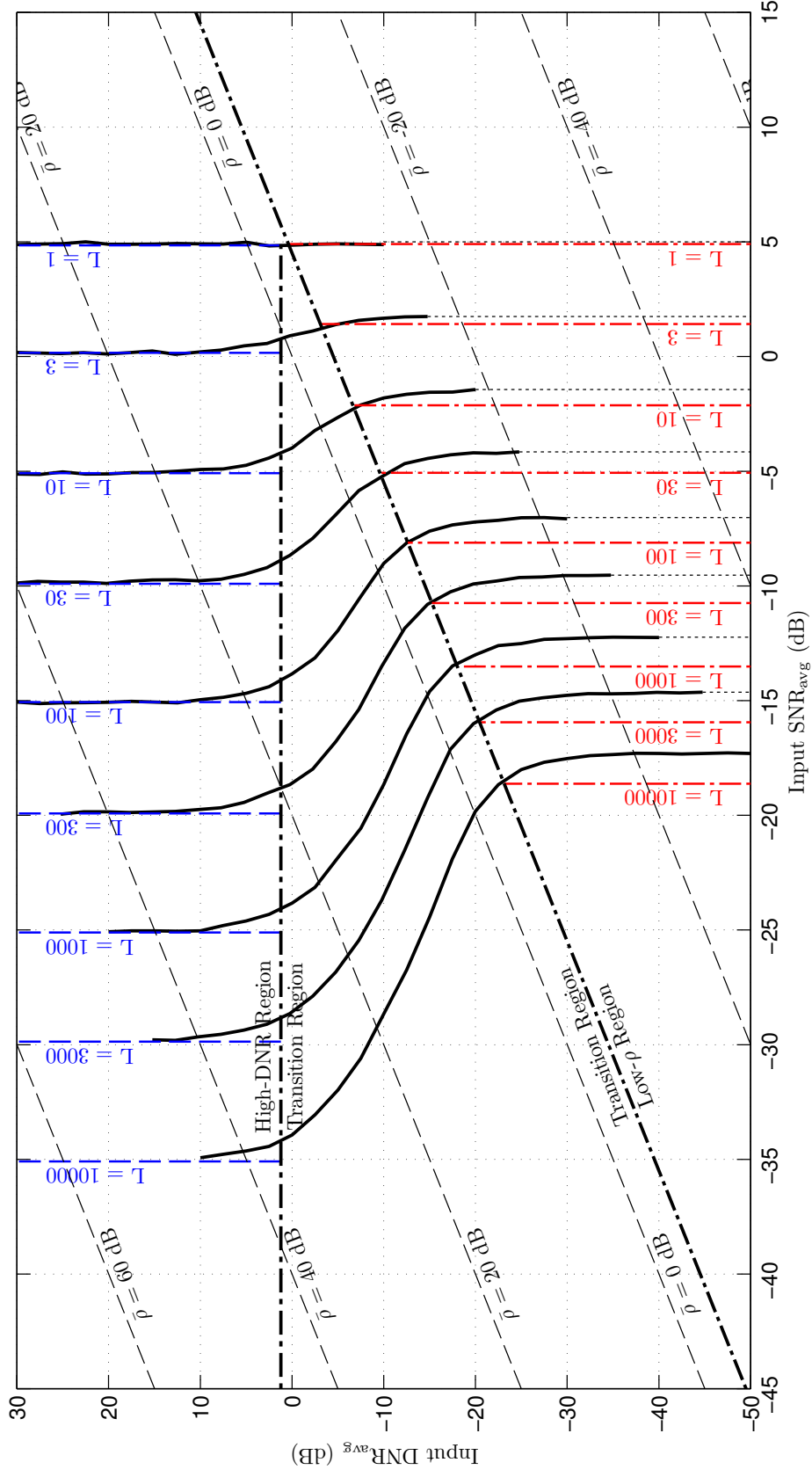


Figure 29. Depiction of RS-GLRT $P_d = 0.9$ iso-contours for $N_t = 2$, $N_r = 3$, and $L = [1, 3, 10, 30, 100, 300, 1000, 3000, 10000]$. The SNR_{avg} values at which the SS-GLRT and MF-GLRT achieve $P_d = 0.9$ are depicted by dash-dotted red lines and dashed blue lines, respectively, for each L .

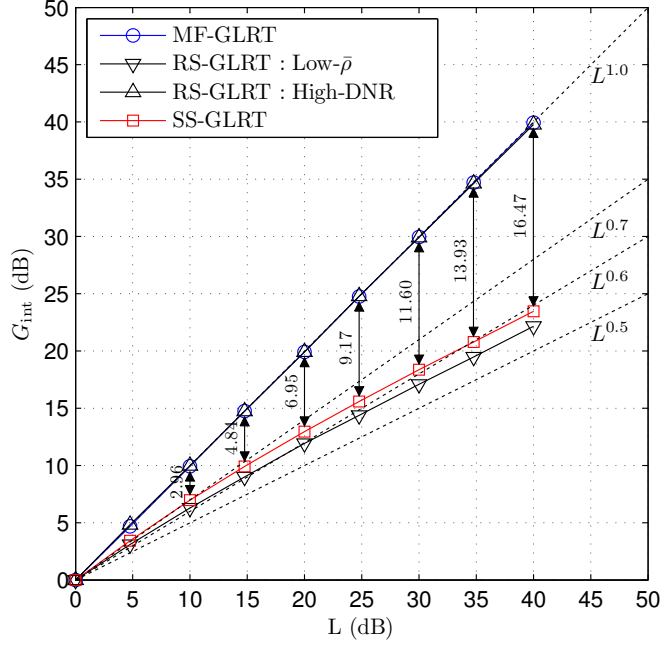


Figure 30. G_{int} as a Function of L for a PMR Scenario with $N_t = 2$ and $N_r = 3$

4.5.2 Ambiguity Performance.

This section illustrates the ambiguity performance of the considered GLRTs by calculating their test statistics as a function of the hypothesized target position $\mathbf{p} = [p_x, p_y]$. The scenario consists of two stationary transmitters at $\mathbf{d}^1 = [0.5, 4]$ km and $\mathbf{d}^2 = [-0.5, -4]$ km, three stationary receivers at $\mathbf{r}^1 = [-4, 2]$ km, $\mathbf{r}^2 = [-4, 0.5]$ km and $\mathbf{r}^3 = [-4, -2.5]$ km, and one target at $\mathbf{t} = [4, 0]$ km. Stationary and moving target scenarios are considered. The transmitters have carrier frequencies of 8.0 and 8.1 GHz, respectively, and isotropic $P_{\text{erp}}^i = 50$ W. All receivers are 6-element uniform linear arrays facing the $+p_x$ direction with 1.875 cm element spacing and unity element patterns, i.e., $G_e^j(\cdot) = 1$. Complex baseband signals \mathbf{s}_n^{ij} are simulated according to Eq. (117) with $f_s = 500$ kHz, $T = 2$ ms, $\sigma_n^2 = 2.0019 \times 10^{-14}$ (-106.99 dBm), and $\mathbf{u}^i = \exp\{j\boldsymbol{\theta}^i\}$, where $\boldsymbol{\theta}^i \in \mathbb{R}^{L \times 1}$ is a random phase vector with i.i.d. elements uniformly distributed on $[0, 2\pi]$, and $L = f_s T = 1000$. The target has an

isotropic 10 dBsm RCS, i.e., $\alpha^{ij} = \sqrt{10}$ for all i and j . Note that the receivers are not phase-synchronized due to the random phase θ^j in the direct-path and target-path channel coefficients, γ_d^{ij} and γ_t^{ij} , according to Eqs. (27) and (38) in Secs. 2.2.1 and 2.2.2, respectively. Note that this scenario is the same as the scenario considered in Sec. 3.5.2, except that here the CPI duration T is 2 ms ($L = 1000$) rather than 10 ms ($L = 5000$).

Three SNR-DNR scenarios are considered, given by $(\text{SNR}_{\text{avg}}, \text{DNR}_{\text{avg}}) = (-5, -35)$ dB, $(-10, -10)$ dB, and $(-15, 15)$ dB. These SNR-DNR scenarios fall within the low- $\bar{\rho}$, transition, and high-DNR regions, respectively, and they are identified in Fig. 28 by star symbols. Note that each SNR_{avg} is between 8 to 10 dB above the SNR_{avg} that is required at that DNR_{avg} to achieve $P_d = 0.90$. High SNR_{avg} values are chosen so that the ambiguity response may be clearly seen above noise. In order to achieve each SNR-DNR scenario, it is necessary to scale the direct-path and target-path signals that result from simulation of the scenario described in the previous paragraph. In particular, simulation of this scenario according to the signal model of Sec. 4.1 results in $\text{SNR}_{\text{avg}} = -43.14$ dB and $\text{DNR}_{\text{avg}} = 36.60$ dB, where these averages are taken across all surveillance and reference channels, respectively. Therefore, to achieve $(\text{SNR}_{\text{avg}}, \text{DNR}_{\text{avg}}) = (-15, 15)$ dB, every target-path signal is scaled by +28.14 dB ($-43.14 + 28.14 = -15$ dB), and every direct-path signal is scaled by -21.60 dB ($36.60 - 21.60 = 15$ dB). The other two SNR-DNR scenarios are achieved similarly.

4.5.2.1 Low- $\bar{\rho}$ Region.

Let $(\text{SNR}_{\text{avg}}, \text{DNR}_{\text{avg}}) = (-5, -35)$ dB, which is within the low- $\bar{\rho}$ region. Consider, first, a stationary target scenario, i.e., $\dot{\mathbf{t}} = [\dot{t}_x, \dot{t}_y] = \mathbf{0}_2$. Fig. 31 depicts the RS-GLRT and SS-GLRT statistics, ξ_{rs} and ξ_{ss} , respectively, as a function of hypothesized position \mathbf{p} when the hypothesized velocity is matched to the true target velocity,

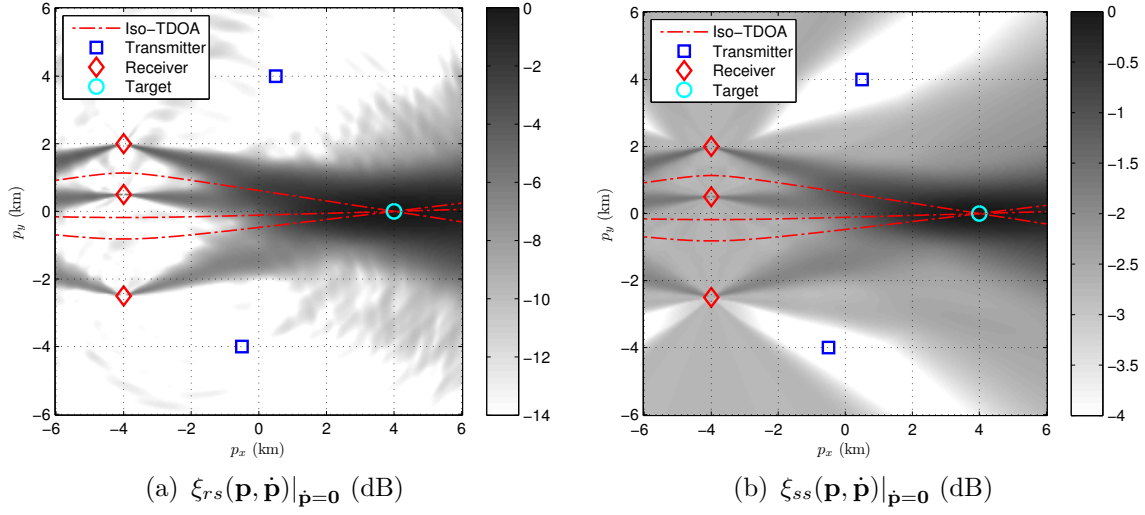


Figure 31. Low- $\bar{\rho}$ Ambiguity of the (a) RS-GLRT and (b) SS-GLRT for a Stationary Target

$\dot{\mathbf{p}} = \dot{\mathbf{t}} = \mathbf{0}_2$. As shown, both statistics exhibit a similar response. In particular, both test statistics peak at the true target position, and the effect of beamforming during surveillance channel formation is evident in the angular masking of their responses with respect to the receivers. In addition, the orientation of their main ambiguity responses in the target vicinity are aligned with the target iso-TDOA hyperbolas, which are depicted as red dashed-dotted lines. Each iso-TDOA contour represents the positions at which the TDOA of the hypothesized state equals the TDOA of the actual target state with respect to a given receiver-receiver pair, i.e., $\Delta \ell_p^{i,jk} = \Delta \ell_t^{i,jk}$ for the jk th receiver-receiver pair. This is illustrated in Fig. 32a, which depicts the TDOA $\Delta \tau_p^{i,jk} = \Delta \ell_p^{i,jk} / f_s$ as a function of \mathbf{p} for $i = 1$, $j = 2$, and $k = 3$. The target iso-TDOA contour $\Delta \tau_p^{1,23} = \Delta \tau_t^{1,23}$ is denoted by the red dash-dotted hyperbola.

Next, consider a moving target with velocity $\dot{\mathbf{t}} = [\dot{t}_x, \dot{t}_y] = [-375, 375]$ m/s. Fig. 33 depicts the RS-GLRT and SS-GLRT statistics, ξ_{rs} and ξ_{ss} , respectively, as a function of hypothesized position \mathbf{p} when the hypothesized velocity is matched to the true target velocity, $\dot{\mathbf{p}} = \dot{\mathbf{t}}$. As in the stationary target scenario, both statistics exhibit similar ambiguities. However, in contrast to the stationary target scenario,

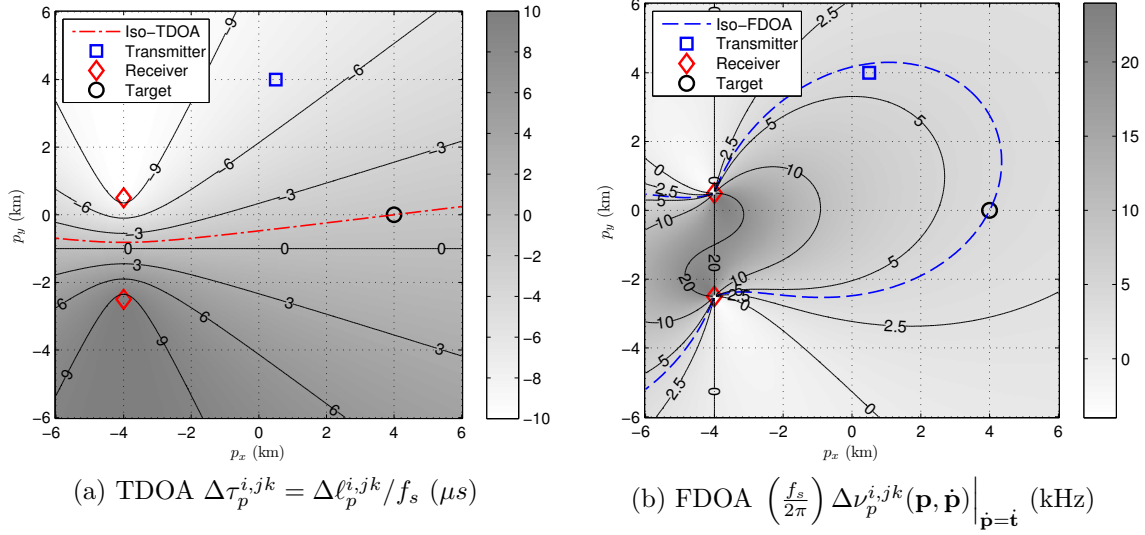


Figure 32. Example TDOA and FDOA Plots for $i = 1$, $j = 2$, and $k = 3$

the ambiguity peaks are sharpened around the true target location due to FDOA mismatch in addition to TDOA mismatch. This is seen by the manner in which the peak responses are aligned with the target iso-FDOA contours, which are depicted in Fig. 33 by blue dashed lines. Each iso-FDOA contour represents the positions at which the FDOA of the hypothesized state equals the FDOA of the actual target state with respect to a given receiver-receiver pair, i.e., $\Delta\nu_p^{i,jk} = \Delta\nu_t^{i,jk}$ for the jk th receiver-receiver pair. This is illustrated in Fig. 32b, which depicts the FDOA $\left(\frac{f_s}{2\pi}\right) \Delta\nu_p^{i,jk}$ in kHz as a function of \mathbf{p} for $i = 1$, $j = 2$, and $k = 3$, and assuming $\dot{\mathbf{p}} = \dot{\mathbf{t}}$. The target iso-FDOA contour $\Delta\nu_p^{1,23} = \Delta\nu_t^{1,23}$ is denoted in this figure by the blue dashed line.

The similarity of the RS-GLRT and SS-GRLT responses for both stationary and moving targets indicates that the ambiguity characteristics of the RS-GLRT are dominated by surveillance-surveillance processing in the low- $\bar{\rho}$ region. This is consistent with the detection sensitivity results in Sec. 4.5.1. It is interesting to note, however, that the RS-GLRT ambiguity response rolls-off more rapidly away from the peak response than the SS-GLRT. This is seen by noting that 14 dB and 4 dB of dynamic range are shown for ξ_{rs} and ξ_{ss} , respectively, in Figs. 31 and 33.

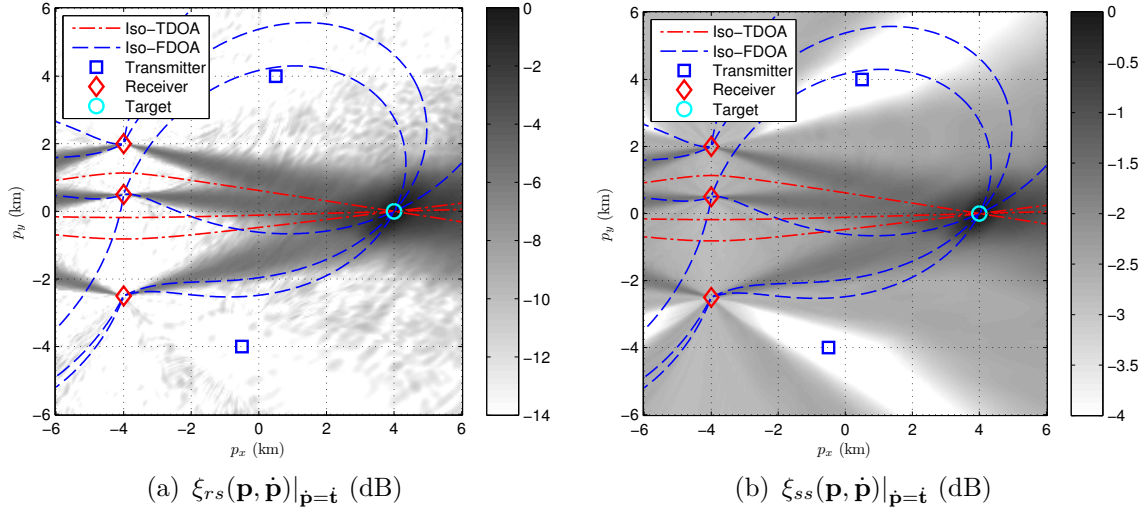


Figure 33. Low- $\bar{\rho}$ Ambiguity of the (a) RS-GLRT and (b) SS-GLRT for a Moving Target

4.5.2.2 High-DNR Region.

Next, let $(\text{SNR}_{\text{avg}}, \text{DNR}_{\text{avg}}) = (-15, 15)$ dB, which is within the high-DNR region as illustrated in Fig. 28. Consider, first, a stationary target scenario, i.e., $\dot{\mathbf{t}} = [\dot{t}_x, \dot{t}_y] = \mathbf{0}_2$. Fig. 34 depicts the ambiguity responses of the RS-GLRT and MF-GLRT statistics, ξ_{rs} and ξ_{mf} , respectively, as a function of hypothesized position \mathbf{p} when the hypothesized velocity is matched to the true target velocity, $\dot{\mathbf{p}} = \dot{\mathbf{t}} = \mathbf{0}_2$. As shown, the ambiguity responses of both statistics are nearly identical. In addition, the peak responses are aligned along the target iso-range ellipses, which are depicted as green dash-dotted lines. Each iso-range contour represents the positions at which the bistatic range of the hypothesized state equals the bistatic range of the actual target state with respect to a given transmitter-receiver pair, i.e., $\ell_p^{ij} = \ell_t^{ij}$ for the ij th transmitter-receiver pair. This is illustrated in Fig. 35a for one transmitter-receiver pair, which depicts the bistatic range $c\ell_p^{ij}/f_s$ in km as a function of \mathbf{p} for $i = 1$ and $j = 2$. The target iso-range contour $\ell_p^{12} = \ell_t^{12}$ is denoted in this figure by the green dash-dotted ellipse.

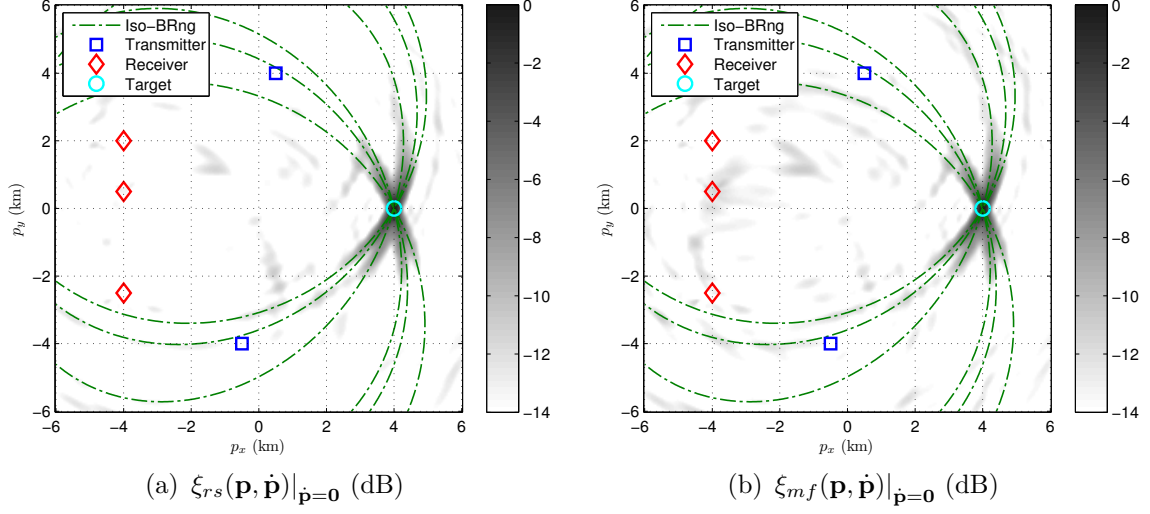


Figure 34. High-DNR Ambiguity of the (a) RS-GLRT and (b) MF-GLRT for a Stationary Target

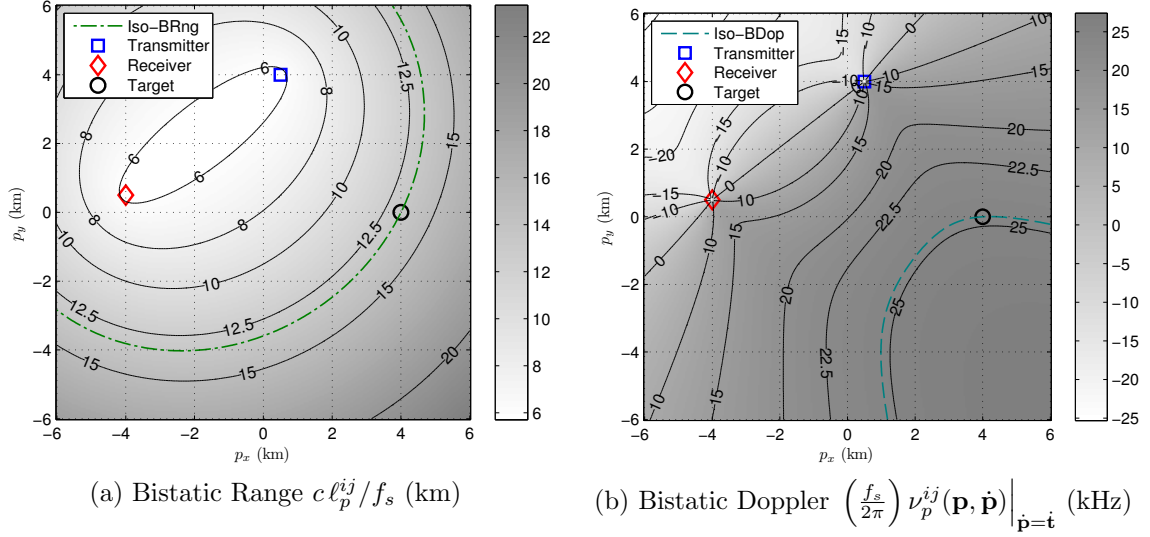


Figure 35. Bistatic Range and Bistatic Doppler for $i = 1$ and $j = 2$

Next, consider a moving target with velocity $\dot{\mathbf{t}} = [\dot{t}_x, \dot{t}_y] = [-375, 375]$ m/s. Fig. 36 depicts the RS-GLRT and MF-GLRT statistics, ξ_{rs} and ξ_{ss} , respectively, as a function of hypothesized position \mathbf{p} when the hypothesized velocity is matched to the true target velocity, $\dot{\mathbf{p}} = \dot{\mathbf{t}}$. Zoomed versions of both statistics in the immediate target vicinity are also depicted to give a close view of the peak ambiguity responses.

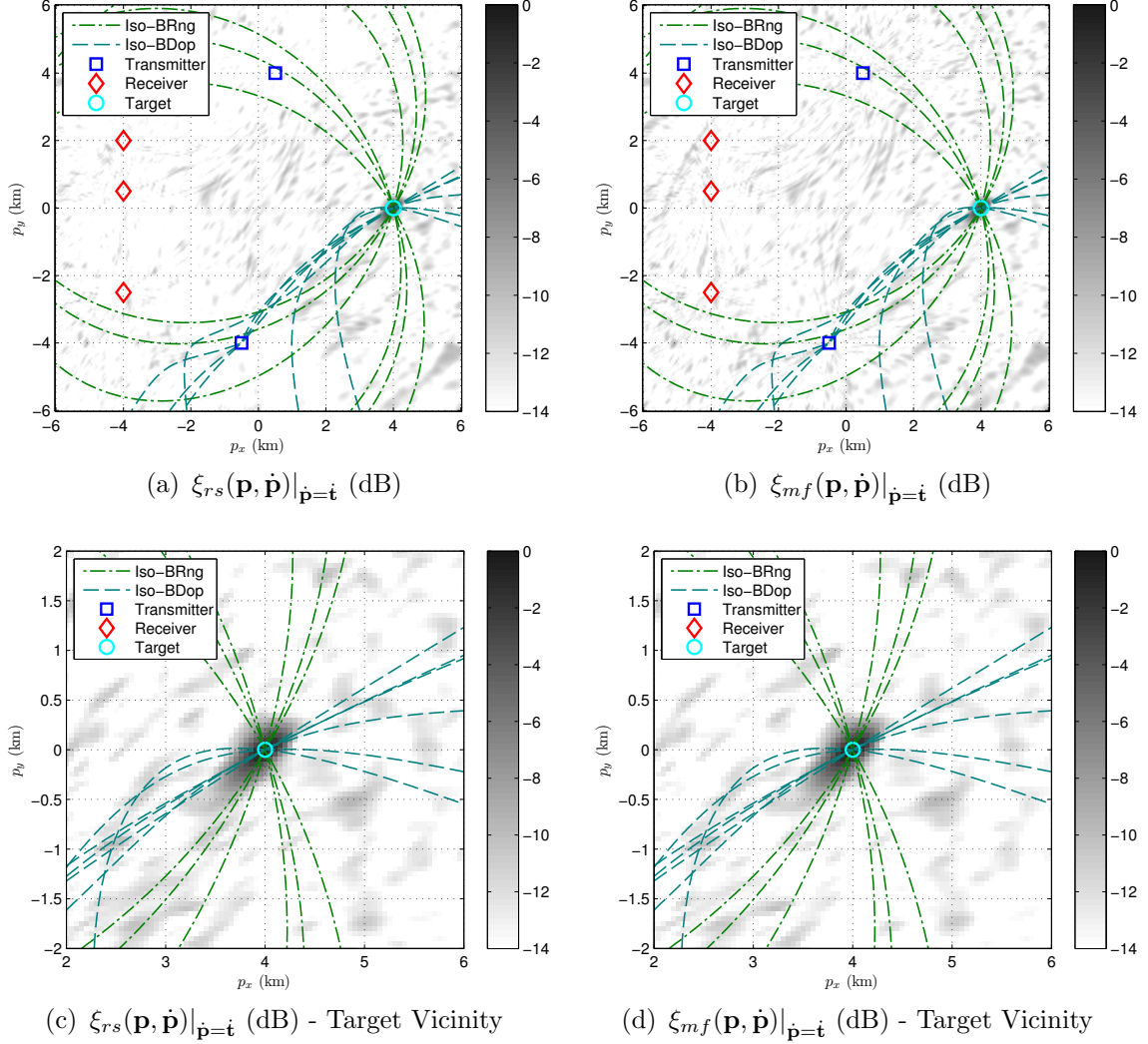


Figure 36. High-DNR Ambiguity of the (a,c) RS-GLRT and (b,d) MF-GLRT for a Moving Target

As in the stationary target scenario, both statistics exhibit nearly identical ambiguities. In addition, the peak responses are sharpened around the true target location in comparison to Fig. 34 due to the effect of bistatic Doppler mismatch in addition to bistatic range mismatch. This is seen by the manner in which the peak responses only exist in the immediate vicinity of both the target iso-range and iso-Doppler contours (the iso-Doppler contours are depicted by cyan dashed lines). Each iso-Doppler contour represents the positions at which the bistatic Doppler of the hypothesized

state equals the bistatic Doppler of the actual target state with respect to a given transmitter-receiver pair, i.e., $\nu_p^{ij} = \nu_t^{ij}$ for the ij th transmitter-receiver pair. This is illustrated in Fig. 35b, which depicts the bistatic Doppler $(\frac{f_s}{2\pi}) \nu_p^{ij}$ in kHz as a function of \mathbf{p} for $i = 1$ and $j = 2$, assuming $\dot{\mathbf{p}} = \dot{\mathbf{t}}$. The target iso-Doppler contour $\nu_p^{12} = \nu_t^{12}$ is denoted in this figure by the cyan dashed line.

The near equality of the RS-GLRT and MF-GLRT responses for both stationary and moving targets indicates that the ambiguity characteristics of the RS-GLRT are dominated by reference-surveillance processing in the high-DNR region. Again, this is consistent with the detection sensitivity results in Sec. 4.5.1, in which the sensitivity of the RS-GLRT approached that of the MF-GLRT in the high-DNR region.

4.5.2.3 Transition Region.

Finally, let $(\text{SNR}_{\text{avg}}, \text{DNR}_{\text{avg}}) = (-10, -10)$ dB, which is within the transition region as shown in Fig. 28. Fig. 37 depicts the ambiguity response of the RS-GLRT statistic, ξ_{rs} , for the stationary target scenario, in which $\dot{\mathbf{p}} = \dot{\mathbf{t}} = \mathbf{0}_2$. As shown, the ambiguity response exhibits significant sidelobes along both the iso-TDOA and the iso-bistatic range contours. Fig. 38 similarly depicts the RS-GLRT ambiguity response for the moving target scenario, in which $\dot{\mathbf{p}} = \dot{\mathbf{t}} = [-375, 375]$ m/s. In comparison to the stationary target scenario in Fig. 37, the moving target peak ambiguity response in Fig. 38 is additionally constrained to exist within the immediate vicinity of the iso-FDOA and iso-bistatic Doppler contours. Thus, the RS-GLRT ambiguity response in the transition region exhibits properties of the RS-GLRT ambiguity responses in both the low- $\bar{\rho}$ and high-DNR regions, in that it appears to be constrained in TDOA, FDOA, bistatic range, *and* bistatic Doppler⁴. This indicates that both surveillance-surveillance and reference-surveillance processing contribute significantly

⁴RS-GLRT ambiguity is also implicitly constrained in *angle* due to the beamforming operation during surveillance channel formation.

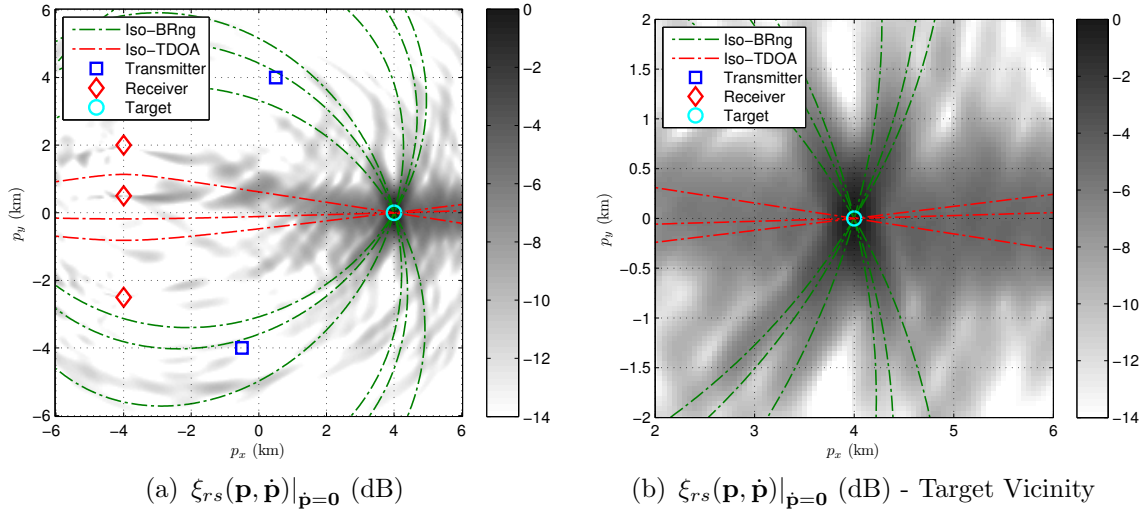


Figure 37. Transition Region Ambiguity of the RS-GLRT for a Stationary Target

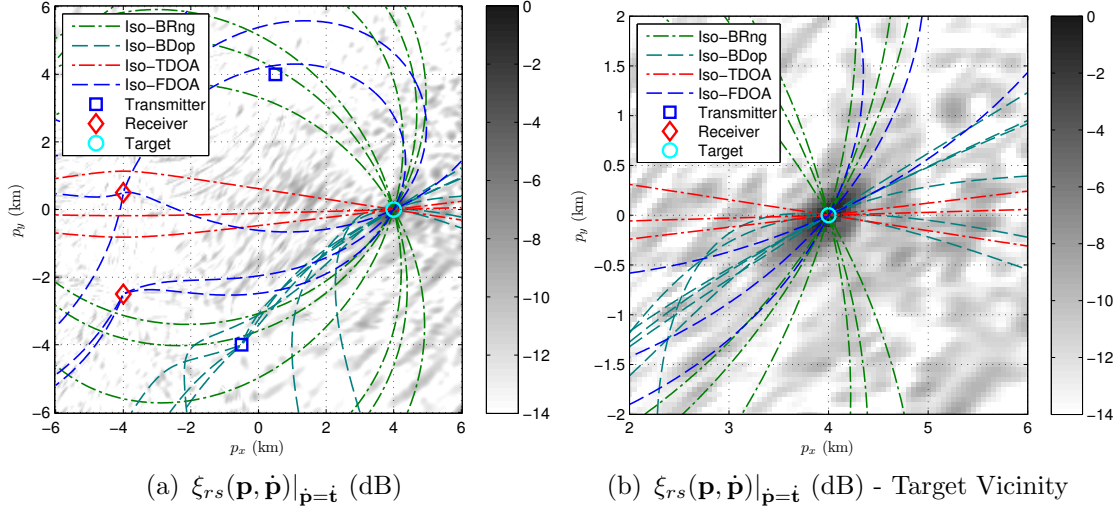


Figure 38. Transition Region Ambiguity of the RS-GLRT for a Moving Target

to the ambiguity properties of the RS-GLRT in the transition region. Again, this result is consistent with the detection sensitivity results in Sec. 4.5.1, where the transition region RS-GLRT sensitivity was shown to be intermediate to its sensitivity in the low- $\bar{\rho}$ and high-DNR regions.

4.6 Discussion

The results presented in Sec. 4.5 demonstrate that the RS-GLRT bridges the gap between the detection and ambiguity performance of the SS-GLRT and MF-GLRT detectors in a manner that depends on the quality of the direct-path reference signals. This result is expected from the analysis presented in Sec. 4.4, where it was shown that the RS-GLRT statistic encompasses the signal processing operations that are characteristic of both PSL and AMR, termed reference-surveillance and surveillance-surveillance processing, respectively. Both are discussed in turn.

First, reference-surveillance processing entails calculation of the pairwise reference-surveillance CAFs. This is the characteristic operation of matched filtering in AMR, and in the conventional approach to PMR detection using reference signals. Geometrically, each Tx-Rx pair constrains the target location in bistatic range and bistatic Doppler, as discussed in Sec. 4.4.2 and illustrated in Sec. 4.5.2. The detection results in Sec. 4.5.1 show that this type of processing is dominant for RS-GLRT detection when the DNR is positive, and that coherent integration gain is realized with increasing signal length in this region. Furthermore, RS-GLRT performance asymptotically approaches MF-GLRT performance with increasing DNR_{avg} . This is expected from the analysis in Sec. 4.3.2, where it was shown that ξ_{rs} approximates ξ_{mf} within a scalar constant under the high-DNR and high- $\bar{\rho}$ conditions. This justifies the conventional approach to PMR detection, in which the direct-path signal in the reference channel is used as the reference in an approximate matched filtering operation, provided DNR_{avg} is positive.

Second, surveillance-surveillance processing entails calculation of the pairwise surveillance-surveillance CAFs. This is the characteristic operation of PSL and PMR without a reference signal. Geometrically, each Rx-Rx pair constrains the target location in TDOA and FDOA, as discussed in Sec. 4.4.1 and illustrated in Sec. 4.5.2.

The detection results in Sec. 4.5.1 show that this type of processing is dominant for RS-GLRT detection when SNR_{avg} exceeds DNR_{avg} by approximately 5 dB, i.e., when $\bar{\rho} \leq 5$ dB. In this region, the RS-GLRT realizes a non-coherent integration gain with increasing signal length, similar to the SS-GLRT. Note that low- $\bar{\rho}$ scenarios are expected to be rare in practice, as both theoretical analysis and experimental results indicate $\bar{\rho}$ is often exceedingly (and problematically) large [27, 33].

It is interesting to note that the asymptotic detection performance of the RS-GLRT in the low- $\bar{\rho}$ region is slightly inferior to that of the SS-GLRT. This might be explained by the fact that the RS-GLRT is adversely affected at low DNR by extremely noisy reference signals that are completely ignored by the SS-GLRT. Incorporating these additional reference signals degrades the implicit estimation of the unknown signals that is performed in calculation of the RS-GLRT statistic. It also necessitates the implicit estimation of the unknown reference channel coefficients, which are additional nuisance parameters that do appear in the SS-GLRT formulation. Therefore, this result suggests that there are cases in which it is better to ignore additional information that pertains to *nuisance* parameters within the problem formulation. This is consistent with a result presented by Ramirez *et al.* in [70], where it was shown that ignoring *a priori* knowledge about the covariance structure of random observations in a particular detection problem is optimal under low-SNR conditions. In their application, incorporating this *a priori* knowledge via the derivation of a GLRT actually degrades performance because estimation of the resulting nuisance parameters cannot be performed accurately under low-SNR conditions.

These results clarify the fundamental role of direct-path signals in PMR detection. On one hand, these signals might not be expected to aid detection performance because they do not differ between the hypotheses in the detection problem of Eqs. (124)-(125). On the other hand, they provide valuable information about

the unknown transmitted signals, which are considered nuisance parameters in our formulation. In other words, they shed light on what the target return should look like by providing (potentially) high-quality estimates of the unknown transmitted signals to the PMR system. Fig. 29 demonstrates that the benefit provided by the direct-path signals in PMR detection depends on the length of the received signals. This benefit may be measured in terms of a direct-path gain, G_{dp} , defined as the difference between the MF-GLRT and SS-GLRT integration gain (G_{int}) curves in Fig. 30. The SS-GLRT is chosen rather than the RS-GLRT because the SS-GLRT represents the best possible PMR detection performance that can be achieved when direct-path signals are ignored completely. As shown in Fig. 30, G_{dp} ranges from 0 dB for $L = 1$ to 16.47 dB for $L = 10000$. Thus, direct-path signals may significantly improve detection performance, particularly for long signal lengths.

4.7 Conclusion

This chapter has presented a GLRT for centralized passive MIMO radar detection. The performance of this detector has been compared to similar GLRTs for centralized detection in active MIMO radar and passive source localization sensor networks. It has been shown that the detection and ambiguity performance of the passive MIMO radar GLRT varies between that of GLRTs for active MIMO radar and passive source localization in a manner that depends on the average direct-path SNR, which is a measure of the degree of knowledge about the (*a priori* unknown) transmitted signals. With high direct-path SNR, passive MIMO radar detection approaches that of active MIMO radar. With low direct-path SNR, passive MIMO radar detection is similar to that of passive source localization. In this way, passive MIMO radar generalizes both active MIMO radar and passive source localization, unifying them within a common theoretical framework. Such a framework is discussed further in Chapter V.

V. Unified Detection Framework

This chapter introduces a unified theoretical framework for detection in active and passive distributed RF sensor networks. This framework, summarized in Fig. 39, encompasses active and passive sensing networks including AMR, PMR, and PSL. The main features of this framework have already been introduced through the derivation, interpretation, and numerical analysis of the SS-GLRT and RS-GLRT detectors in Chapters III and IV, respectively. Drawing from these results, this chapter shows that PMR is the key to linking AMR and PSL sensor networks, which have traditionally been regarded as distinct. Thus, this framework provides fundamental insight into the natures of active and passive distributed RF sensing. Sec. 5.1 introduces the unified framework by showing how AMR, PMR, and PSL are related by simple transformations of their respective signal environments. Based on these relationships, signal models are defined for AMR, PMR and PSL in Sec. 5.2. The detectors that result from these signal models are discussed in Sec. 5.3, as well as the underlying signal processing operations performed by each. Conclusions follow in Sec. 5.4.

5.1 Transformations

The signal environments for AMR, PMR, and PSL are closely related. This is shown in Fig. 40, which depicts the signal environments for AMR, PMR, PMR without direct-path references, and PSL sensor networks, as well as the transformations that relate them. These transformations are discussed in turn. First, as discussed in Chapter I, AMR and PMR are distinguished from each other depending on whether the transmitters are cooperative (AMR) or non-cooperative (PMR). This is equivalent to whether the transmit signals are *a priori* known (AMR) or *a priori* unknown (PMR). Although AMR may have co-located transmitters and receivers, while in

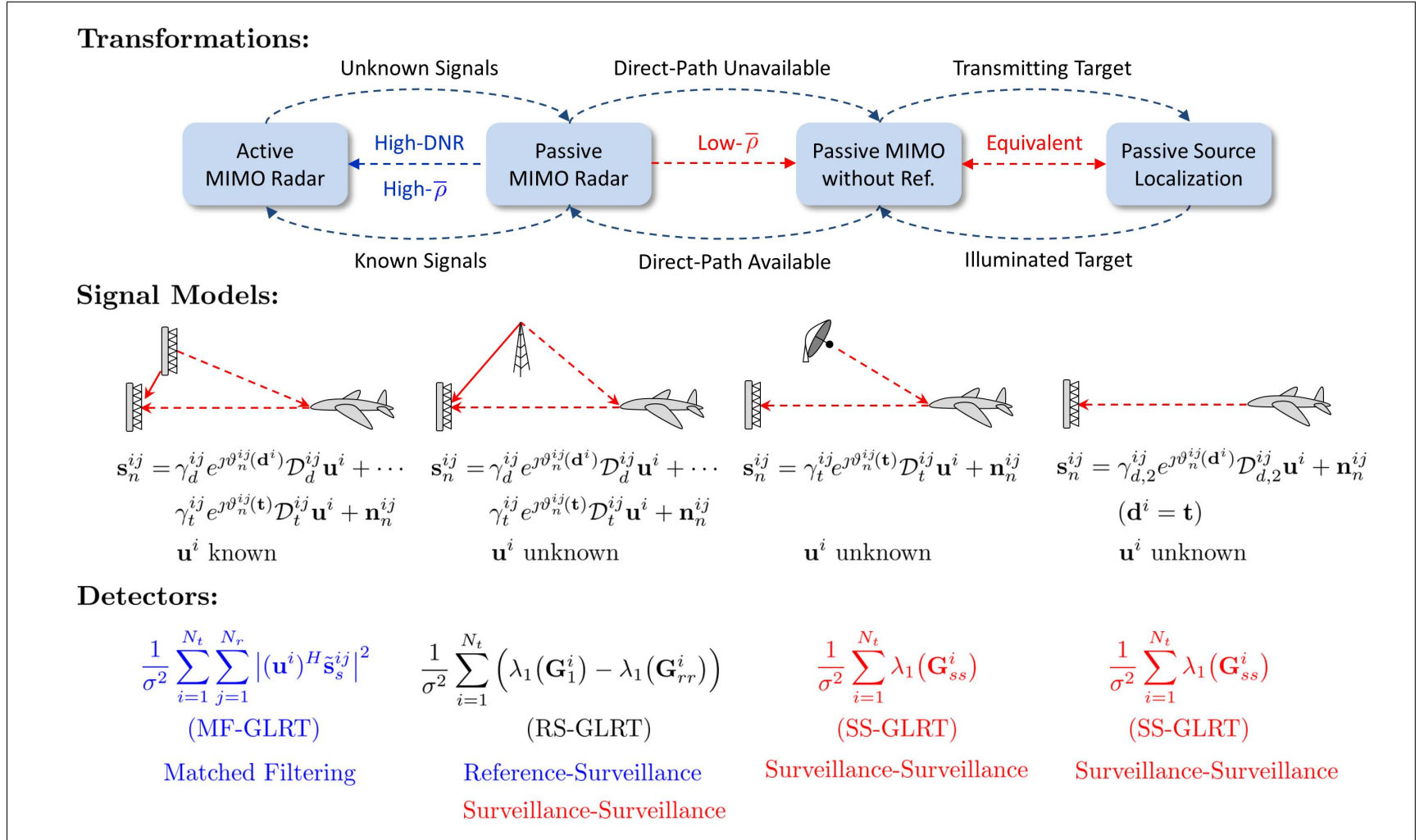


Figure 39. A Unified Theoretical Framework for Detection in Active and Passive Distributed RF Sensor Networks

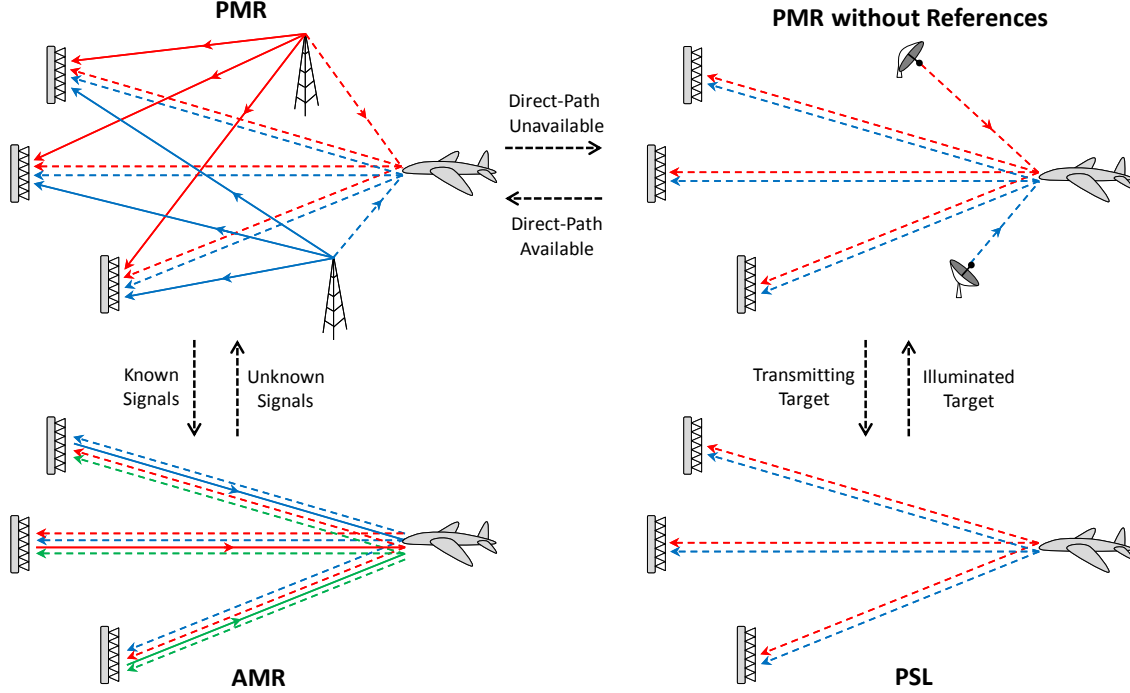


Figure 40. Transformations between AMR, PMR, and PSL Signal Environments

PMR the transmitters and receivers are necessarily separate, this distinction is insignificant from a detection processing perspective¹.

Although the transmit signals are *a priori* unknown in PMR, imperfect estimates of these transmit signals are provided to the PMR system by direct-path signals. The quality of these estimates is quantified by the average DNR; high-quality and low-quality estimates are provided by high-DNR and low-DNR direct-path signals, respectively. This defines a continuum quantified by the average DNR. At the high-DNR extreme the transmit signals become known perfectly; at the low-DNR extreme nothing is known about the transmit signals. This low-DNR extreme exists in PMR if direct-path signals are unavailable to the PMR receivers, which might occur if there is physical blockage of the line-of-sight paths between transmitters

¹Although this distinction will affect the implementation details of AMR detection processing, e.g., the delay-Doppler compensation, it does not fundamentally alter the *type* of processing (i.e., matched filtering) supported by the AMR signal environment.

and receivers, or if illuminators were to utilize highly directive transmission and/or null the receiver directions. The resulting sensor network is termed “PMR without direct-path references,” which is abbreviated “PMR without references” in Fig. 40 and throughout the rest of this chapter.

Finally, PMR without references and PSL are closely related because in both only target-path signals are received by the sensor network. They are distinguished according to whether the target-path signals are scattered (PMR without references) or emitted (PSL) by the target. Accordingly, these sensor networks are distinguished by the type of propagation channel experienced by the *a priori* unknown target-path signals. This distinction is insignificant from a detection perspective. Specifically, it is shown in Sec. 3.4 that PMR without references is mathematically equivalent to PSL when the effects of the first leg of the bistatic target-path channel are absorbed into the unknown transmitted signal.

5.2 Signal Models

In this section, signal models are given for AMR, PMR, and PSL. Due to the relationship between AMR, PMR, and PSL identified in Sec. 5.1, these signal models are derived directly from the PMR signal model presented in Chapter II.

5.2.1 Active MIMO Radar.

As discussed in Sec. 5.1, AMR is distinguished from PMR by the use of cooperative transmitters that transmit known signals. In addition, the transmitters within AMR are typically co-located with the receivers, although this is not necessarily true. Consequently, the signal model is identical to that of PMR except that the transmit signals $\{\mathbf{u}^i\}$ are assumed known, and the i th baseband signal at the n th element of

the j th AMR receiver array is given by Eq. (50) in Chapter II as

$$\mathbf{s}_n^{ij} = \gamma_d^{ij} e^{j\vartheta_n^{ij}(\mathbf{d}^i)} \mathcal{D}_d^{ij} \mathbf{u}^i + \gamma_t^{ij} e^{j\vartheta_n^{ij}(\mathbf{t})} \mathcal{D}_t^{ij} \mathbf{u}^i + \mathbf{n}_n^{ij} \quad (202)$$

where \mathbf{u}^i is the known transmit signal from the i th transmitter, $\mathcal{D}_d^{ij} = \mathcal{D}_{L^i}(\ell_d^{ij}, \nu_d^{ij})$ and $\mathcal{D}_t^{ij} = \mathcal{D}_{L^i}(\ell_t^{ij}, \nu_t^{ij})$ for brevity, and all the remaining variables are defined as in (50). Note that (202) is a CW formulation for AMR, whereas AMR is often studied in the context of pulsed operation. However, (202) also applies to pulsed operation if \mathbf{u}^i is interpreted as a pulse train that represents an entire CPI. Note also that the direct-path signal is often excluded in AMR signal model formulations because it is implicitly assumed that the receivers are blanked while any pulsed direct-path signal is incident.

5.2.2 Passive MIMO Radar.

The PMR signal model is derived in detail in Chapter II, where the i th baseband signal at the n th element of the j th PMR receiver array is given by Eq. (50) as

$$\mathbf{s}_n^{ij} = \gamma_d^{ij} e^{j\vartheta_n^{ij}(\mathbf{d}^i)} \mathcal{D}_d^{ij} \mathbf{u}^i + \gamma_t^{ij} e^{j\vartheta_n^{ij}(\mathbf{t})} \mathcal{D}_t^{ij} \mathbf{u}^i + \mathbf{n}_n^{ij} \quad (203)$$

where \mathbf{u}^i is the unknown transmit signal from the i th transmitter, $\mathcal{D}_d^{ij} = \mathcal{D}_{L^i}(\ell_d^{ij}, \nu_d^{ij})$ and $\mathcal{D}_t^{ij} = \mathcal{D}_{L^i}(\ell_t^{ij}, \nu_t^{ij})$ for brevity, and all the remaining variables are defined as in (50). The signal model for PMR without references is similarly given by

$$\mathbf{s}_n^{ij} = \gamma_t^{ij} e^{j\vartheta_n^{ij}(\mathbf{t})} \mathcal{D}_t^{ij} \mathbf{u}^i + \mathbf{n}_n^{ij} \quad (204)$$

which is equivalent to (203) except the direct-path signal is absent.

5.2.3 Passive Source Localization.

As discussed in Sec. 5.1, PMR without references and PSL are distinguished by whether the target-path signals are scattered (PMR without references) or emitted (PSL) by the target. This distinction may be defined mathematically by dividing the bistatic target-path channel coefficient γ_t^{ij} and delay-Doppler operator \mathcal{D}_t^{ij} into components that represent each leg of the bistatic propagation channel, i.e., $\gamma_t^{ij} = \gamma_{t,2}^{ij} \gamma_{t,1}^{ij}$ and $\mathcal{D}_t^{ij} = \mathcal{D}_{t,2}^{ij} \mathcal{D}_{t,1}^{ij}$, as discussed in Secs. 3.1 and 3.4 of Chapter III. Then, the i th baseband signal at the n th element of the j th PSL receiver array is given by

$$\mathbf{s}_n^{ij} = \gamma_{t,2}^{ij} e^{j\vartheta_n^{ij}(\mathbf{t})} \mathcal{D}_{t,2}^{ij} \mathbf{u}^i + \mathbf{n}_n^{ij} \quad (205)$$

where \mathbf{u}^i is the i th unknown signal emitted by the target, and $\gamma_{t,2}^{ij}$ is the channel coefficient between the target and the j th receiver, defined by (53) in Sec. 3.1 as

$$\gamma_{t,2}^{ij} = e^{j(\theta^i - \omega_c^i R_2^j(\mathbf{t})/c)} \sqrt{\frac{P_{\text{erp}}^i(\mathbf{r}^j) \lambda^{i2} G_e^j(\mathbf{t})}{(4\pi R_2^j(\mathbf{t}))^2}} \quad (206)$$

where the terms in (206) are defined in Sec. 3.1. Note that in (53) there is an α^{ij} that represents the bistatic reflectivity with respect to the ij th bistatic target-path channel. In (206), this term has been replaced by $\sqrt{P_{\text{erp}}^i(\mathbf{r}^j)}$, the effective radiated power in the direction of the j th receiver, to reflect the difference between PSL and PMR without references.

5.3 Detectors

When the centralized target detection problem is formulated for AMR, PMR, PMR without references, and PSL sensor networks using the signal models presented in Sec. 5.2, the resulting detectors exhibit similarities that reflect the similarities in

their respective signal models. These detectors, depicted in Fig. 39, are the MF-GLRT, RS-GLRT, and SS-GLRT detectors presented in Chapters III and IV. These are defined and discussed in the following sections.

5.3.1 Matched Filter GLRT.

First, the matched filter GLRT (MF-GLRT) is the GLRT for centralized detection in AMR sensor networks that results from the AMR signal model in (202). This GLRT is given by Eq. (150) in Sec. 4.2.3 as

$$\xi_{mf} = \frac{1}{\sigma^2} \sum_{i=1}^{N_t} \sum_{j=1}^{N_r} |(\mathbf{u}^i)^H \tilde{\mathbf{s}}_s^{ij}|^2 \underset{\mathcal{H}_0}{\overset{\mathcal{H}_1}{\geq}} \kappa_{mf} \quad (207)$$

where $\tilde{\mathbf{s}}_s^{ij} = (\mathcal{D}_t^{ij})^H \mathbf{s}_s^{ij}$ is the surveillance signal \mathbf{s}_s^{ij} after removal of the delay and Doppler that results from propagation along the ij th hypothesized target-path channel with respect to the cell under test. As shown in (207), the test statistic ξ_{mf} is formed by delay-Doppler compensating each surveillance signal, matched filtering, and then non-coherently integrating the matched filter outputs across all bistatic transmitter-receiver pairs. This signal processing structure is common in AMR detection [24, 43]. The test statistic ξ_{mf} follows the non-central and central chi-squared distributions under \mathcal{H}_1 and \mathcal{H}_0 , respectively (Sec. 4.3.1). The integration gain realized by the MF-GLRT grows coherently with increasing signal length, as expected for matched filtering (Sec. 4.5.1). In addition, the ambiguity properties of the MF-GLRT can be explained in terms of bistatic range, bistatic Doppler, and (for array receivers) AOA (Sec. 4.5.2). Note that matched filtering is only possible because the transmit signals $\{\mathbf{u}^i\}$ are known in the AMR detection problem formulation.

5.3.2 Surveillance-Surveillance GLRT.

Next, consider the surveillance-surveillance GLRT (SS-GLRT). As discussed in Sec. 3.2, this detector is the GLRT for centralized detection in PMR networks without direct-path references. Due to the mathematical equivalence between PMR networks without references and PSL networks, it is also the GLRT for centralized detection in PSL networks. The SS-GLRT is given by Eq. (79) in Sec. 3.2 as

$$\xi_{ss} = \frac{1}{\sigma^2} \sum_{i=1}^{N_t} \lambda_1(\mathbf{G}_{ss}^i) \underset{\mathcal{H}_0}{\overset{\mathcal{H}_1}{\gtrless}} \kappa_{ss} \quad (208)$$

where $\lambda_1(\cdot)$ denotes the largest eigenvalue of its matrix argument, and \mathbf{G}_{ss}^i is a Gram matrix with jk th element defined by

$$[\mathbf{G}_{ss}^i]_{jk} = (\tilde{\mathbf{s}}_s^{ij})^H \tilde{\mathbf{s}}_s^{ik} \quad (209)$$

It is shown in Sec. 4.4.1 that the entries of \mathbf{G}_{ss}^i may be found by sampling the CAFs between each pair of surveillance signals. This is referred to as *surveillance-surveillance processing*. The Gram matrix \mathbf{G}_{ss}^i is a complex Wishart matrix that is non-central under \mathcal{H}_1 and central under \mathcal{H}_0 , and the exact distribution of the test statistic ξ_{ss} is found in the recent random matrix theory literature (Sec. 3.3). In comparison to the MF-GLRT, the SS-GLRT achieves non-coherent rather than coherent integration gain with increasing signal length (Sec. 3.5.1.2 and 4.5.1). In addition, the ambiguity properties of the SS-GLRT can be explained in terms of TDOA, FDOA, and (for array receivers) AOA (Secs. 3.5.2 and 4.5.2). Finally, transmitters and receivers contribute asymmetrically to detection sensitivity in that adding an additional receiver increases detection sensitivity more than adding an additional transmitter (Sec. 3.5.1.1). This contrasts with the MF-GLRT, which benefits from transmitters and receivers equally.

5.3.3 Reference-Surveillance GLRT.

Finally, consider the RS-GLRT. As shown in Sec. 4.2.1, this detector is the GLRT for centralized detection in PMR networks with direct-path references. It is given by Eq. (148) in Sec. 4.2.1 as

$$\xi_{rs} = \frac{1}{\sigma^2} \sum_{i=1}^{N_t} \left(\lambda_1(\mathbf{G}_1^i) - \lambda_1(\mathbf{G}_{rr}^i) \right) \underset{\mathcal{H}_0}{\overset{\mathcal{H}_1}{\gtrless}} \kappa_{rs} \quad (210)$$

where \mathbf{G}_1^i is a Gram matrix with block structure

$$\mathbf{G}_1^i = \begin{bmatrix} \mathbf{G}_{ss}^i & \mathbf{G}_{sr}^i \\ \mathbf{G}_{rs}^i & \mathbf{G}_{rr}^i \end{bmatrix} \quad (211)$$

\mathbf{G}_{ss}^i is defined by (209), $\mathbf{G}_{rs}^i = (\mathbf{G}_{sr}^i)^H$, \mathbf{G}_{sr}^i and \mathbf{G}_{rr}^i are defined

$$[\mathbf{G}_{sr}^i]_{jk} = (\tilde{\mathbf{s}}_s^{ij})^H \tilde{\mathbf{s}}_r^{ik} \quad (212)$$

$$[\mathbf{G}_{rr}^i]_{jk} = (\tilde{\mathbf{s}}_r^{ij})^H \tilde{\mathbf{s}}_r^{ik} \quad (213)$$

and $\tilde{\mathbf{s}}_r^{ij} = (\mathcal{D}_d^{ij})^H \mathbf{s}_r^{ij}$ is the reference signal \mathbf{s}_r^{ij} after removal of the delay and Doppler shift due to direct-path propagation from the i th transmitter to the j th receiver. It is shown in Sec. 4.4.2 that the entries of \mathbf{G}_{sr}^i may be found by sampling CAFs between reference and surveillance signals. The calculation of such reference-surveillance CAFs, referred to as *reference-surveillance processing*, can be interpreted as matched filtering with a noisy reference. This operation is the basis for the conventional approach to PMR detection, described in Sec. 1.4.1.

The Gram matrix \mathbf{G}_1^i is a non-central complex Wishart matrix under both \mathcal{H}_1 and \mathcal{H}_0 , however the random variables $\lambda_1(\mathbf{G}_1^i)$ and $\lambda_1(\mathbf{G}_{rr}^i)$ in (210) are not independent due to the dependence of \mathbf{G}_1^i on \mathbf{G}_{rr}^i . This case does not appear to have been addressed

in the random matrix literature; consequently, the probability distribution of the statistic ξ_{rs} is not known. However, the distribution of ξ_{rs} can be approximated under certain conditions, described shortly.

The appearance of both \mathbf{G}_{ss}^i and \mathbf{G}_{sr}^i in (211) suggests that the RS-GLRT exploits both reference-surveillance and surveillance-surveillance processing. Comparison of the RS-GRLT, MF-GRLT, and SS-GLRT detectors in Sec. 4.5 shows that this is true. Specifically, RS-GLRT detection performance, in terms of both sensitivity and ambiguity, varies between that of the MF-GLRT and SS-GRLT as a function of the average target-path-to-noise ratio (SNR) and the average direct-path-to-noise ratio (DNR). It is shown in Sec. 4.5 that the performance of the RS-GLRT can be divided into three distinct SNR-DNR regions: a high-DNR region, in which reference-surveillance processing is dominant; a low- $\bar{\rho}$ region (where $\bar{\rho}$ denotes the average direct-path to target-path power ratio), in which surveillance-surveillance processing is dominant; and a transition region between the high-DNR and low- $\bar{\rho}$ regions where both types of processing are significant. These regions are now discussed in turn.

In the high-DNR region, reference-surveillance processing (i.e., noisy matched filtering) is dominant, and RS-GLRT performance approaches MF-GLRT performance. Consequently, the RS-GLRT realizes coherent integration gain with signal length (Sec. 4.5.1), and its ambiguity can be explained in terms of bistatic range, bistatic Doppler, and (for array receivers) AOA (Sec. 4.5.2). Furthermore, assuming high-DNR and high- $\bar{\rho}$, the RS-GLRT statistic, ξ_{rs} , is approximately equal to a scaled version of the MF-GLRT statistic, ξ_{mf} (Sec. 4.3.2). Therefore, ξ_{rs} approximately follows the non-central and central chi-squared distributions under \mathcal{H}_1 and \mathcal{H}_0 , respectively, under high-DNR and high- $\bar{\rho}$ conditions.

In the low- $\bar{\rho}$ region, surveillance-surveillance processing is dominant, and RS-GLRT performance approaches SS-GLRT performance. Thus, the RS-GLRT realizes

non-coherent integration gain with signal length (Sec. 4.5.1), and its ambiguity can be explained in terms of TDOA, FDOA, and (for array receivers) AOA (Sec. 4.5.2).

Finally, the RS-GLRT detector exhibits properties of both surveillance-surveillance and reference-surveillance processing in the transition region. In particular, its detection sensitivity is intermediate to that of the MF-GLRT and SS-GLRT (Sec. 4.5.1), and its ambiguity properties are influenced by bistatic range, bistatic Doppler, TDOA, FDOA, and (for array receivers) AOA (Sec. 4.5.2). Note that in the transition region the sensitivity and ambiguity performance of the RS-GLRT vary smoothly between the sensitivity and ambiguity of the SS-GLRT and MF-GLRT with increasing DNR.

5.4 Conclusion

This chapter demonstrates that PMR links PSL and AMR sensor networks within a common theoretical framework. This framework is summarized in Fig. 39. As discussed in Sec. 5.1, imperfect estimates of the unknown transmit signals are provided to the PMR system by direct-path signals. The quality of this estimate is quantified by the DNR; high-quality and low-quality estimates are provided by high-DNR and low-DNR direct-path signals. This defines a continuum that conceptually spans the gap between AMR and PSL sensor networks. At the high-DNR extreme, PMR approaches AMR in that the *a priori* unknown signals may be estimated accurately via reception of high-DNR direct-path signals. At the low-DNR extreme, PMR approaches PSL in that there is no auxiliary source of information about the *a priori* unknown transmit signals available to the PMR system apart from the target-path signal itself. In this way, PMR links PSL and AMR sensor networks, thereby unifying them within a common theoretical framework. This result provides insight into the fundamental natures of active and passive distributed RF sensing.

VI. Conclusion

This dissertation advances the theory of passive MIMO radar detection. The main contributions of this research are summarized in Sec. 6.1. Promising theoretical and experimental extensions to this research are discussed in Sec. 6.2.

6.1 Summary of Contributions

As stated in Sec. 1.6, the main contributions of this research are:

1. The derivation and statistical characterization of a novel detector for the centralized PMR detection *without* direct-path references problem (Chapter III)
2. The derivation and statistical characterization of a novel detector for the centralized PMR detection *with* direct-path references problem (Chapter IV)
3. The introduction of a unified framework for detection in active and passive distributed RF sensor networks that encompasses active MIMO radar, passive MIMO radar, and passive source localization sensor networks (Chapter V)

6.1.1 PMR Detection without References.

Chapter III introduced the SS-GLRT, a novel GLRT detector for centralized PMR detection without direct-path references. The formulation of this detector extends the formulations of previous PMR detectors to account for multiple non-cooperative transmitters, multichannel (array) receivers, non-isotropic target scattering, and non-coherent receivers. Previous PMR detector formulations have considered, at most, two out of four of these conditions. These extensions are significant because they enhance detection sensitivity and reduce detection ambiguity. The exact distributions of the SS-GLRT test statistic are identified under both hypotheses using recent

results from RMT, which represents the first appearance of these distributions in the context of radar detection. These distributions show that detection sensitivity is only a function of the number of received signal samples, the number of transmitters and receivers in the PMR network, and the average target-path SNR. Furthermore, numerical examples demonstrate important properties of the detector, namely, that (a) receivers and transmitters contribute asymmetrically to detection sensitivity (which is uncommon in radar detection), and (b) integration gain grows non-coherently with increasing signal length. The SS-GLRT has been submitted for publication in [38].

6.1.2 PMR Detection with References.

Chapter IV introduced the RS-GLRT, a novel GLRT detector for centralized PMR detection with direct-path references. This detector extends the formulation of the SS-GLRT to include direct-path signals with arbitrary DNRs. This extension is significant because it quantifies, for the first time, the dependence of PMR detection performance on the quality of the direct-path reference signals. Analysis of the RS-GLRT test statistic distributions shows that detection sensitivity depends only on the number of received signal samples, the number of transmitters and receivers in the PMR network, the average target-path input SNR, and the average input DNR. Numerical simulations reveal that PMR detection sensitivity and ambiguity may be divided into three SNR/DNR regimes: first, a high-DNR region, in which reference-surveillance processing is dominant; second, a low- $\bar{\rho}$ region, in which surveillance-surveillance processing is dominant; and third, a transition region between the high-DNR and low- $\bar{\rho}$ regions, in which both types of processing contribute significantly to sensitivity and ambiguity. These regimes characterize, for the first time, how PMR sensitivity and ambiguity depends on *both* SNR and DNR. The RS-GLRT has been submitted for publication in [37].

6.1.3 Unified Detection Framework.

Finally, a novel theoretical framework for detection in active and passive distributed RF sensor networks is proposed. This framework, summarized in Fig. 39 of Chapter V, encompasses AMR, PMR, and PSL sensor networks. It identifies how AMR, PMR, and PSL are related by simple transformations of their respective signal environments. These transformations reveal that PMR is the key to linking AMR and PSL, which have traditionally been regarded as distinct. These relationships also suggest that PMR detection might exhibit properties of detection in both AMR and PSL sensor networks under the appropriate DNR conditions. Analysis of the RS-GLRT and SS-GLRT detectors shows that this is true, i.e., PMR detection performance, in terms of both sensitivity and ambiguity, varies between that of AMR and PSL as a function of the average DNR. In high-DNR scenarios, RS-GLRT performance approaches AMR performance. In such scenarios, reference-surveillance processing (i.e., noisy matched filtering) is dominant. In low- $\bar{\rho}$ scenarios (where $\bar{\rho}$ is the average direct-path to target-path signal power ratio), RS-GLRT performance approaches SS-GLRT performance, which is the GLRT detector for *both* PMR without references and PSL sensor networks. In such scenarios, surveillance-surveillance processing is dominant. Finally, at intermediate DNRs, RS-GLRT performance exhibits properties of both AMR and PSL. These results are explained by interpreting PSL and AMR as two extremes in terms of knowledge about the transmit signals, i.e., the signals are entirely unknown in PSL and entirely known in AMR. These extremes are spanned by PMR, for which direct-path signals provide a varying degree of knowledge about the unknown transmit signals that is quantified by the DNR. In this way, PMR may be interpreted as generalizing PSL and AMR. This result provides fundamental insight into the natures of active and passive distributed RF sensing.

6.2 Future Research

This work may be extended in several ways. First, the RS-GLRT detector could be extended to explicitly account for clutter-path interference. In this work, the RS-GLRT formulation considers only receiver noise and direct-path signals. Direct-path interference is mitigated via deterministic nulling of the transmitter direction during surveillance channel formation. Consequently, the RS-GLRT results presented in Chapter IV represent noise-limited performance, which may be regarded as an upper bound on performance. In practice, clutter-path interference often limits performance by masking target returns [19]. This problem is exacerbated for CW signals in comparison to pulsed signals because a CW signal’s ambiguity function fills all of range-Doppler space. Consequently, the ambiguity function floor of strong near-range clutter returns may mask far-range targets [53, 51]. This limits the applicability of pulsed-radar clutter mitigation techniques such as bistatic space-time adaptive processing (STAP), which are formulated assuming only intra-range cell clutter. It is expected that explicitly incorporating clutter-path signals into the RS-GLRT detector formulation (as in, e.g., [19]) will result in a detector that implicitly mitigates clutter-path interference. This will extend the applicability of the RS-GLRT to scenarios with challenging interference environments.

Second, the unified framework presented in this work could be extended to include localization in addition to detection. Maximizing the RS-GLRT statistic over a hypothesized target position-velocity space, Ω_{surv} , gives the MLE of the unknown target state, i.e.,

$$(\hat{\mathbf{t}}, \hat{\mathbf{t}}) = \arg \max_{(\mathbf{p}, \dot{\mathbf{p}}) \in \Omega_{\text{surv}}} \xi_{rs}(\mathbf{p}, \dot{\mathbf{p}}). \quad (214)$$

The corresponding Cramer-Rao Lower Bound (CRLB) for localization in PMR sensor networks does not currently exist. Note that (214) represents a single-step approach

that *directly* estimates the MLE of the unknown target state. This is in contrast to traditional two-step localization approaches that *indirectly* estimate the target state by measuring and then fusing intermediate quantities such as TDOA, FDOA, and AOA. A number of recent papers have investigated direct single-step localization performance for PSL sensor networks, an approach termed *direct position determination* [87, 5, 12, 86, 82]. It is expected that the CRLB for PMR localization may be similarly derived. It is also expected from the ambiguity results in Sec. 4.5.2 that this CRLB would be a function of both SNR *and* DNR, and would implicitly exploit AOA, TDOA, FDOA, bistatic range, and bistatic Doppler information, thereby unifying localization in AMR and PSL sensor networks within a common framework.

Finally, this work requires experimental verification. Specifically, it would be interesting to verify the ambiguity characteristics of the RS-GLRT detector in the high-DNR, transition, and low- $\bar{\rho}$ regions. A minimal experimental setup consists of one isotropic target, one pulsed transmitter, and multiple geographically-distributed single-channel receivers in an anechoic RF environment. Achieving the SNR and DNR required for each region requires careful control of the transmitter power, target radar cross section, and scenario geometry. Use of pulsed rather than CW transmission is convenient because it potentially enables isolation of the direct-path and target-path signals via time gating, provided the pulse duration is sufficiently short relative to the scenario geometry. This enables the use of single-channel rather than multichannel receivers, because multiple channels would not be required to spatially isolate the direct-path and target-path signals. An anechoic RF environment is required to minimize clutter-path interference, which is not addressed in the RS-GLRT formulation. Verification of the ambiguity characteristics associated with each of the three performance regions would confirm the relationship between AMR, PMR, and PSL sensor networks within the unified framework of Chapter V.

Appendix A. Far-Field Differential Range Approximation

Let the n th element of an array antenna be at location $\mathbf{r}_n = \mathbf{r} + \boldsymbol{\delta}_n$, where \mathbf{r} is the location of the array reference element, and $\boldsymbol{\delta}_n$ represents the offset of the n th element with respect to the reference element. Let the location \mathbf{x} be in the far-field of the array, where the far-field is defined as $\Omega_{\text{ff}} = \{\mathbf{x} : \|\mathbf{x} - \mathbf{r}\| \gg 2 \|\boldsymbol{\delta}_n\|^2 / \lambda\}$. Then, for $\mathbf{x} \in \Omega_{\text{ff}}$, the range between \mathbf{x} and \mathbf{r}_n , $R_n = \|\mathbf{x} - \mathbf{r}_n\|$, can be approximated as the sum of the range to the array reference element, $R_0 = \|\mathbf{x} - \mathbf{r}\|$, and a differential term that accounts for the offset of the n th element with respect to the reference element. To show this, r_n can be expanded and simplified as follows,

$$R_n = \|\mathbf{x} - \mathbf{r}_n\| \quad (215)$$

$$= \sqrt{\|(\mathbf{x} - \mathbf{r}) - \boldsymbol{\delta}_n\|^2} \quad (216)$$

$$= \sqrt{\|\mathbf{x} - \mathbf{r}\|^2 - 2(\mathbf{x} - \mathbf{r})^T \boldsymbol{\delta}_n + \|\boldsymbol{\delta}_n\|^2} \quad (217)$$

$$= \|\mathbf{x} - \mathbf{r}\| \sqrt{1 - \frac{2(\mathbf{x} - \mathbf{r})^T \boldsymbol{\delta}_n + \|\boldsymbol{\delta}_n\|^2}{\|\mathbf{x} - \mathbf{r}\|^2}} \quad (218)$$

$$= \|\mathbf{x} - \mathbf{r}\| \left(1 - \frac{(\mathbf{x} - \mathbf{r})^T \boldsymbol{\delta}_n + \|\boldsymbol{\delta}_n\|^2 / 2}{\|\mathbf{x} - \mathbf{r}\|^2} + \text{H.O.T.} \right) \quad (219)$$

$$\approx \|\mathbf{x} - \mathbf{r}\| \left(1 - \frac{(\mathbf{x} - \mathbf{r})^T \boldsymbol{\delta}_n}{\|\mathbf{x} - \mathbf{r}\|^2} \right) \quad (220)$$

$$= R_0 - \hat{\mathbf{k}}(\mathbf{x}) \cdot \boldsymbol{\delta}_n \quad (221)$$

where $\hat{\mathbf{k}}(\mathbf{x})$ is the unit vector pointing from \mathbf{r} to \mathbf{x} . Equation (219) results from the following Taylor series expansion about $x = 0$, which converges for $|x| \leq 1$,

$$\sqrt{1+x} = \sum_{n=0}^{\infty} \frac{(-1)^n (2n)!}{(1-2n)(n!)^2 (4^n)} = 1 + \frac{x}{2} - \frac{x^2}{8} + \frac{x^3}{16} - \dots \quad (222)$$

Equation (220) then follows by ignoring the higher order terms due to the large magnitude of $\|\mathbf{x} - \mathbf{r}\|$, and observing that $\|\mathbf{x} - \mathbf{r}\| \gg \|\boldsymbol{\delta}_n\|^2$ due to the far-field condition.

Appendix B. Reference and Surveillance Channel Formation

Given an arbitrary unitary matrix $\mathbf{A}^{ij} \in \mathbb{C}^{N_e L \times N_e L}$, the scalar $\|\mathbf{s}^{ij} - \mathbf{M}_1^{ij} \mathbf{u}^i\|^2$ in (135) may be expressed as

$$\begin{aligned} & \|\mathbf{s}^{ij} - \mathbf{M}_1^{ij} \mathbf{u}^i\|^2 \\ &= \|\mathbf{A}^{ij}(\mathbf{s}^{ij} - \mathbf{M}_1^{ij} \mathbf{u}^i)\|^2 \end{aligned} \quad (223)$$

$$= \|\mathbf{A}^{ij} \mathbf{s}^{ij}\|^2 - 2\text{Re}\{\mathbf{s}^{ijH} \mathbf{M}_1^{ij} \mathbf{u}^i\} + \|\mathbf{A}^{ij} \mathbf{M}_1^{ij} \mathbf{u}^i\|^2 \quad (224)$$

We consider unitary matrices of the form $\mathbf{A}^{ij} = (\mathbf{B}^{ij} \otimes \mathbf{I}_L)^H$, where $\mathbf{B}^{ij} \in \mathbb{C}^{N_e \times N_e}$ is a unitary beamforming matrix that consists of N_e orthonormal column vectors,

$$\mathbf{B}^{ij} = [\mathbf{b}_s^{ij}, \mathbf{b}_r^{ij}, \mathbf{b}_3^{ij}, \dots, \mathbf{b}_{N_e}^{ij}] \quad (225)$$

and \mathbf{b}_s^{ij} and \mathbf{b}_r^{ij} denote surveillance and reference beamformers, respectively, defined according to the approach depicted in Fig. 25. Specifically, \mathbf{b}_r^{ij} steers in the i th transmitter direction,

$$\mathbf{b}_r^{ij} = \frac{\mathbf{a}_d^{ij}}{\|\mathbf{a}_d^{ij}\|} \quad (226)$$

and \mathbf{b}_s^{ij} steers in the direction of the position under test, \mathbf{p} , while placing a null in the transmitter direction,

$$\mathbf{b}_s^{ij} = \frac{\mathbf{P}_{r^\perp}^{ij} \mathbf{a}_p^{ij}}{\|\mathbf{P}_{r^\perp}^{ij} \mathbf{a}_p^{ij}\|} \quad (227)$$

where $\mathbf{P}_{r^\perp}^{ij} = \mathbf{I}_{N_e} - \mathbf{b}_r^{ij} \mathbf{b}_r^{ijH}$ is the projection matrix into the orthogonal complement of \mathbf{b}_r^{ij} . The remaining columns $\{\mathbf{b}_k^{ij} : k = 3 \dots N_e\}$ are defined so that $(\mathbf{B}^{ij})^H \mathbf{B}^{ij} = \mathbf{I}_{N_e}$.

A geometric interpretation of \mathbf{B}^{ij} is given in Fig. 41 [72]. For the ij th bistatic pair, the direct-path and hypothesized target-path steering vectors, \mathbf{a}_d^{ij} and \mathbf{a}_p^{ij} , are linearly independent but not necessarily orthogonal, and they span a rank-2 subspace of \mathbb{C}^{N_e} , denoted $\langle [\mathbf{a}_d^{ij} \ \mathbf{a}_p^{ij}] \rangle$. The reference and surveillance beamformers, \mathbf{b}_r^{ij} and \mathbf{b}_s^{ij} , are an

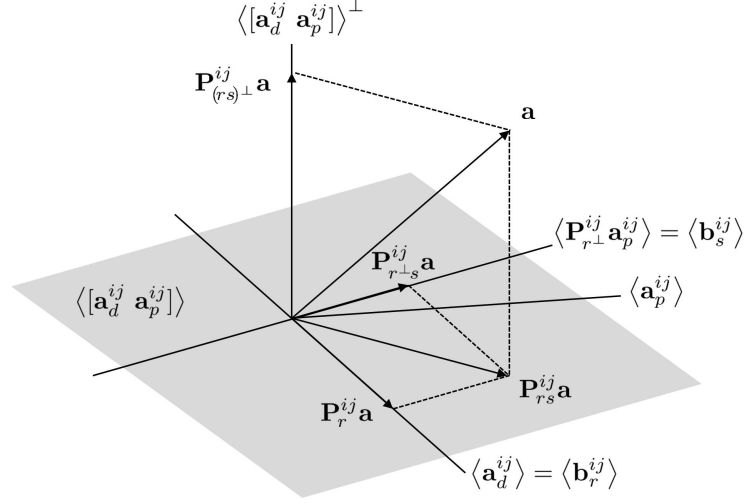


Figure 41. Decomposition of \mathbb{C}^{N_e} into Subspaces Spanned by the Columns of \mathbf{B}^{ij} ; the Rank-2 Subspace $\langle [\mathbf{a}_d^{ij} \ \mathbf{a}_p^{ij}] \rangle$ is Depicted by the Gray Plane

orthonormal basis for $\langle [\mathbf{a}_d^{ij} \ \mathbf{a}_p^{ij}] \rangle$. Similarly, $\{\mathbf{b}_k^{ij} : k = 3 \dots N_e\}$ is an orthonormal basis for the orthogonal complement of $\langle [\mathbf{a}_d^{ij} \ \mathbf{a}_p^{ij}] \rangle$, denoted $\langle [\mathbf{a}_d^{ij} \ \mathbf{a}_p^{ij}] \rangle^\perp$. Note that

$$\mathbf{B}^{ij} \mathbf{B}^{ijH} = \underbrace{\mathbf{b}_s^{ij} \mathbf{b}_s^{ijH}}_{=\mathbf{P}_{r^\perp s}^{ij}} + \underbrace{\mathbf{b}_r^{ij} \mathbf{b}_r^{ijH}}_{=\mathbf{P}_r^{ij}} + \underbrace{\sum_{k=3}^{N_e} \mathbf{b}_k^{ij} \mathbf{b}_k^{ijH}}_{=\mathbf{P}_{(rs)^\perp}^{ij}} = \mathbf{I}_{N_e} \quad (228)$$

where $\mathbf{P}_{r^\perp s}^{ij}$, \mathbf{P}_r^{ij} , and $\mathbf{P}_{(rs)^\perp}^{ij}$ are orthogonal projections into $\langle \mathbf{b}_s^{ij} \rangle$, $\langle \mathbf{b}_r^{ij} \rangle$, and $\langle [\mathbf{a}_d^{ij} \ \mathbf{a}_p^{ij}] \rangle^\perp$, respectively.

The terms of (224) are considered in turn. First, $\|\mathbf{A}^{ij} \mathbf{s}^{ij}\|^2$ can be expanded

$$\|\mathbf{A}^{ij} \mathbf{s}^{ij}\|^2 = \|(\mathbf{B}^{ij} \otimes \mathbf{I}_L)^H \mathbf{s}^{ij}\|^2 \quad (229)$$

$$= \|\mathbf{s}_s^{ij}\|^2 + \|\mathbf{s}_r^{ij}\|^2 + \underbrace{\sum_{k=3}^{N_e} \|\mathbf{w}_k^{ij}\|^2}_{=E_{(rs)^\perp}^{ij}} \quad (230)$$

where \mathbf{s}_s^{ij} and \mathbf{s}_r^{ij} denote surveillance and reference channel signals, respectively,

$$\mathbf{s}_{(s,r)}^{ij} = \sum_{n=1}^{N_e} [\mathbf{b}_{(s,r)}^{ij}]_n^* \mathbf{s}_n^{ij} \quad (231)$$

and \mathbf{w}_k^{ij} is given by

$$\mathbf{w}_k^{ij} = \sum_{n=1}^{N_e} [\mathbf{b}_k^{ij}]_n^* \mathbf{s}_n^{ij} \quad (232)$$

The notation $[\mathbf{x}]_n$ denotes the n th element of the vector \mathbf{x} . Note that $E_{(rs)^\perp}^{ij}$ represents the total energy within the projection of \mathbf{s}^{ij} into $\langle [\mathbf{a}_d^{ij} \ \mathbf{a}_p^{ij}] \rangle^\perp$.

Next, the value $\mathbf{s}^{ijH} \mathbf{M}_1^{ij} \mathbf{u}^i$ in the second term of (224) can be expressed using (228) as

$$\mathbf{s}^{ijH} \mathbf{M}_1^{ij} \mathbf{u}^i = \mathbf{s}^{ijH} ((\mathbf{P}_r^{ij} + \mathbf{P}_{r^\perp s}^{ij} + \mathbf{P}_{(rs)^\perp}^{ij}) \otimes \mathbf{I}_L) \mathbf{M}_1^{ij} \mathbf{u}^i \quad (233)$$

The term in (233) involving \mathbf{P}_r^{ij} can be expanded using (121), (226), (228), and the mixed-product property of the Kronecker product as

$$\mathbf{s}^{ijH} (\mathbf{P}_r^{ij} \otimes \mathbf{I}_L) \mathbf{M}_1^{ij} \mathbf{u}^i = \mathbf{s}^{ijH} (\mathbf{P}_r^{ij} \otimes \mathbf{I}_L) \left(\gamma_d^{ij} (\mathbf{a}_d^{ij} \otimes \mathcal{D}_d^{ij}) + \gamma_p^{ij} (\mathbf{a}_p^{ij} \otimes \mathcal{D}_p^{ij}) \right) \mathbf{u}^i \quad (234)$$

$$= \mathbf{s}^{ijH} \left(\gamma_d^{ij} (\mathbf{P}_r^{ij} \mathbf{a}_d^{ij}) \otimes \mathcal{D}_d^{ij} + \gamma_p^{ij} (\mathbf{P}_r^{ij} \mathbf{a}_p^{ij}) \otimes \mathcal{D}_p^{ij} \right) \mathbf{u}^i \quad (235)$$

$$= \mathbf{s}^{ijH} \left(\gamma_d^{ij} \mathbf{a}_d^{ij} \otimes \mathcal{D}_d^{ij} + \gamma_p^{ij} \beta_{dp}^{ij} \mathbf{a}_d^{ij} \otimes \mathcal{D}_p^{ij} \right) \mathbf{u}^i \quad (236)$$

where β_{dp}^{ij} quantifies the mismatch between \mathbf{a}_d^{ij} and \mathbf{a}_p^{ij} ,

$$\beta_{dp}^{ij} = \frac{(\mathbf{a}_d^{ij})^H \mathbf{a}_p^{ij}}{\|\mathbf{a}_d^{ij}\|^2} \quad (237)$$

The second term in (236), which represents leakage of the target-path signal into the reference channel, can be ignored due to the large power ratio between the direct-path and target-path signals typical in PMR, i.e., $|\gamma_d^{ij}|^2 \gg |\gamma_p^{ij}|^2$, and noting that $|\beta_{dp}^{ij}| < 1$

by the Cauchy-Schwarz inequality for $\mathbf{a}_d^{ij} \neq \mathbf{a}_p^{ij}$. Continuing with this approximation,

$$\mathbf{s}^{ijH}(\mathbf{P}_r^{ij} \otimes \mathbf{I}_L)\mathbf{M}_1^{ij}\mathbf{u}^i \approx \gamma_d^{ij} \mathbf{s}^{ijH}(\mathbf{a}_d^{ij} \otimes \mathcal{D}_d^{ij})\mathbf{u}^i \quad (238)$$

$$= \gamma_d^{ij} \left(\mathcal{D}_d^{ijH} \sum_{n=1}^{N_e} [\mathbf{a}_d^{ij}]_n^* \mathbf{s}_n^{ij} \right)^H \mathbf{u}^i \quad (239)$$

$$= \gamma_d^{ij} \sqrt{N_e} (\tilde{\mathbf{s}}_r^{ij})^H \mathbf{u}^i \quad (240)$$

where $\sqrt{N_e} = \|\mathbf{a}_d^{ij}\|$, and $\tilde{\mathbf{s}}_r^{ij}$ is the reference signal \mathbf{s}_r^{ij} in (231) after delay-Doppler compensation that removes the delay and Doppler of the direct-path channel,

$$\tilde{\mathbf{s}}_r^{ij} = \mathcal{D}_d^{ijH} \sum_{n=1}^{N_e} [\mathbf{a}_d^{ij}]_n^* \mathbf{s}_n^{ij} = \mathcal{D}_d^{ijH} \mathbf{s}_r^{ij} \quad (241)$$

Similarly, the term in (233) involving $\mathbf{P}_{r^\perp s}^{ij}$ can be expanded using (121) and (228), and simplified, giving

$$\mathbf{s}^{ijH}(\mathbf{P}_{r^\perp s}^{ij} \otimes \mathbf{I}_L)\mathbf{M}_1^{ij}\mathbf{u}^i = \gamma_p^{ij} \sqrt{N_e(1 - |\beta_{dp}^{ij}|^2)} (\tilde{\mathbf{s}}_s^{ij})^H \mathbf{u}^i \quad (242)$$

where $\sqrt{N_e(1 - |\beta_{dp}^{ij}|^2)} = \|\mathbf{P}_{r^\perp}^{ij} \mathbf{a}_p^{ij}\|$, and $\tilde{\mathbf{s}}_s^{ij}$ is the surveillance signal \mathbf{s}_s^{ij} in (231) after delay-Doppler compensation that removes the delay and Doppler of the target-path channel,

$$\tilde{\mathbf{s}}_s^{ij} = \mathcal{D}_p^{ijH} \sum_{n=1}^{N_e} [\mathbf{b}_s^{ij}]_n^* \mathbf{s}_n^{ij} = \mathcal{D}_p^{ijH} \mathbf{s}_s^{ij} \quad (243)$$

Unlike (240), (242) is exact rather than approximate.

Finally, the term in (233) involving $\mathbf{P}_{(rs)^\perp}^{ij}$ equals zero because \mathbf{a}_d^{ij} and \mathbf{a}_p^{ij} are in the null space of $\mathbf{P}_{(rs)^\perp}^{ij}$,

$$\mathbf{s}^{ijH}(\mathbf{P}_{(rs)^\perp}^{ij} \otimes \mathbf{I}_L)\mathbf{M}_1^{ij}\mathbf{u}^i = \mathbf{s}^{ijH} \left(\underbrace{\gamma_d^{ij} (\mathbf{P}_{(rs)^\perp}^{ij} \mathbf{a}_d^{ij})}_{=0} \otimes \mathcal{D}_d^{ij} + \gamma_p^{ij} \underbrace{(\mathbf{P}_{(rs)^\perp}^{ij} \mathbf{a}_p^{ij})}_{=0} \otimes \mathcal{D}_t^{ij} \right) \mathbf{u}^i \quad (244)$$

Substituting (240), (242), and (244) into (233) gives

$$\mathbf{s}^{ijH} \mathbf{M}_1^{ij} \mathbf{u}^i = (\mu_r^{ij} \tilde{\mathbf{s}}_r^{ijH} + \mu_s^{ij} \tilde{\mathbf{s}}_s^{ijH}) \mathbf{u}^i \quad (245)$$

where μ_r^{ij} and μ_s^{ij} are scale factors that account for the composite scaling of the reference and surveillance channels resulting from channel effects and beamforming, defined as

$$\mu_r^{ij} = \gamma_d^{ij} \sqrt{N_e} \quad (246)$$

$$\mu_s^{ij} = \gamma_p^{ij} \sqrt{N_e(1 - |\beta_{dp}^{ij}|^2)} \quad (247)$$

Finally, the term $\|\mathbf{A}^{ij} \mathbf{M}_1^{ij} \mathbf{u}^i\|^2$ in (224) can be expanded using (121) and (225), and simplified, to give

$$\|\mathbf{A}^{ij} \mathbf{M}_1^{ij} \mathbf{u}^i\|^2 \approx L(|\mu_r^{ij}|^2 + |\mu_s^{ij}|^2) \quad (248)$$

The approximation in (248) amounts to ignoring the target-path signal leakage in the reference channel, discussed earlier in relation to (236).

Substituting (230), (245), and (248) into (224), and noting that $\|\tilde{\mathbf{s}}_s^{ij}\|^2 = \|\mathbf{s}_s^{ij}\|^2$, $\|\tilde{\mathbf{s}}_r^{ij}\|^2 = \|\mathbf{s}_r^{ij}\|^2$, and $\|\mathbf{u}^i\|^2 = L$, the scalar $\|\mathbf{s}^{ij} - \mathbf{M}^{ij} \mathbf{u}^i\|^2$ can be expressed as

$$\|\mathbf{s}^{ij} - \mathbf{M}^{ij} \mathbf{u}^i\|^2 \approx \|\tilde{\mathbf{s}}_s^{ij} - \mu_s^{ij} \mathbf{u}^i\|^2 + \|\tilde{\mathbf{s}}_r^{ij} - \mu_r^{ij} \mathbf{u}^i\|^2 + E_{(rs)^\perp}^{ij} \quad (249)$$

Bibliography

- [1] “Airborne Passive Radars and their Applications APRA (SET-186)”. URL http://www.cso.nato.int/ACTIVITY_META.asp?ACT=SET-186. 22 April 2012.
- [2] “Official Site of the U.S. Air Force - Welcome”. URL <http://www.af.mil/main/welcome.asp>. 16 June 2013.
- [3] Abramowitz, E. and I. Stegun (editors). *Handbook of Mathematical Functions*. Dover Publications, Inc., 10 edition, Dec 1972.
- [4] Alcazar, V. “Crisis Management and the Anti-Access/Area-Denial Problem”. *Strategic Studies Quarterly*, 42–70, Winter 2012.
- [5] Amar, A. and A. J. Weiss. “Localization of Narrowband Radio Emitters Based on Doppler Frequency Shifts”. *IEEE Trans. Signal Process.*, 56(11):5500–5508, 2008.
- [6] Baczyk, Marcin Kamil and Mateusz Malanowski. “Decoding and reconstruction of reference DVB-T signal in passive radar systems”. *Proc. 11th Int. Radar Symp. (IRS)*, 1–4. 2010.
- [7] Baniak, J., G. Baker, A.M. Cunningham, and L. Martin. “Silent sentry passive surveillance”. *Aviation week and space technology*, 7:134–139, 1999.
- [8] Berizzi, F., M. Martorella, D. Petri, M. Conti, and A. Capria. “USRP technology for multiband passive radar”. *Proc. IEEE Radar Conf*, 225–229. 2010.
- [9] Bialkowski, K. S. and I. V. L. Clarkson. “Passive radar signal processing in single frequency networks”. *Signals, Systems and Computers (ASILOMAR), 2012 Conference Record of the Forty Sixth Asilomar Conference on*, 199–202. 2012. URL <http://ieeexplore.ieee.org/stamp/stamp.jsp?tp=&arnumber=6488989>.
- [10] Bialkowski, K. S., I. V. L. Clarkson, and S. D. Howard. “Generalized canonical correlation for passive multistatic radar detection”. *Proc. IEEE Statistical Signal Processing Workshop (SSP)*, 417–420. 2011.
- [11] Bongioanni, C., F. Colone, S. Bernardini, L. Lelli, A. Stavolo, and P. Lombardo. “Passive radar prototypes for multifrequency target detection”. *Proc. SPIE 6937*. 2007.
- [12] Bosse, J., A. Ferreol, and P. Larzabal. “Performance analysis of passive localization strategies: Direct one step approach versus 2 steps approach”. *Proc. IEEE Statistical Signal Processing Workshop (SSP)*, 701–704. 2011.

- [13] Brown, J., K. Woodbridge, A. Stove, and S. Watts. “Air target detection using airborne passive bistatic radar”. *Electronics Letters*, 46(20):1396–1397, 2010.
- [14] Bruyere, D. and N. Goodman. “Adaptive detection and diversity order in multistatic radar”. *IEEE Trans. Aerosp. Electron. Syst.*, 44(4):1615–1623, 2008.
- [15] Cardinali, R., F. Colone, C. Ferretti, and P. Lombardo. “Comparison of Clutter and Multipath Cancellation Techniques for Passive Radar”. *Proc. IEEE Radar Conf*, 469–474. 2007.
- [16] Chestnut, P. “Emitter Location Accuracy Using TDOA and Differential Doppler”. *IEEE Trans. Aerosp. Electron. Syst.*, 18:214–218, 1982.
- [17] Colone, F., R. Cardinali, P. Lombardo, O. Crognale, A. Cosmi, A. Lauri, and T. Bucciarelli. “Space-time constant modulus algorithm for multipath removal on the reference signal exploited by passive bistatic radar”. *IET Radar, Sonar & Navigation*, 3(3):253–264, 2009.
- [18] Colone, F., P. Falcone, C. Bongioanni, and P. Lombardo. “WiFi-Based Passive Bistatic Radar: Data Processing Schemes and Experimental Results”. *IEEE Trans. Aerosp. Electron. Syst.*, 48(2):1061–1079, 2012.
- [19] Colone, F., D. W. O’Hagan, P. Lombardo, and C. J. Baker. “A Multistage Processing Algorithm for Disturbance Removal and Target Detection in Passive Bistatic Radar”. *IEEE Trans. Aerosp. Electron. Syst.*, 45(2):698–722, 2009.
- [20] Daher, R. and R. Adve. “A Notion of Diversity Order in Distributed Radar Networks”. *IEEE Trans. Aerosp. Electron. Syst.*, 46(2):818–831, 2010.
- [21] Daun, M., U. Nickel, and W. Koch. “Tracking in multistatic passive radar systems using DAB/DVB-T illumination”. *Signal Processing*, 92:1365–1386, 2012.
- [22] Dawidowicz, B., K. S. Kulpa, M. Malanowski, J. Misiurewicz, P. Samczynski, and M. Smolarczyk. “DPCA Detection of Moving Targets in Airborne Passive Radar”. *IEEE Trans. Aerosp. Electron. Syst.*, 48(2):1347–1357, 2012.
- [23] Donley, M. B. and N. A. Schwartz. *Fiscal Year 2013 Air Force Posture Statement*. Technical report, United States Air Force, 2012.
- [24] Fishler, E., A. Haimovich, R. S. Blum, Jr. Cimini, L. J., D. Chizhik, and R. A. Valenzuela. “Spatial diversity in radars-models and detection performance”. *IEEE Trans. Signal Process.*, 54(3):823–838, 2006.
- [25] Gavish, M. and A. J. Weiss. “Performance analysis of bearing-only target location algorithms”. *IEEE Trans. Aerosp. Electron. Syst.*, 28(3):817–828, 1992.

- [26] Goodman, N. A. and D. Bruyere. “Optimum and decentralized detection for multistatic airborne radar”. *IEEE Trans. Aerosp. Electron. Syst.*, 43(2):806–813, 2007.
- [27] Gould, Dale, Robert Pollard, Carlos Sarno, and Paul Tittensor. “Developments to a multiband passive radar demonstrator system”. *Proc. IET Int Radar Systems Conf*, 1–5. 2007.
- [28] Gould, Dale, Robert Pollard, Carlos Sarno, and Paul Tittensor. “A Multiband Passive Radar Demonstrator”. *Bistatic-Multistatic Radar and Sonar Systems*, RTO-MP-SET-095. NATO, 2009. URL <http://www.rta.nato.int/Pubs/rdp.asp?RDP=RTO-EN-SET-133>.
- [29] Gradshteyn, I. and I. Ryzhik. *Table of Integrals, Series, and Products*. Academic Press, Inc., 4 edition, 1980.
- [30] Griffiths, H. and C. Baker. “The Signal and Interference Environment in Passive Bistatic Radar”. *Proc. Information, Decision and Control IDC '07*, 1–10. 2007.
- [31] Griffiths, H. and C. Baker. “Passive bistatic radar waveforms”. *Waveform Diversity & Design for Advanced Radar Systems*, chapter 5. Peter Peregrinus Ltd, (in preparation).
- [32] Griffiths, H. and N. Willis. “Klein Heidelberg – The First Modern Bistatic Radar System”. *IEEE Trans. Aerosp. Electron. Syst.*, 46(4):1571–1588, 2010.
- [33] Griffiths, H. D. and C. J. Baker. “Passive coherent location radar systems. Part 1: performance prediction”. *IEE Proceedings -Radar, Sonar and Navigation*, 152(3):153–159, 2005.
- [34] Griffiths, H. D. and N. R. W. Long. “Television-based bistatic radar”. *IEE Proceedings F Communications, Radar and Signal Processing*, 133(7):649–657, 1986.
- [35] Guner, A., M. A. Temple, and Jr. Claypoole, R. L. “Direct-path filtering of DAB waveform from PCL receiver target channel”. *Electronics Letters*, 39(1):118–119, 2003.
- [36] Guo, Jianxin, Lei Jiang, Jinliang Li, Qun Zhang, and Zhaozhao Gao. “A Robust Spatial DPI Suppression Algorithm for GSM-Based Passive Detection System”. *Proc. 7th Int Wireless Communications, Networking and Mobile Computing (WiCOM) Conf*, 1–4. 2011.
- [37] Hack, D., L. Patton, B. Himed, and M. Saville. “Centralized Passive MIMO Radar Detection”. *IEEE Trans. Signal Process.*, (submitted).

- [38] Hack, D., L. Patton, B. Himed, and M. Saville. “Centralized Passive MIMO Radar Detection without Direct-Path Reference Signals”. *IEEE Trans. Signal Process.*, (submitted).
- [39] Hack, D., L. Patton, A. Kerrick, and M. Saville. “Direct Cartesian Detection, Localization, and De-Ghosting for Passive Multistatic Radar”. *Proc. IEEE Sensor Array and Multichannel Signal Processing Workshop (SAM)*. 2012.
- [40] Hack, D., L. Patton, M. Saville, and B. Himed. “On the Applicability of Source Localization Techniques to Passive Multistatic Radar”. *Proc. 46th Asilomar Conf. Signals, Systems and Computers*. 2012.
- [41] Haimovich, A. M., R. S. Blum, and L. J. Cimini. “MIMO Radar with Widely Separated Antennas”. *IEEE Signal Process. Mag.*, 25(1):116–129, 2008.
- [42] Hanle, E. “Survey of bistatic and multistatic radar”. *IEE Proceedings F Communications, Radar and Signal Processing*, 133(7):587–595, 1986.
- [43] He, Qian, Nikolaus H. Lehmann, Rick S. Blum, and Alexander M. Haimovich. “MIMO Radar Moving Target Detection in Homogeneous Clutter”. *IEEE Trans. Aerosp. Electron. Syst.*, 46(3):1290–1301, 2010.
- [44] Horn, R. A. and C. R. Johnson. *Matrix Analysis*. Cambridge University Press, 1985.
- [45] Howland, P. E. “Passive Tracking Of Airborne Targets Using Only Doppler And DOA Information”. *Proc. IEE Colloquium Algorithms for Target Tracking*, 37–39. 1995.
- [46] Howland, P. E. “Target tracking using television-based bistatic radar”. *IEE Proceedings -Radar, Sonar and Navigation*, 146(3):166–174, 1999.
- [47] Jin, S., M. R. McKay, X. Gao, and I. B. Collings. “MIMO multichannel beam-forming: SER and outage using new eigenvalue distributions of complex noncentral Wishart matrices”. *IEEE Trans. Commun.*, 56(3):424–434, 2008.
- [48] Kang, Ming and M.-S. Alouini. “Largest eigenvalue of complex Wishart matrices and performance analysis of MIMO MRC systems”. *IEEE J. Sel. Areas Commun.*, 21(3):418–426, 2003.
- [49] Kay, Steven M. *Fundamentals of Statistical Signal Processing: Detection Theory*, volume 2. Prentice Hall PTR, 1998.
- [50] Klein, Mathieu and Nicolas Millet. “Multireceiver passive radar tracking”. *IEEE Aero El Sys Mag*, 27(10):26–36, 2012.
- [51] Kulpa, K. “The CLEAN type algorithms for radar signal processing”. *Proc. Microwaves, Radar and Remote Sensing Symp. MRRS 2008*, 152–157. 2008.

- [52] Kulpa, K., M. Malanowski, P. Samczynski, and B. Dawidowicz. “The concept of airborne passive radar”. *Proc. Microwaves, Radar and Remote Sensing Symp. (MRRS)*, 267–270. 2011.
- [53] Kulpa, K. S. and Z. Czekala. “Masking effect and its removal in PCL radar”. *IEE Proceedings -Radar, Sonar and Navigation*, 152(3):174–178, 2005.
- [54] Kuschel, H. “Software Defined Passive Radar”, 2009. (Presentation) European Microwave Week, Rome, 28th Sept. - 2cd Oct. 2009.
- [55] Kuschel, H., J. Heckenbach, S. Muller, and R. Appel. “On the potentials of passive, multistatic, low frequency radars to counter stealth and detect low flying targets”. *Proc. IEEE Radar Conf. RADAR '08*, 1–6. 2008.
- [56] Kuschel, H., J. Heckenbach, D. O’Hagan, and M. Ummenhofer. “A hybrid multi-frequency Passive Radar concept for medium range air surveillance”. *Proc. Microwaves, Radar and Remote Sensing Symp. (MRRS)*, 275–279. 2011.
- [57] Kuschel, H. and D. O’Hagan. “Passive radar from history to future”. *Proc. 11th Int. Radar Symp. (IRS)*, 1–4. 2010.
- [58] Levanon, N. “Interferometry against differential Doppler: performance comparison of two emitter location airborne systems”. *IEE Proceedings F Radar and Signal Processing*, 136(2):70–74, 1989.
- [59] Malanowski, M. and K. Kulpa. “Digital beamforming for Passive Coherent Location radar”. *Proc. IEEE Radar Conf. RADAR '08*, 1–6. 2008.
- [60] Malanowski, M., K. Kulpa, and J. Misiurewicz. “PaRaDe - PASSive RADar DEMonstrator family development at Warsaw University of Technology”. *Proc. Microwaves, Radar and Remote Sensing Symp. MRRS 2008*, 75–78. 2008.
- [61] Malanowski, M., K. Kulpa, and R. Suchozebrski. “Two-stage tracking algorithm for passive radar”. *Proc. 12th Int. Conf. Information Fusion FUSION '09*, 1800–1806. 2009.
- [62] Malanowski, Mateusz. “Comparison of Adaptive Methods for Clutter Removal in PCL Radar”. *Proc. Int. Radar Symp. IRS 2006*, 1–4. 2006.
- [63] Malanowski, Mateusz and Krzysztof Kulpa. “Two Methods for Target Localization in Multistatic Passive Radar”. *IEEE Trans. Aerosp. Electron. Syst.*, 48(1):572–580, 2012.
- [64] Mrstik, A.V. “Multistatic-Radar Binomial Detection”. *IEEE Trans. Aerosp. Electron. Syst.*, AES-14(1):103 –108, jan. 1978. ISSN 0018-9251.

- [65] Nickel, U. R. O. “System considerations for passive radar with GSM illuminators”. *Proc. IEEE Int Phased Array Systems and Technology (ARRAY) Symp*, 189–195. 2010.
- [66] Niu, Ruixin, R. S. Blum, P. K. Varshney, and A. L. Drozd. “Target Localization and Tracking in Noncoherent Multiple-Input Multiple-Output Radar Systems”. *IEEE Trans. Aerosp. Electron. Syst.*, 48(2):1466–1489, 2012.
- [67] O’Hagan, D. W., F. Colone, C. J. Baker, and H. D. Griffiths. “Passive Bistatic Radar (PBR) demonstrator”. *Proc. IET Int Radar Systems Conf*, 1–5. 2007.
- [68] Palmer, J., S. Palumbo, A. Summers, D. Merrett, S. Searle, and S. Howard. “An overview of an illuminator of opportunity passive radar research project and its signal processing research directions”. *Digital Signal Processing*, 21(5):593–599, 2011.
- [69] Palmer, J. and S. Searle. “Evaluation of Adaptive Filter Algorithms for Clutter Cancellation in Passive Bistatic Radar”. *Proc. IEEE Radar Conf. (RADAR)*. 2012.
- [70] Ramirez, D., J. Via, I. Santamaria, and L. Scharf. “Locally Most Powerful Invariant Tests for Correlation and Sphericity of Gaussian Vectors”. *IEEE Trans. Inf. Theory*, 59(4):2128–2141, 2013.
- [71] Richards, M. A., J. A. Scheer, and W. A. Holm. *Principles of Modern Radar*, volume 1. SciTech Publishing, Inc., 2010.
- [72] Scharf, L. L. and B. Friedlander. “Matched subspace detectors”. *IEEE Trans. Signal Process.*, 42(8):2146–2157, 1994.
- [73] Schroeder, A., M. Edrich, and V. Winkler. “Multi-Illuminator Passive Radar Performance Evaluation”. *Proc. Int. Radar Symp. (IRS)*. 2012.
- [74] Schroeder, Alexander and Michael Edrich. “CASSIDIAN multiband mobile passive radar system”. *Proc. Int. Radar Symp. (IRS)*, 286–291. 2011.
- [75] Searle, S., S. Howard, and J. Palmer. “Remodulation of DVB—T signals for use in Passive Bistatic Radar”. *Proc. Conf Signals, Systems and Computers (ASILOMAR) Record of the Forty Fourth Asilomar Conf*, 1112–1116. 2010.
- [76] Stansfield, R.G. “Statistical theory of d.f. fixing”. *Electrical Engineers - Part IIIA: Radiocommunication, Journal of the Institution of*, 94(15):762–770, march-april 1947.
- [77] Tan, D. K. P., H. Sun, Y. Lu, M. Lesturgie, and H. L. Chan. “Passive radar using Global System for Mobile communication signal: theory, implementation and measurements”. *IEE Proceedings -Radar, Sonar and Navigation*, 152(3):116–123, 2005.

- [78] Tao, R., H. Z. Wu, and T. Shan. “Direct-path suppression by spatial filtering in digital television terrestrial broadcasting-based passive radar”. *IET Radar, Sonar & Navigation*, 4(6):791–805, 2010.
- [79] Tharmarasa, R., N. Nandakumaran, M. McDonald, and T. Kirubarajan. “Resolving Transmitter-of-Opportunity Origin Uncertainty in Passive Coherent Location Systems”. *Proc. of SPIE*, volume 7445. 2009.
- [80] Torrieri, D. J. “Statistical Theory of Passive Location Systems”. *IEEE Trans. Aerosp. Electron. Syst.*, (2):183–198, 1984.
- [81] Van Trees, H. L. *Optimum Array Processing*. Detection, Estimation, and Modulation Theory, Part IV. Wiley-Interscience, 2002.
- [82] Vankayalapati, N. and S. Kay. “Asymptotically optimal detection/localization of LPI signals of emitters using distributed sensors”. *Proc. SPIE 7706*. 2010.
- [83] Vankayalapati, Naresh and Steven Kay. “Asymptotically Optimal Detection of Low Probability of Intercept Signals using Distributed Sensors”. *IEEE Trans. Aerosp. Electron. Syst.*, 48(1):737–748, 2012.
- [84] Wang, L. and B. Yazici. “Passive Imaging of Moving Targets Using Sparse Distributed Apertures”. *SIAM Journal of Imaging Sciences*, 5:769–808, 2012.
- [85] Wang, Pu, Hongbin Li, and B. Himed. “Moving Target Detection Using Distributed MIMO Radar in Clutter With Nonhomogeneous Power”. *IEEE Trans. Signal Process.*, 59(10):4809–4820, 2011.
- [86] Weiss, A. J. “Direct Geolocation of Wideband Emitters Based on Delay and Doppler”. *IEEE Trans. Signal Process.*, 59(6):2513–2521, 2011.
- [87] Weiss, A. J. and A. Amar. “Direct Position Determination of Multiple Radio Signals”. *EURASIP Journal on Applied Signal Processing*, 1:37–49, 2005.
- [88] Willis, N. J., H. D. Griffiths, and D. K. Barton. “Air Surveillance”. *Advances in Bistatic Radar*, chapter 6. SciTech Publishing, Inc., 2007.
- [89] Xue, Ming, Jian Li, and Petre Stoica. “MIMO Radar Waveform Design”. F. Gini, A. De Maio, and L. Patton (editors), *Waveform Diversity & Design for Advanced Radar Systems*. The Institution of Engineering and Technology, 2011.
- [90] Zanella, A., M. Chiani, and M. Win. “On the Marginal Distribution of the Eigenvalues of Wishart matrices”. *IEEE Trans. Commun.*, 57:1050–1060, 2009.
- [91] Zemmari, R., U. Nickel, and W.-D. Wirth. “GSM passive radar for medium range surveillance”. *Proc. European Radar Conf. EuRAD 2009*, 49–52. 2009.
- [92] Zemmari, Reda. “Reference signal extraction for GSM passive coherent location”. *Proc. 11th Int. Radar Symp. (IRS)*, 1–4. 2010.

REPORT DOCUMENTATION PAGE				Form Approved OMB No. 0704-0188	
<p>The public reporting burden for this collection of information is estimated to average 1 hour per response, including the time for reviewing instructions, searching existing data sources, gathering and maintaining the data needed, and completing and reviewing the collection of information. Send comments regarding this burden estimate or any other aspect of this collection of information, including suggestions for reducing this burden, to Department of Defense, Washington Headquarters Services, Directorate for Information Operations and Reports (0704-0188), 1215 Jefferson Davis Highway, Suite 1204, Arlington, VA 22202-4302. Respondents should be aware that notwithstanding any other provision of law, no person shall be subject to any penalty for failing to comply with a collection of information if it does not display a currently valid OMB control number. PLEASE DO NOT RETURN YOUR FORM TO THE ABOVE ADDRESS.</p>					
1. REPORT DATE (DD-MM-YY) 12-09-13		2. REPORT TYPE Dissertation		3. DATES COVERED (From - To) Sep 2008 – 12 Sep 2013	
4. TITLE AND SUBTITLE Passive MIMO Radar Detection				5a. CONTRACT NUMBER	
				5b. GRANT NUMBER	
				5c. PROGRAM ELEMENT NUMBER	
6. AUTHOR(S) Hack, Daniel E., Mr.				5d. PROJECT NUMBER	
				5e. TASK NUMBER	
				5f. WORK UNIT NUMBER	
7. PERFORMING ORGANIZATION NAME(S) AND ADDRESS(ES) Air Force Institute of Technology Graduate School of Engineering and Management (AFIT/EN) 2950 Hobson Way WPAFB OH 45433-7765				8. PERFORMING ORGANIZATION REPORT NUMBER AFIT-ENG-DS-13-S-07	
9. SPONSORING/MONITORING AGENCY NAME(S) AND ADDRESS(ES) <div style="display: flex; justify-content: space-between;"> <div> Dr. Braham Himed, AFRL/RYMD Air Force Research Laboratory 2241 Avionics Circle, Bldg 620 WPAFB, OH 45433-7320 </div> <div> Dr. Alan Kerrick, AFRL/RYMR Air Force Research Laboratory 2241 Avionics Circle, Bldg 620 WPAFB, OH 45433-7320 </div> </div>				10. SPONSORING/MONITORING AGENCY ACRONYM(S) AFRL/RYMD, AFRL/RYMR	
				11. SPONSORING/MONITORING AGENCY REPORT NUMBER(S)	
12. DISTRIBUTION/AVAILABILITY STATEMENT APPROVED FOR PUBLIC RELEASE; DISTRIBUTION UNLIMITED					
13. SUPPLEMENTARY NOTES					
14. ABSTRACT Passive multiple-input multiple-output (MIMO) radar is a sensor network comprised of multiple distributed receivers that detects and localizes targets using the emissions from multiple non-cooperative radio frequency transmitters. This dissertation advances the theory of centralized passive MIMO radar (PMR) detection by proposing two novel generalized likelihood ratio test (GLRT) detectors. The first addresses detection in PMR networks without direct-path signals. The second addresses detection in PMR networks with direct-path signals. The probability distributions of both test statistics are investigated using recent results from random matrix theory. Equivalence is established between PMR networks without direct-path signals and passive source localization (PSL) networks. Comparison of both detectors with a centralized GLRT for active MIMO radar (AMR) detection reveals that PMR may be interpreted as the link between AMR and PSL sensor networks. In particular, under high direct-path-to-noise ratio (DNR) conditions, PMR sensitivity and ambiguity approaches that of AMR. Under low-DNR conditions, PMR sensitivity and ambiguity approaches that of PSL. At intermediate DNRs, PMR sensitivity and ambiguity smoothly varies between that of AMR and PSL. In this way, PMR unifies PSL and AMR within a common theoretical framework. This result provides insight into the fundamental natures of active and passive distributed sensing.					
15. SUBJECT TERMS Passive Radar, Passive MIMO Radar, MIMO Radar, Passive Source Localization, Detection, Random Matrix Theory					
16. SECURITY CLASSIFICATION OF:			17. LIMITATION OF ABSTRACT: UU	18. NUMBER OF PAGES 150	19a. NAME OF RESPONSIBLE PERSON (Monitor) Dr. Michael A. Saville AFIT/ENG 19b. TELEPHONE NUMBER (Include Area Code) (937) 775-5169 michael.saville@wright.edu
a. REPORT U	b. ABSTRACT U	c. THIS PAGE U			